UNIVERSIDADE FEDERAL DO PARÁ
INSTITUTO DE CIÊNCIAS EXATAS E NATURAIS
PROGRAMA DE PÓS-GRADUAÇÃO EM FÍSICA

SCALAR FIELDS IN BLACK HOLE SPACETIMES AND ANALOGUES

Carolina Loureiro Benone
Advisor: Prof. Dr. Luís Carlos Bassalo Crispino

Belém-Pará
2017

UNIVERSIDADE FEDERAL DO PARÁ
INSTITUTO DE CIÊNCIAS EXATAS E NATURAIS
PROGRAMA DE PÓS-GRADUAÇÃO EM FÍSICA

Scalar fields in black hole spacetimes and analogues

Carolina Loureiro Benone
Advisor: Prof. Dr. Luís Carlos Bassalo Crispino

Belém-Pará
2017

Scalar fields in black hole spacetimes and analogues

Carolina Loureiro Benone

Doctoral thesis presented to the Programa de Pós-graduação em Física of the Universidade Federal do Pará (PPGF-UFPA) as part of the requirements needed for the degree of Doctor in Physics.
Advisor: Prof. Dr. Luís Carlos Bassalo Crispino

Examiners

Prof. Dr. Luís Carlos Bassalo Crispino (Advisor - UFPA)

Prof. Dr. André Carlos Lehum (Inside member - UFPA)

Prof. Dr. Manuel Eleutério Rodrigues (Inside member - UFPA)

Prof. Dr. Elcio Abdalla (Outside member - USP)

Prof. Dr. Carla Gobel Burlamaqui de Mello (Outside member - PUC/RJ)

Belém-Pará

2017

Abstract

Recently the hypothesis that scalar fields with small mass are good dark matter candidates has received some attention. Such scalar fields would interact with black holes, thus being interesting to study their absorption cross section and bound solutions in black hole scenarios. In this thesis we study scalar fields around black holes and analogue models, focusing on absorption cross sections and stationary solutions around black holes. Regarding the absorption, we consider a massive and charged scalar field impinging upon a charged black hole, as well as a massless scalar field impinging upon a charged and rotating black hole, finding the absorption cross section for both cases. We compute the high- and low-frequency limits of the absorption cross section, which we compare with the numerical results in order to validate them. For a frequency below the critical frequency, ω_c, the reflected part of the wave is enhanced, thus being greater than the incident wave. This phenomenum is known as superradiance and is associated to a negative absorption cross section. Regarding the stationary solutions, we consider modes of massive and charged scalar fields with $\omega = \omega_c$ around Kerr-Newman black holes. These modes form bound states around rotating black holes. These bound states – dubbed *scalar clouds* – are generically non-zero and finite on and outside the horizon, decay exponentially at spatial infinity, have a real frequency and are specified by a set of integer "quantum" numbers (n, ℓ, m). For a specific set of these numbers, the clouds are only possible along a 1-dimensional subset, called an *existence line*, of the 2-dimensional parameter space of Kerr black holes. We make a thorough investigation of the scalar clouds due to neutral (charged) scalar fields around Kerr(-Newman) black holes. We present the location of the existence lines for a variety of quantum numbers, their spatial representation and compare analytic approximation formulas available in the literature with our exact numerical results, exhibiting remarkable agreement for certain parameters ranges. Massless complex scalar fields can also form such bound states around black holes, provided that we put a mirror around the black hole to give the trapping condition. This may seem unphysical in the context of black holes, but if we consider a draining bathtub, the "mirror" can be simply the wall of the basin which contains the fluid. We show that sound waves, when enclosed in a cylindrical cavity, can form stationary waves around rotating acoustic holes. These acoustic perturbations display similar properties to the scalar clouds around Kerr and Kerr-Newman black holes; thus they are dubbed *acoustic clouds*. We make the comparison between scalar clouds around Kerr black holes and acoustic clouds around the draining bathtub explicit by studying also the properties of scalar clouds around Kerr black holes enclosed in a cavity. Acoustic clouds suggest the possibility of testing, experimentally, the existence and properties of black hole clouds, using analogue models. The last case we consider is the system formed by a static fluid placed between two concentric cylinders, where the inner cylinder rotates with constant angular momentum. For small enough time scales the fluid can be considered at rest, but, due to the rotation of the inner cylinder, we can still have superradiant instabilities, what enables the formation of clouds. We show that for $\omega = \omega_c$ we can have clouds for this case, analyzing the effect of the impedance of the inner cylinder on these clouds.

Keywords: Black holes, scalar fields, analogue models.

Knowledge areas: 1.05.01.03-7, 1.05.01.02-9.

Belém-Pará

2017

Resumo

Recentemente a hipótese de que campos escalares com massa pequena são bons candidatos à matéria escura tem recebido alguma atenção. Estes campos interagiriam com buracos negros, sendo, portanto, interessante estudar sua seção de choque de absorção e soluções ligadas neste contexto. Nesta tese nós estudamos campos escalares ao redor de buracos negros e modelos análogos, focando na seção de choque de absorção e soluções estacionárias ao redor de buracos negros. Em relação à absorção, nós consideramos um campo escalar massivo e carregado incidindo sobre um buraco negro carregado, assim como um campo escalar não massivo incidindo em um buraco negro carregado e com rotação, encontrando a seção de choque de absorção para ambos os casos. Nós calculamos os limites de alta e baixa frequência da seção de choque de absorção, que comparamos com nossos resultados numéricos com o intuito de validá-los. Para uma frequência abaixo da frequência crítica, ω_c, a parte refletida da onda é amplificada, sendo, portanto, maior que a onda incidente. Este fenômeno é chamado de superradiância e está associado a uma seção de choque de absorção negativa. Em relação às soluções estacionárias, nós consideramos modos de campos escalares massivos e carregados com $\omega = \omega_c$ ao redor de buracos negros de Kerr-Newman. Estes modos formam estados ligados ao redor de buracos negros girantes. Estes estados ligados – chamados de *nuvens escalares* – são genericamente não nulos e finitos no horizonte e fora dele, decaem exponencialmente no infinito espacial, possuem frequência real e são especificados por um conjunto de números "quânticos" inteiros (n, l, m). Para um subconjunto específico destes números, as nuvens são possíveis somente ao longo de um conjunto unidimensional, chamado de *linha de existência*, do conjunto bidimensional do espaço de parâmetros dos buracos negros de Kerr. Fazemos uma investigação completa das nuvens escalares devidas a campos escalares neutros (carregados) ao redor de buracos negros de Kerr(-Newman). Apresentamos a localização das linhas de existência para uma variedade de números quânticos, sua representação espacial e comparamos aproximações analíticas disponíveis na literatura com nossos resultados numéricos, exibindo concordância excelente para certos intervalos de parâmetros. Campos escalares complexos não massivos também podem formar estados ligados ao redor de buracos negros, desde que coloquemos um espelho ao redor do buraco negro para estabelecer a condição de confinamento. Isto pode parecer artificial no contexto de buracos negros, mas se considerarmos um buraco acústico girante, o "espelho" pode ser simplesmente a parede do recipiente que contém o fluido. Também mostramos que ondas sonoras, quando presas em uma cavidade cilíndrica, podem formar ondas estacionárias ao redor de buracos acústicos girantes. Estas perturbações acústicas apresentam propriedades semelhantes as das nuvens escalares ao redor de buracos negros de Kerr e Kerr-Newman; assim elas são chamadas de *nuvens acústicas*. Nós fazemos a comparação entre nuvens escalares ao redor de buracos negros de Kerr e nuvens acústicas ao redor de buracos acústicos girantes explícita estudando também as propriedades de nuvens escalares ao redor de um buraco negro de Kerr em uma cavidade. Nuvens acústicas sugerem a possibilidade de testar, experimentalmente, a existência e as propriedades de nuvens de buracos negros, usando modelos análogos. O último caso que consideramos é o sistema formado por um fluido estático localizado entre dois cilindros concêntricos, no qual o cilindro interno rotaciona com momento angular constante. Para escalas de tempo suficientemente pequenas, podemos considerar que o fluido está em repouso, mas, devido à rotação do cilindro interno, ainda podemos ter instabilidade superradiante, o que possibilita a formação de nuvens. Mostramos que para $\omega = \omega_c$ podemos encontrar nuvens para este caso, analisando o efeito da impedância do cilindro interno nestas nuvens.

Palavras-chave: Buracos negros, campos escalares, modelos análogos.

Áreas de Conhecimento: 1.05.01.03-7, 1.05.01.02-9.

Belém-Pará

2017

To the memory of

Maria Regina Couto Loureiro.

I, a universe of atoms,

an atom in the universe.

Richard Feynman

Acknowledgements

- To Prof. Luís Carlos Bassalo Crispino for the supervision since my undergraduate years.
- To Prof. Carlos Alberto Ruivo Herdeiro for the co-supervision during the time I spent on Aveiro, Portugal.
- To Prof. Edward Witten for email correspondence.
- To Eugen Radu, Sam Dolan, Luiz Leite, Ednilton de Oliveira and Mauricio Richartz for the collaboration.
- To Caio Filipe Bezerra Macedo for the love, attention and care.
- To my family for support and comprehension, specially to Mario Roberto Oliveira Benone, Maria Augusta Loureiro Benone, Maria Regina Couto Loureiro, Tatiana Loureiro Benone, Andreza Benone Maia and Mario Antônio Loureiro Benone.
- To my sister Naraiana Loureiro Benone for all kind of discussions and for the friendship.
- To my nephews João Benone Maia and Pedro Benone Maia and nieces Mariana Ferreira Benone, Luíza Benone Maia and Clarice Noha Gigena Loureiro.
- To my High School fellows from Colégio Santa Catarina de Sena (CSCS) for the friendship.
- To my friends of the dance groups Yui Soran, Fúcsia and Cia Moderno de Dança and of the percussion group Yui Daiko.
- To my friends of the Programa de Pós-Gradução em Física from Universidade Federal do Pará (PPGF-UFPA) and from the Gravity at Amazônia (Grav@zon) group for the discussions about physics and friendship.

- To my friends from the Gr@v team for the discussions and friendship.
- To the Universidade Federal do Pará (UFPA) and to the PPGF-UFPA, for the opportunity of doing Science in Brazil.
- To Coordenação de Aperfeiçoamento de Pessoal de Nível Superior (CAPES) for the financial support.
- To Marie Curie International Research Staff Exchange Scheme (IRSES) for partial financial support.
- To Universidade de Aveiro for the hospitality.

Contents

Foreword

This thesis is a result of the research developed during the years of the doctoral studies of the candidate. The research was carried out in two institutions: The Universidade Federal do Pará (UFPA), in Brazil, and the Universidade de Aveiro (UA), in Portugal. The collaboration between the two institutions was funded through the CAPES/PDSE program, which made possible for the candidate to stay ten months in the UA.

The content of this thesis is based on the following scientific papers:

- C. L. Benone, E. S. de Oliveira, S. Dolan and L. C. B. Crispino, Absorption of a massive scalar field by a charged black hole, Phys. Rev. D, vol. 89, p. 104053, 2014, 1404.0687;

- C. L. Benone, L. C. B. Crispino, C. Herdeiro and E. Radu, Kerr-Newman scalar clouds, Phys. Rev. D, vol. 90, p. 104024, 2014, 1409.1593;

- C. L. Benone, L. C. B. Crispino, C. Herdeiro and E. Radu, Acoustic clouds: standing sound waves around a black hole analogue, Phys. Rev. D, vol. 91, p. 104038, 2015, 1412.7278;

- C. L. Benone and L. C. B. Crispino, Superradiance in static black hole spacetimes, Phys. Rev. D, vol. 93, p. 024028, 2016, 1511.02634;

- C. L. Benone, E. S. de Oliveira, S. Dolan and L. C. B. Crispino, Addendum to "Absorption of a massive scalar field by a charged black hole", Phys. Rev. D, vol. 95, p. 044035, 2017, 1702.06591;

- L. C. S. Leite, C. L. Benone and L. C. B. Crispino, Scalar absorption by charged rotating black holes. Submitted for publication;

- M. Richartz, C. Herdeiro, C. L. Benone and L. C. B. Crispino, Stationary scalar clouds in a static fluid. To be published;

and the following conference proceedings:

- C. L. Benone, L. C. B. Crispino, C. Herdeiro and E. Radu, Stationary bound states of massless scalar fields around black holes and black hole analogues, Int. J. Mod. Phys. D, vol. 24, p. 1542018, 2015;

- C. L. Benone, Stationary configurations around charged rotating black holes, Int. J. Mod. Phys. D, vol. 25, p. 1641012, 2016;

- C. L. Benone, E. S. de Oliveira, S. Dolan and L. C. B. Crispino, Absorption cross section of a massive scalar field by a Reissner-Nordström black hole. To be published;

Introduction

Stars, such as our Sun, equilibrate the gravity interaction with thermal pressure, the latter coming from fusion processes that take place inside the star. When the core becomes extremely heavy the star starts to collapse until it reaches another equilibrium state. This collapse can lead to the formation of white dwarfs, which sustain themselves by electron degeneracy pressure [1].

If a white dwarf has mass above a certain limit, the degeneracy pressure will not be enough to stop the collapse. Chandrasekhar has shown that this limit is $1.4M_{\odot}$, known as *Chandrasekhar limit*, for ideal stars [2]. Recently, Das and Mukhopadhyay have shown that strongly magnetized white dwarfs can have super-Chandrasekhar masses and established a new upper limit for the mass of white dwarfs, given by $\sim 2.58M_{\odot}$ [3]. Above this limit the collapse continues until it reachs another equilibrium state.

For stars with large initial masses a supernova explosion may take place, taking away part of the star's mass. The collapse would lead then to the formation of a more compact object: a neutron star. In this case, the star sustains itself by neutron degeneracy pressure, but, as for the white dwarf, we also have a limit for the mass of the neutron star. If the mass is above $3M_{\odot}$, which is the *Oppenheimer-Volkoff limit* [4,5], then the collapse of the star continues.

At this point the conditions of the system are so extreme that nothing can stop the collapse. The matter continues to infall to a point, i.e., to a singularity, where the curvature diverges and general relativity is no longer valid. According to the cosmic censorship conjecture, the singularity is expected to be safely hidden by a trapped surface, which is the event horizon. This astrophysical object corresponds to a black hole, one of the most important and intriguing solutions of general relativity.

The first black hole solution was published in 1916 by Karl Schwarzschild [6], in the following year of the publication of Einstein equations. The Schwarzschild black hole, as it became known, describes a static and spherically symmetric solution of Einstein's equations which depends only on the mass M of the black hole. Another black hole solution was soon discovered independently by Hans Reissner [7] and Gunnar Nordström [8], namely the Reissner-Nordström black hole solution. This solution describes the spacetime outside a static and spherically symmetric distribution of mass M and charge Q.

Since most astrophysical objects have angular momentum, we should expect a solution with rotation. It was only in 1963 that such a solution was found by Roy Kerr and therefore named after him [9]. The Kerr metric is a stationary and axially symmetric solution of the Einstein's equations which depends on the mass and on the angular momentum J of the black hole. Two years later a more general solution was found by Ezra Newman and collaborators, which depends on mass, charge and angular momentum, and was named Kerr-Newman black hole [10].

We can wonder if it is reasonable to assume a black hole to have a non zero charge. To understand this, we consider the situation of a particle, with charge e and mass μ, around a charged black hole. If

$$eQ > M\mu \tag{1}$$

then the electromagnetic repulsion will be stronger than the gravitational attraction, avoiding charges of the same sign of the black hole to be absorbed and favoring charges of the opposite sign to be absorbed, what leads to the discharge of the black hole. Knowing that for the electron $\mu/e \approx 10^{-21}$, we see that Eq. (1) is easily fulfilled and the black hole discharges quickly. Another phenomena to take into consideration is the emission of particles by black holes. Charged black holes tend to emit more particles with the same charge sign as they have than with the opposite sign, also leading to a neutralization of the hole [11].

However, in the context of minicharged dark matter [12] it is possible to have black holes with a considerable amount of charge and even extremally charged black holes [13]. Such black holes would be charged under fractional electric charge or under a hidden dark matter interaction, but would still be described by the Kerr-Newman line element.

To gain knowledge about black holes one can study how particles and fields behave around these objects. Studying the scattering of light rays by a black hole one can find the shadow cast by the black hole, which could be observed with the Event Horizon Telescope [14, 15]. Studying the scattering of fields by compact objects one finds interesting phenomena, such as the glory effect and rainbow scattering [16].

There are plenty of works on scattering and absorption by Schwarzschild black holes, including the scattering and absorption for massless [17–19] and massive [20, 21] scalar fields, fermions [22, 23], electromagnetic [24] and gravitational waves [25]. For rotating black holes there is still a lot of work to be done in this area, although some investigations have been devoted to the scattering and absorption of scalar [26–28] and gravitational fields [29] in Kerr spacetime.

For the Reissner-Nordström spacetime there is also a considerable number of studies in the literature. Nakamura and Sato [30] studied the absorption of charged and massive scalar fields in the Reissner-Nordström spacetime, finding the reflection coefficient numerically. There are also recent works that compute the absorption and scattering cross sections of Reissner-Nordström black holes for massless scalar fields [31], electromagnetic [32–34] and gravitational waves [35, 36]. Some studies on absorption by higher-dimensional Reissner-Nordström black holes can also be found in the literature [37–39].

One of the most interesting phenomena which appears in the study of scattering by compact objects is the superradiant scattering [40]. Superradiance was already known from quantum dynamics, referring to amplification of radiation due to coherence [41]. Studying the scattering of waves by an absorbing rotating body, Zel'dovich has shown that the part of the rotation energy of the object is transferred to the wave, leading to an amplification of the reflected wave [42,43]. For black holes the superradiant scattering was first studied by Misner [44], who considered the case for a Kerr black hole. Soon, it was shown that both charge and angular momentum can be extracted from the black holes and transferred to the waves [45]. The superradiant scattering was recently confirmed experimentally [46].

Based on Misner work, Press and Teukolsky proposed a rather odd scenario [47]:

Consider a rotating black hole inside a spherical mirror. Modes with $\omega < \omega_c$ will be amplified by the black hole and then reflected by the mirror. This process will continue until the mirror can no longer stand the pressure, so that the mirror breaks and releases the energy stored in the modes. This effect is called black hole bomb.

Since these black hole solutions depend only on a few parameters, how could they be the result of the collapse of objects as complex as stars? The *uniqueness theorems* tell us that the Kerr-Newman family is the only black hole family of solutions to the Einstein-Maxwell equations in electrovacuum [48–50]. These theorems led John Wheeler to state that "black holes have no hair" [51], in which the word *hair* is referring to quantities which can be measured at infinity (excluding the parameters of the Kerr-Newman family). Therefore, according to the *no-hair conjecture*, even if you start with stars with very different configurations, if they collapse to black holes with the same mass, charge and angular momentum, you cannot differ the resulting black holes.

There are several studies about the no-hair conjecture (cf., e.g., [52–56]). In particular, Jacob Bekeinstein has shown that black holes cannot support massive scalar fields in static configurations surrounding them [57]. However, if we consider a mode of a massive scalar field at the threshold of superradiant instability, that is, with $\omega = \omega_c$, we find that this mode neither increases nor decreases, but stays in a stationary orbit around the black hole. These solutions are dubbed *clouds* [58].

These clouds are real bound states, which arise from the linearized solutions of the field equations in the black hole spacetime. We can make the clouds *heavier*, by considering their backscattering on the geometry, finding hairy black holes [59, 60]. For a massive scalar field the mass gives the trapping condition, but for a massless scalar field the trapping condition can be obtained with a mirror-like condition at a certain radius. It seems very odd to consider a black hole inside a cavity, but if we consider acoustic holes [61], then this *mirror* can be simply the wall of the basin which contains the fluid.

In this work we use a partial wave approach to compute numerically the absorption cross section for three cases, namely:

(i) Massive scalar field around a Reissner-Nordström black hole [62–64];

(ii) Massive and charged scalar field around a Reissner-Nordström black hole [65];

(iii) Massless scalar field around a Kerr-Newman black hole [66].

For all these cases we are able to find the high- and low-frequency limits of the absorption cross section (semi)analytically, which we compare with our numerical results. We also analyze the superradiant regime, studying both partial and total absorption cross sections.

Regarding the clouds we consider:

(iv) Massive and charged scalar field around a Kerr-Newman black hole [67, 68];

(v) Massless scalar field in a rotating acoustic hole inside a cylindrical cavity [69, 70];

(vi) Static fluid between two cylinders, where the inner cylinder is rotating [71].

In order to find these clouds we use a shooting method.

This work is organized as follows. In Chapter 1 we give a brief review on some aspects of general relativity and the spacetimes of the black holes and analogues, presenting the equations of motion for particles in these spacetimes. In Chapter 2 we find the absorption cross section for a massive scalar field around a charged black hole. For the high-frequency limit we use the geodesics equation to find an analytical solution, as well as a sinc approximation. We also find an approximation for the low-frequency limit, which gives us two different solutions depending on the velocity of the field. In Chapter 3 we find the absorption cross section for a massive and charged scalar field around a Reissner-Nordström black hole, showing the influence of the charge of the field in the absorption cross section. In Chapter 4 we compute the absorption cross section of a massless scalar field around a charged and rotating black hole, considering different incidence angles. For off-axis incidence we separate the modes into corrotating and counterrotating ones, finding a more regular pattern for the absorption cross section. In Chapter 5 we consider the clouds formed by a massive and charged scalar field around Kerr-Newman black hole, comparing our numerical results with analytical results from the literature. In Chapter 6 we consider the acoustic clouds formed by sound waves in a cylindrical basin with shallow water. We also consider the case of scalar clouds for a massless scalar field around a Kerr black hole inside a cavity. In Chapter 7 we consider a static fluid between two concentric cylinders, with the inner cylinder rotating with constant angular momentum. We find the clouds for this case considering different values for the impedance of the inner cylinder. We assume $G = \hbar = c = 1$ throughout this thesis.

Chapter 1

General Relativity and Spacetimes

General relativity tells us that the content of energy-momentum alters the geometry of the spacetime, while the geometry determines the path followed by particles in such spacetime. This information is encompassed in the Einstein's equations,

$$R_{\kappa\nu} - \frac{1}{2} g_{\kappa\nu} R = 8\pi T_{\kappa\nu}, \tag{1.1}$$

where the left-hand side is related to the geometry and the right-hand side is related to the content of energy-momentum of the spacetime.

The Ricci tensor, $R_{\kappa\nu}$, and the Ricci scalar, R, can be written in terms of the metric, $g_{\kappa\nu}$, and derivatives of the metric, such that, in principle, for a fixed energy-momentum tensor, $T_{\kappa\nu}$, we can find the components of the metric and, hence, the spacetime.

Once we know the metric, we can find the geodesics equation, which is the equation that dictates the path followed by free particles in the spacetime. This equation is given by

$$\ddot{x}^\kappa + \Gamma^\kappa_{\nu\lambda} \dot{x}^\nu \dot{x}^\lambda = 0, \tag{1.2}$$

where the overdot denotes the derivative with respect to the affine parameter and $\Gamma^\kappa_{\nu\lambda}$ is the affine connection.

In order to find the geodesics equation we consider the Lagrangian given by

$$L = T - V = \frac{1}{2} g_{\kappa\nu} \dot{x}^\kappa \dot{x}^\nu - V, \tag{1.3}$$

which we substitute in the Euler-Lagrange equations,

$$\frac{d}{dt}\left(\frac{\partial L}{\partial \dot{x}^\lambda}\right) - \frac{\partial L}{\partial x^\lambda} = 0, \tag{1.4}$$

obtaining

$$\ddot{x}^\kappa + \Gamma^\kappa_{\nu\lambda}\dot{x}^\nu \dot{x}^\lambda = -g^{\kappa\nu}\partial_\nu V. \tag{1.5}$$

Eq. (1.5) gives us the equation of motion for a particle under the influence of an external force, but taking $V = 0$ we retrieve the geodesics equation.

1.1 Reissner-Nordström black hole

If we search for the solution outside a spherically symmetric charged distribution of matter we find the Reissner-Nordström line element, which can be written as

$$ds^2 = f dt^2 - (1/f)dr^2 - r^2(d\theta^2 + \sin^2\theta d\phi^2), \tag{1.6}$$

where

$$f = \left(1 - \frac{r_+}{r}\right)\left(1 - \frac{r_-}{r}\right), \tag{1.7}$$

with

$$r_\pm = M \pm \sqrt{M^2 - Q^2}, \tag{1.8}$$

where M and Q are the black hole mass and charge, respectively.

From Eq. (1.8) we see that if $M > Q$ we have two horizons, where r_+ is the outer (event) horizon and r_- the inner (Cauchy) horizon. For $M = Q$ we have the special case of an extremal black hole, when the two horizons coincide. For $M < Q$ both r_+ and r_- are complex and we have the case of a naked singularity, which we will not consider in this thesis.

We can wonder what is the path followed by a particle with mass μ and charge q in this spacetime. For the Reissner-Nordström black hole the electromagnetic 4-potential is given by $A^\nu = (Q/r, 0, 0, 0)$ and Eq. (1.3) is written as

$$\begin{aligned} 2L &= g_{\kappa\nu}\dot{x}^\kappa \dot{x}^\nu + 2\frac{q}{\mu}A_0\dot{x}^0, \\ &= f\dot{t}^2 - (1/f)\dot{r}^2 - r^2(\dot{\theta}^2 + \sin^2\theta\dot{\phi}^2) + 2\frac{q}{\mu}\frac{Q}{r}\dot{t}, \end{aligned} \tag{1.9}$$

where the expression for V comes from the expression for the Lorentz force law in an arbitrary coordinate system, namely

$$\mu(\ddot{x}^{\kappa} + \Gamma^{\kappa}_{\nu\lambda}\dot{x}^{\nu}\dot{x}^{\lambda}) = qF^{\kappa}{}_{\nu}\dot{x}^{\nu}, \tag{1.10}$$

where F^{κ}_{ν} is the electromagnetic tensor.

Since this geometry is spherically symmetric we can choose $\theta = \pi/2$ (equatorial plane) without loss of generality. Substituting Eq.(1.9) in the Euler-Lagrange equations (Eq. (1.4)) for $\lambda = 0$ and 3 we find

$$f\dot{t} + \frac{1}{\mu}\frac{qQ}{r} = \frac{E}{\mu}, \qquad r^2\dot{\theta} = \frac{L}{\mu}, \tag{1.11}$$

respectively, where E and L are the energy and angular momentum of the particle at infinity. For non-null curves, we have

$$\begin{aligned} g_{\kappa\nu}\dot{x}^{\kappa}\dot{x}^{\nu} &= 1, \\ f\dot{t}^2 - (1/f)\dot{r}^2 - r^2\dot{\phi}^2 &= 1. \end{aligned} \tag{1.12}$$

Substituting Eq. (1.11) in Eq. (1.12) we obtain

$$\dot{r}^2 + f\left[1 + \left(\frac{L}{\mu r}\right)^2\right] = \frac{1}{\mu^2}\left(E - \frac{qQ}{r}\right)^2, \tag{1.13}$$

which is an equation of energy balance. In order to find the orbit equation we use the chain rule, such that $\dot{r} = (dr/d\phi)\dot{\phi}$, and define $u \equiv 1/r$, obtaining

$$\left(\frac{du}{d\phi}\right)^2 = -f(u)\left(u^2 + \frac{\mu^2}{L^2}\right) + \frac{(E - qQu)^2}{L^2}, \tag{1.14}$$

where $f(u) = 1 - 2Mu + Q^2u^2$.

1.2 Kerr black hole

The Kerr metric is a stationary and axially symmetric solution of the Einstein's equations in the vacuum. It is difficult to obtain this solution directly from the Einstein's equations, but we can obtain it by doing a complex transformation in the Schwarzschild metric [1].

[1] For more details in how to obtain this metric we refer to [72].

In Boyer-Lindquist coordinates, the Kerr line element is given by

$$ds^2 = \left(1 - \frac{2Mr}{\rho^2}\right) dt^2 + \frac{4Mar\sin^2\theta}{\rho^2} dt d\phi - \frac{\rho^2}{\Delta} dr^2 - \rho^2 d\theta^2 - C \sin^2\theta d\phi^2, \tag{1.15}$$

with

$$C = r^2 + a^2 + \frac{2Mra^2 \sin^2\theta}{\rho^2} \tag{1.16}$$

and

$$\rho^2 \equiv r^2 + a^2 \cos^2\theta, \qquad \Delta \equiv r^2 - 2Mr + a^2, \tag{1.17}$$

where the black hole angular momentum is given by $J = aM$. In this case the singularity is not a point, as in the Schwarzschild case, but a ring of radius a in the equatorial plane. Taking $\Delta = 0$ we find the outer and inner horizons, i. e., the event horizon and the Cauchy horizon, which are given, respectively, by

$$r_+ = M + \sqrt{M^2 - a^2} \qquad \text{and} \qquad r_- = M - \sqrt{M^2 - a^2}. \tag{1.18}$$

Taking also $g_{tt} = 0$ we find the stationary limit surfaces, with radius given by

$$r_{S\pm} = M \pm \sqrt{M^2 - a^2 \cos^2\theta}. \tag{1.19}$$

Between r_{S+} and r_+ we have a region where nothing can stay still, but has to rotate in the same sense as the black hole rotation.

We will consider only null geodesics in the equatorial plane, in which case we have

$$2L = \left(1 - \frac{2M}{r}\right) \dot{t}^2 + \frac{4Ma}{r} \dot{t}\dot{\phi} - \frac{r^2}{\Delta} \dot{r}^2 - \left(r^2 + a^2 + \frac{2Ma^2}{r}\right) \dot{\phi}^2. \tag{1.20}$$

Substituting in the Euler-Lagrange equations we find the conserved quantities

$$\left(1 - \frac{2M}{r}\right) \dot{t} + \frac{2Ma}{r} \dot{\phi} = \frac{E}{\mu}, \tag{1.21}$$

$$-\frac{2Ma}{r} \dot{t} + \left(r^2 + a^2 + \frac{2Ma^2}{r}\right) \dot{\phi} = \frac{L}{\mu}. \tag{1.22}$$

Solving Eqs. (1.34) and (1.22) for $\dot{\phi}$ and $\dot{t}$, we obtain

$$\dot{\phi} = \frac{1}{\Delta} \left[\left(1 - \frac{2M}{r}\right) L + \frac{2Ma}{r} E \right], \tag{1.23}$$

$$\dot{t} = \frac{1}{\Delta} \left[\left(r^2 + a^2 + \frac{2Ma^2}{r}\right) E - \frac{2Ma}{r} L \right]. \tag{1.24}$$

Substituting Eqs. (1.23) and (1.24) in $g_{\kappa\nu}\dot{x}^\kappa\dot{x}^\nu = 0$, we obtain

$$\dot{r}^2 = E^2 + \frac{2M}{r^3}(L - aE)^2 - \frac{1}{r^2}(L^2 - a^2E^2). \tag{1.25}$$

Defining the impact parameter as $b \equiv L/E$, we can rewrite Eq. (1.25) as

$$\frac{\dot{r}^2}{E^2} = 1 + \frac{2M}{r^3}(b - a)^2 - \frac{1}{r^2}(b^2 - a^2) = U(r). \tag{1.26}$$

In order to find the circular orbit for light we must take $U(r) = 0$ and $U'(r) = 0$, finding

$$b_c = a\frac{(3M + r_c)}{3M - r_c}, \qquad r_c = 2M\left\{1 + \cos\left[\frac{2}{3}\cos^{-1}\left(\pm\frac{a}{M}\right)\right]\right\}, \tag{1.27}$$

where the $+$ sign is for retrograde orbits, while the $-$ sign is for direct orbits.

1.3 Kerr-Newmann black hole

We can obtain a more general black hole solution if besides rotation we also consider that the black hole possesses electric charge. This leads us to the Kerr-Newman metric, which is, as the Kerr metric, axisymmetric and stationary. To obtain this solution we consider the nonzero energy-momentum tensor $T^{\mu\nu}$, which comes from the contribution of the electromagnetic field. This solution can be obtained from a complex transformation of the Reissner-Nordström metric [72].

The line element of the Kerr-Newman black hole is

$$ds^2 = \left(1 - \frac{2Mr - Q^2}{\rho^2}\right)dt^2 + \frac{2a\sin^2\theta}{\rho^2}(2Mr - Q^2)dtd\phi - \frac{\rho^2}{\Delta}dr^2 - \rho^2 d\theta^2 - C\sin^2\theta d\phi^2, \tag{1.28}$$

with

$$\rho^2 \equiv r^2 + a^2\cos^2\theta, \qquad \Delta \equiv r^2 - 2Mr + a^2 + Q^2, \tag{1.29}$$

and

$$C = r^2 + a^2 + \frac{(2Mr - Q^2)a^2\sin^2\theta}{\rho^2}. \tag{1.30}$$

The horizons are located at

$$r_+ = M + \sqrt{M^2 - (a^2 + Q^2)} \qquad \text{and} \qquad r_- = M - \sqrt{M^2 - (a^2 + Q^2)}. \tag{1.31}$$

The background electromagnetic 4-potential is

$$A_\alpha = (rQ/\rho^2, 0, 0, -aQr\sin^2\theta/\rho^2). \tag{1.32}$$

The Lagrangian for this geometry is given by

$$2L = \left(1 - \frac{2Mr - Q^2}{\rho^2}\right)\dot{t}^2 + \frac{2a\sin^2\theta}{\rho^2}(2Mr - Q^2)\dot{t}\dot{\phi} - \frac{\rho^2}{\Delta}\dot{r}^2 - \rho^2\dot{\theta}^2 - \frac{C\sin^2\theta}{\rho^2}\dot{\phi}^2. \tag{1.33}$$

Substituting in the Euler-Lagrange equations we find the conserved quantities

$$\left(1 - \frac{2Mr - Q^2}{\rho^2}\right)\dot{t} + \frac{a\sin^2\theta}{\rho^2}(2Mr - Q^2)\dot{\phi} = E, \tag{1.34}$$

$$\frac{a\sin^2\theta}{\rho^2}(2Mr - Q^2)\dot{t} - \left(r^2 + a^2 + \frac{(2Mr - Q^2)a^2\sin^2\theta}{\rho^2}\right)\sin^2\theta\dot{\phi} = L_z. \tag{1.35}$$

One can now find the geodesics equation using the Hamilton-Jacob equations [72].

We are interested in the shadow cast by this black hole, such that we need to compute the photon orbit. For the Schwarzschild black hole the photon orbit is $r_c = 3M$, but for the Kerr-Newman black hole, due to the frame dragging of inertial frames, the photon orbit depends on how the photon falls upon the black hole. Particularly, for an observer in the equatorial plane the shadow of the black hole has a D shape [73], as can be seen in Fig. 1.1. To find the impact parameter for an arbitrary incidence we write the *impact vector* as

$$\vec{b} = [b\cos\gamma\cos\chi, b\sin\chi, -b\sin\gamma\sin\chi], \tag{1.36}$$

where γ is the incidence angle and χ is an angle defined in the plane of the shadow. For this impact parameter, we have

$$\hat{L}_z = \frac{L_z}{E} = b\sin\chi\sin\gamma, \tag{1.37}$$

and

$$\hat{\mathcal{Q}} = \frac{\mathcal{Q}}{E^2} = b^2\cos^2\chi + (b^2\sin^2\chi - a^2)\cos^2\gamma, \tag{1.38}$$

where $\mathcal{Q}$ is Carter's constant. The radial equation is given by

$$R(r) = ((r^2 + a^2) - a\hat{L}_z)^2 - \Delta((\hat{L}_z - a)^2 - \hat{\mathcal{Q}}). \tag{1.39}$$

In order to find the critical radius and the critical impact parameter we have to solve $R(r_c) = 0$ and $R'(r_c) = 0$.

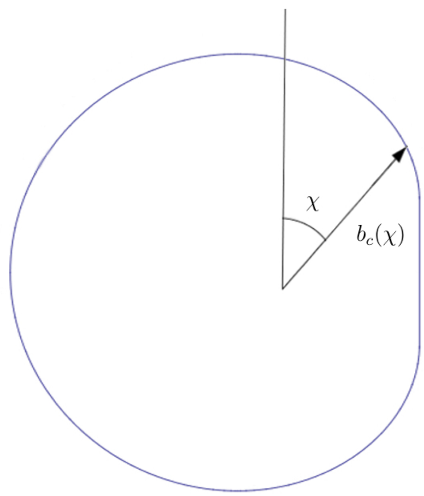

Figure 1.1: Apparent shape of an extremal Kerr-Newman black hole viewed by an observer in the equatorial plane ($\gamma = \pi/2$) at infinity.

1.4 Draining bathtub

In 1981, William Unruh published a seminal work on analogue models of black holes [61]. Unruh noticed that, using the equations of motion of a fluid, one could show that an acoustic perturbation on this fluid obeys the Klein-Gordon equation for a massless scalar field in an effective spacetime. A model considering rotation on the fluid was proposed in 1998 by Matt Visser, who considered acoustic perturbations in a rotating draining bathtub [74].

To analyse the draining bathtub, let us first consider a barotropic and inviscid fluid with flow velocity

$$\vec{v} = \frac{A}{r}\hat{r} + \frac{B}{r}\hat{\phi} \; , \tag{1.40}$$

where A is the draining and B is the circulation of the flow. For this effective spacetime we will consider $c_s = 1$, where c_s is the speed of sound in the fluid. Using the continuity and Euler equations, we can show that an acoustic perturbation obeys the Klein-Gordon equation for a massless scalar field, namely

$$\Delta\psi = \frac{1}{\sqrt{-g}}\partial_\mu \left(\sqrt{-g} g^{\mu\nu}\partial_\nu \psi\right) , \tag{1.41}$$

where the components of the metric can be obtained from the line element

$$ds^2 = \left(1 - \frac{A^2 + B^2}{r^2}\right) dt^2 - \left(1 - \frac{A^2}{r^2}\right)^{-1} dr^2 + 2Bd\phi dt - r^2 d\phi^2 \ . \tag{1.42}$$

This is not identical to the line element of a rotating black hole, but it keeps its essential features. For the spacetime associated to Eq. (1.42), the stationary limit surface is given by

$$r_S = \sqrt{A^2 + B^2}, \tag{1.43}$$

which delimits the region where the velocity of the fluid exceeds the speed of sound (c_s) [75]. The event horizon is located at

$$r_H = A, \tag{1.44}$$

which delimits a region where the radial velocity of the fluid exceeds the speed of sound. This horizon is rotating with angular velocity

$$\Omega_H = B/A^2. \tag{1.45}$$

1.5 Static fluid between cylinders

As we mentioned in Subsection 1.4, sound waves in a background flow can mimic the propagation of scalar fields in General Relativity. Assuming the fluid to be barotropic and inviscid, and the flow to be irrotational, velocity perturbations can be shown to satisfy a Klein-Gordon equation in a curved spacetime [61]. If $v = \nabla\phi$, where ϕ is a scalar field, v is the background velocity, linearized perturbations $\delta\phi$ satisfy the equation

$$\nabla_\mu \nabla^\mu \delta\phi = -\frac{1}{\sqrt{-g}} \frac{\partial}{\partial x^\mu} \left(g^{\mu\nu} \sqrt{-g} \frac{\partial \delta\phi}{\partial x^\nu} \right) = 0, \tag{1.46}$$

where

$$g^{\mu\nu} \equiv \frac{1}{\rho c_s} \left[\begin{array}{ccc} -1 & \vdots & -v^j \\ \cdots\cdots & . & \cdots\cdots\cdots \\ -v^i & \vdots & (c_s^2 \delta_{ij} - v^i v^j) \end{array} \right] \tag{1.47}$$

is the inverse background metric, ρ is the background density, c_s is the sound speed, and $g = \det(g^{\mu\nu})$. When the fluid is homogeneous and at rest, the acoustic metric is flat, and reads

$$ds^2 = \frac{\rho}{c_s}\left(-c_s^2 dt^2 + dr^2 + r^2 d\theta^2 + dz^2\right) \tag{1.48}$$

in cylindrical coordinates.

Chapter 2

Absorption of a massive and chargeless scalar field by Reissner-Nordström black holes

In this chapter we focus on the absorption cross section for a monochromatic planar wave of the neutral massive scalar field impinging upon a four-dimensional Reissner-Nordström spacetime. There are four parameters in this scenario: the mass M and charge Q of the black hole, and the mass μ and frequency ω of the field. From these quantities, we may form three dimensionless parameters: the black hole charge-to-mass ratio $|Q|/M$, with $0 \leq |Q|/M < 1$ for sub-extremal black holes, and a pair of field-to-black hole couplings, $M\omega$ and $M\mu$. Note that we adopt units in which $c = \hbar = G = 1$ so that, e.g., $M\mu \equiv M\mu/m_P^2$, where m_P is the Planck mass. We also make use of an alternative dimensionless parameter,

$$v = \sqrt{1 - \frac{\mu^2}{\omega^2}}, \tag{2.1}$$

corresponding to the ratio of the speed of propagation of the wave in the far-field to the speed of light. Here $0 < v \leq 1$ for unbound modes, for which $\omega > \mu$.

2.1 Field equations

The Klein-Gordon equation in a curved spacetime is given by

$$\nabla_\nu \nabla^\nu \Phi - \mu^2 \Phi = 0. \tag{2.2}$$

where ∇_ν denotes the covariant derivative, and indices are raised with the inverse metric $g^{\mu\nu}$.

An axially-symmetric solution to Eq. (2.2) in Reissner-Nordström spacetime can be written as

$$\Phi_{\omega l} = \frac{\psi_{\omega l}(r)}{r} P_l(\cos\theta) e^{-i\omega t}, \tag{2.3}$$

where $P_l(\cos\theta)$ is a Legendre polynomial, and $\psi_{\omega l}(r)$ obeys the radial equation

$$\frac{d^2}{dr_*^2}\psi_{\omega l} + \left[\omega^2 - V_{\text{eff}}(r)\right]\psi_{\omega l} = 0, \tag{2.4}$$

with the effective potential

$$V_{\text{eff}}(r) = f\left(\mu^2 + \frac{l(l+1)}{r^2} + \frac{2M}{r^3} - \frac{2Q^2}{r^4}\right). \tag{2.5}$$

In Eq. (2.4) we introduced the tortoise coordinate r_*, defined in the standard way by $dr_*/dr = f^{-1}$.

Equation (2.4) is a Schrödinger-like equation with an effective potential. Figure 2.1 shows V_{eff}, defined in Eq. (2.5), for $l = 0, 1$ and various values of the scalar field mass. In the far field, the potential may be expanded as $V_{\text{eff}} = \mu^2 - 2M\mu^2/r + [l(l+1) + Q^2\mu^2]/r^2 + O(r^{-3})$. The mass coupling term generates a Newtonian-like attraction at $\mathcal{O}(r^{-1})$, and the angular momentum l (and charge Q) creates a potential barrier at $\mathcal{O}(r^{-2})$. In the limit $r \to r_+$, the potential tends to zero. Figure 2.1 shows that, for moderate values of $M\mu$, the effective potential admits a local minimum and a local maximum. These features are washed out as $M\mu$ increases.

Jung and Park [20] introduced the notion of a 'critical mass' $M\mu_c = M\mu_c(Q/M, l)$, defined (for each l) as the value at which the local maximum value of V_{eff} is equal to the asymptotic value, $V_{\text{eff}}(r \to \infty) = \mu^2$. For $M\mu > M\mu_c$, all unbound modes are strongly absorbed, regardless of the frequency. In the large-l regime, the critical mass scales linearly

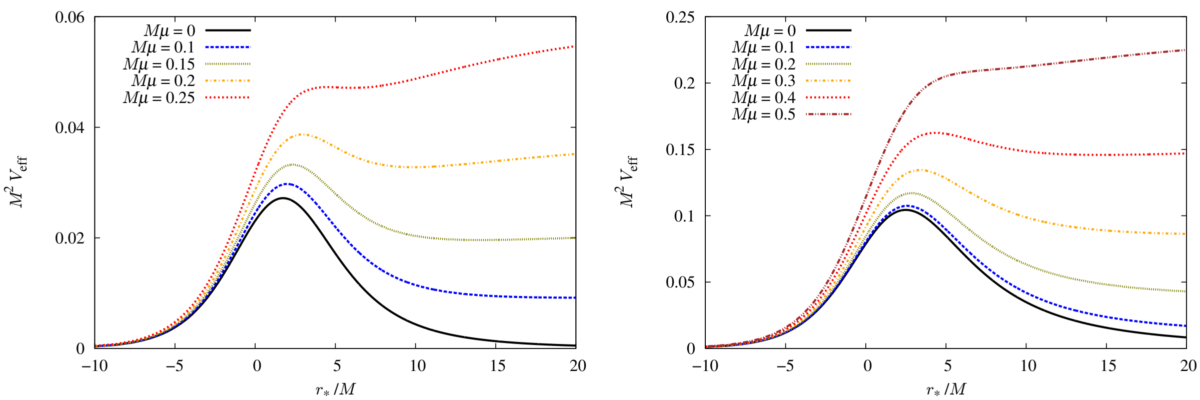

Figure 2.1: Effective potential for $q \equiv Q/M = 0.4$, $l = 0$ (left, $M\mu_c = 0.195$) and $l = 1$ (right, $M\mu_c = 0.405$) plotted for different values of the scalar field mass.

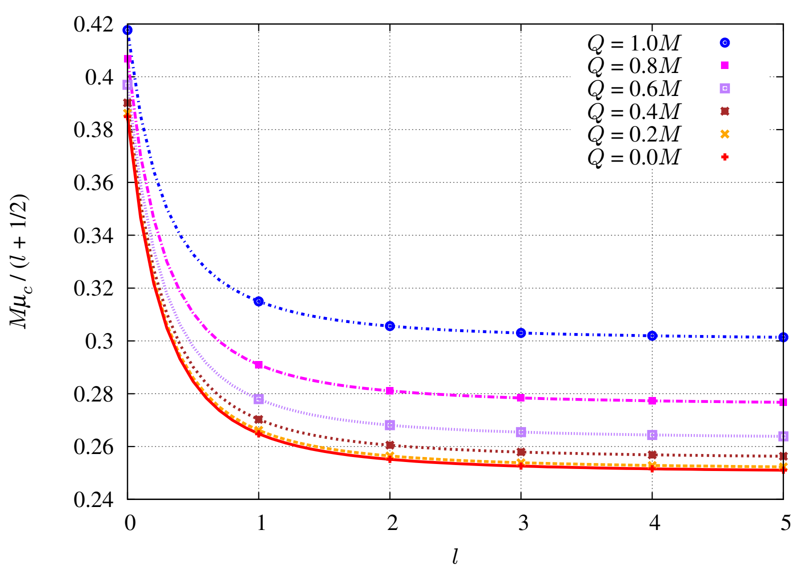

Figure 2.2: Critical mass coupling $M\mu_c$ [20] as a function of multipole l. For $l = 0$, $M\mu_c \approx 0.192$ in the Schwarzschild ($Q = 0$) case, and $M\mu_c \approx 0.209$ in the extremal Reissner-Nordström ($Q = M$) case. In the large-l regime, $M\mu_c(Q = 0, l) \approx 0.25(l + 1/2)$ and $M\mu_c(Q = M, l) \approx 0.3(l + 1/2)$.

with $l+1/2$. Figure 2.2 shows $M\mu_c/(l+1/2)$ as a function of l, determined numerically, for various black hole charge-to-mass ratios Q/M. We see that $M\mu_c$ increases with Q/M.

Let us now turn our attention to the asymptotic solutions of Eq. (2.4). Since we are interested in the absorption process, we consider only those modes which are ingoing at the outer horizon,

$$\psi_{\omega l}(r) \approx \begin{cases} \sqrt{v}\, T_{\omega l}\, e^{-i\omega r_*}, & \text{for } r \to r_+, \\ e^{-i\varrho} + R_{\omega l} e^{i\varrho}, & \text{for } r \to \infty, \end{cases} \tag{2.6}$$

where $T_{\omega l}$, $R_{\omega l}$ are complex coefficients and $\varrho = \varrho(r)$ has the leading-order expansion

$$\varrho = \omega v r + \frac{\omega M(1+v^2)}{v} \ln(2M\omega v r) + \mathcal{O}(r^0). \tag{2.7}$$

We note that the normalization of $\psi_{\omega l}(r)$ has been chosen here for later convenience. Note also that $|R_{\omega l}|^2$ and $|T_{\omega l}|^2$ may be interpreted as reflection and transmission coefficients, respectively. By considering the Wronskian of Eq. (2.6), it is straightforward to show that

$$|R_{\omega l}|^2 + |T_{\omega l}|^2 = 1, \tag{2.8}$$

representing the conservation of flux (cf. Sec. 2.2).

2.2 Absorption Cross Section

In this section we obtain an expression for the absorption cross section as a sum of partial wave contributions. We seek a monochromatic field Φ which is purely ingoing at the event horizon [cf. Eq. (2.6)] and which, in the far-field, resembles the sum of an incident planar wave Φ^I and an outgoing scattered wave Φ^S. The absorption cross section is defined as the ratio between the flux of Φ passing into the black hole, and the current of the incident wave Φ^I.

We take the incident wave Φ^I to be a monochromatic planar wave of frequency ω which, without loss of generality, we assume to be propagating along the z axis. In a Minkowski spacetime, one may write $\Phi^I_{(\mathrm{M})} = e^{-i\omega(t-vz)}$, and then make use of

$$e^{i\omega v z} = \sum_{l=0}^{\infty} (2l+1) i^l j_l(\omega v r) P_l(\cos\theta), \tag{2.9}$$

to expand in partial waves. Here $j_l(\cdot)$ is a spherical Bessel function, and $P_l(\cdot)$ is a Legendre polynomial. In the far-field, this becomes

$$\Phi^I_{(\mathrm{M})} \sim \frac{e^{-i\omega t}}{r} \sum_{l=0}^{\infty} c_{l\omega} \left(e^{-i\omega v r} + e^{-i\pi(l+1)} e^{i\omega v r} \right) P_l(\cos\theta) \tag{2.10}$$

where

$$c_{l\omega} = \frac{2l+1}{2i\omega v} e^{i\pi(l+1)}. \tag{2.11}$$

By contrast, in a black hole spacetime the long-ranged nature of the gravitational field implies that a planar wave is *distorted*, even far from the black hole. Using Eqs. (2.6) and (2.7), the analogue of a planar wave has an asymptotic form

$$\Phi^I \sim \frac{e^{-i\omega t}}{r} \sum_{l=0}^{\infty} c_{l\omega} \left(e^{-i\varrho} + e^{-i\pi(l+1)} e^{i\varrho} \right) P_l(\cos\theta). \tag{2.12}$$

The physical solution Φ is constructed from the horizon-ingoing modes (2.6) in such a way that, in the far-field, the ingoing part of Φ is matched onto the ingoing part of Φ^I. That is, we define

$$\Phi = \frac{e^{-i\omega t}}{r} \sum_{l=0}^{\infty} c_{l\omega} \psi_{\omega l}(r) P_l(\cos\theta). \tag{2.13}$$

The scattered wave $\Phi^S = \Phi - \Phi^I$ has the asymptotic form

$$\Phi^S \sim \frac{e^{-i\omega t}}{r} \hat{f}(\theta) e^{i\varrho}, \tag{2.14}$$

with a scattering amplitude $\hat{f}(\theta)$ given by

$$\hat{f}(\theta) = \frac{1}{2i\omega v} \sum_{l=0}^{\infty} (2l+1) \left(e^{i\pi(l+1)} R_{\omega l} - 1 \right) P_l(\cos\theta). \tag{2.15}$$

To find the absorption cross section, we may begin by introducing a four-current

$$J_\alpha = \frac{i}{2} \left[\Phi^* \partial_\alpha \Phi - \Phi \partial_\alpha \Phi^* \right], \tag{2.16}$$

which satisfies the conservation law $\nabla_\alpha J^\alpha = 0$, by Eq. (2.2). Now, we consider a four-volume bounded by 3-surfaces defined by $t = t_1$, $t = t_2$, $r = r_1$ and $r = r_2$ (where $t_1 < t_2$ and $r_+ < r_1 < r_2$). Applying Gauss' theorem and taking the limit $t_2 - t_1 \to 0^+$, leads to

$$\frac{d}{dt} \left\{ \int r^2 J^t dr_* d\Omega \right\} = \Big[N(r) \Big]_{r_1}^{r_2}. \tag{2.17}$$

Here, $N(r)$ is the flux passing through a surface of constant radius r, given by

$$N(r) = -\int r^2 \, J^r d\Omega. \tag{2.18}$$

We consider a stationary scenario, in which the left-hand side of Eq. (2.17) is zero, and thus $N(r_1) = N(r_2) = N$. In this case, N is (minus) the flux of particles passing into the black hole [21].

The absorption cross section σ is defined as the ratio between $|N|$ and the incident current in the planar wave, ωv. We may insert Eq. (2.13) into Eq. (2.16) and use the orthogonality of Legendre polynomials, given by

$$\int_0^\pi P_l(\cos\theta) P_{l'}(\cos\theta) \sin\theta d\theta = \frac{2}{2l+1}\delta_{ll'}, \tag{2.19}$$

to write the total absorption cross section σ as a sum of partial cross sections σ_l,

$$\sigma = \sum_{l=0}^{\infty} \sigma_l, \tag{2.20}$$

defined in terms of modal transmission/reflection coefficients by

$$\sigma_l = \frac{\pi(2l+1)}{\omega^2 v^2} |T_{\omega l}|^2 = \frac{\pi(2l+1)}{\omega^2 v^2} \left(1 - |R_{\omega l}|^2\right). \tag{2.21}$$

2.3 High-frequency regime

In the limit of high frequency, the wavelength of the field becomes very small in comparison with the scale of the black hole (e.g. the horizon radius). Under the eikonal approximation, a wavefront propagates along geodesics of the spacetime [76]. The 'geodesic capture cross section' is defined as $\sigma_{\text{hf}} = \pi b_c^2$, where b_c is the critical impact parameter corresponding to the unbound geodesic which asymptotically approaches the unstable circular orbit at $r = r_c$. The critical impact parameter may be found by solving the orbital equation for a timelike geodesic in the Reissner-Nordström spacetime. Let us start from the 'energy' balance equation, which we can find by making $q = 0$ in Eq. (1.13), such that

$$\dot{r}^2 = \frac{E^2}{\mu^2} - f\left[1 + \left(\frac{L}{\mu r}\right)^2\right] \equiv V_r. \tag{2.22}$$

Now, we introduce the impact parameter $b \equiv L/(Ev)$, where $v^2 = 1-\mu^2/E^2$, which allows us to write

$$\frac{\mu^2}{L^2}\dot{r}^2 = \frac{1}{b^2v^2} - f\left(\frac{1-v^2}{b^2v^2} + \frac{1}{r^2}\right). \tag{2.23}$$

To obtain b_c, the critical impact parameter, and r_c, the radius of the unstable circular orbit (or 'critical radius'), we set this equation and its radial derivative to zero. This yields

$$b_c = \frac{r_c}{v f_c^{1/2}}\left[1-(1-v^2)f_c\right]^{1/2}, \tag{2.24}$$

where $f_c = f(r_c)$, and a quartic equation for r_c, namely,

$$r_c^4 + M\frac{(1-4v^2)}{v^2}r_c^3 + \left(\frac{4(v^2-1)}{v^2}M^2 + 2Q^2\right)r_c^2 + \frac{4MQ^2(1-v^2)}{v^2}r_c + \frac{Q^4(v^2-1)}{v^2} = 0. \tag{2.25}$$

We seek a root of Eq. (2.25) that is larger than the outer horizon, i.e., $r_c > r_+$, and which corresponds to the peak of the potential barrier from Eq. (2.23). This root may be found numerically. Figure 2.3 shows the critical radius as a function of v for various charge-to-mass ratios Q/M. We see that, in general, r_c decreases as v increases, and as Q/M increases.

In the limit $v \to 0$, the critical impact parameter b_c diverges as $1/v$. Let us therefore introduce a dimensionless 'absorption function' $F(v,Q) = v^2 b_c^2/M^2$, which is regular in this limit, so that in the high-frequency limit

$$\sigma \to \sigma_{\mathrm{hf}} = v^{-2}F(v,Q)\,\pi M^2. \tag{2.26}$$

In the null geodesic case ($v=1$) [32],

$$F(1,Q) = \frac{\left(3+\sqrt{9-(Q/M)^2}\right)^4}{8\left(3-2(Q/M)^2+\sqrt{9-8(Q/M)^2}\right)}. \tag{2.27}$$

In the Schwarzschild case ($Q=0$) [23],

$$F(v,0) = \frac{1}{4}\frac{(4v^2-1+\sqrt{1+8v^2})^2}{\sqrt{1+8v^2}-1}\left(3+\sqrt{1+8v^2}\right). \tag{2.28}$$

In the extremal case ($Q=M$),

$$F(v,M) = \chi^2\frac{v^2+\frac{2(1-v^2)}{\chi}-\frac{(1-v^2)}{\chi^2}}{1-\frac{2}{\chi}+\frac{1}{\chi^2}}, \tag{2.29}$$

where

$$\chi = \frac{1}{6}\frac{\kappa^{1/3}}{v^2} + \frac{2}{3}\frac{(3v^2+1)}{v^2\kappa^{1/3}} + \frac{1}{3}\frac{(3v^2-1)}{v^2} \tag{2.30}$$

and

$$\kappa = -36v^2 + 108v^4 - 8 + 12\sqrt{(27v^4 - 22v^2 - 5)3}\,v^2. \tag{2.31}$$

In the limit $v \to 0$, we may find r_c by solving the cubic

$$x^3 - 4x^2 + 4(Q/M)^2 x - (Q/M)^4 = 0, \tag{2.32}$$

where $x = r_c/M$, and substituting the solution into Eq. (2.24) to obtain b_c and thus $F(0, Q)$.

In the general case $(v, Q \neq 0, M)$, one may compute the values of the critical ray by finding the numerical solution of Eq. (2.25). We find that the absorption function $F(v, Q)$ varies smoothly, as shown in Fig. 2.4.

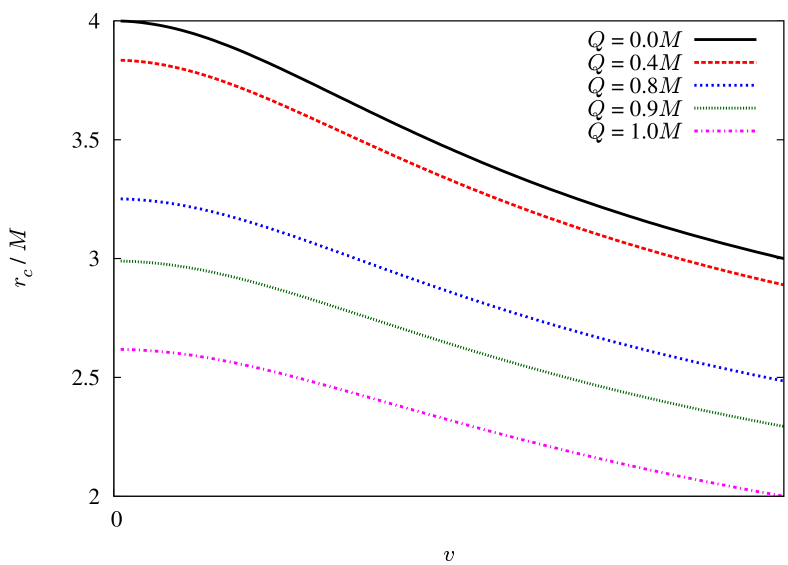

Figure 2.3: Radius of the unstable circular orbit, r_c, as a function of incident speed v for a range of charge-to-mass ratios Q/M.

2.3.1 Sinc approximation

In the high-frequency regime the absorption cross section exhibits regular oscillations (with ω) around the limiting value (see e.g. Fig. 2.6). In the case of a massless scalar field

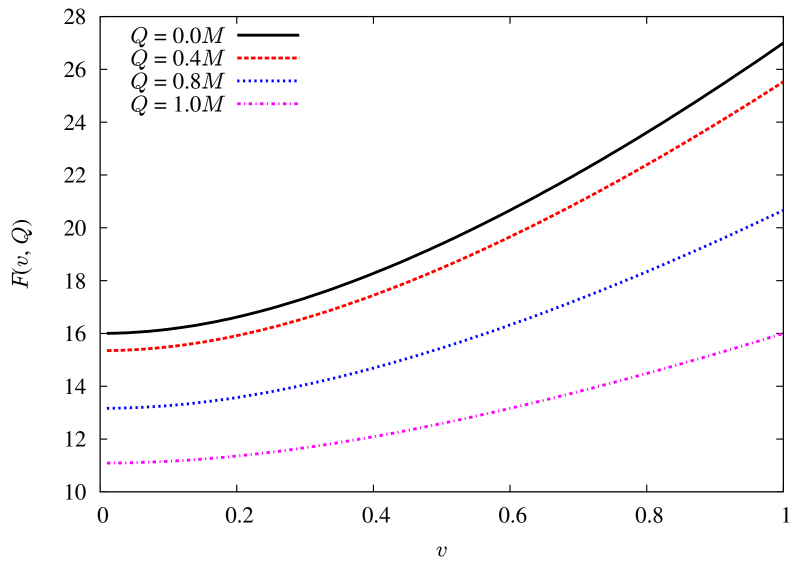

Figure 2.4: Absorption function $F(v, Q)$ as a function of the incident speed v for various charge-to-mass ratios Q/M. $F(v, Q)$ determines the high-frequency absorption cross section via Eq. (2.26). For closed-form solutions in limits $v \in \{0, 1\}$, $Q/M \in \{0, 1\}$ see Eqs. (2.27)–(2.29).

absorbed by a Schwarzschild BH, Sanchez [18] found that a simple formula provided a good fit at high frequencies,

$$\sigma_{\rm hf}^{(Q=0,v=1)} \approx 27\pi M^2 \left[1 - \hat{\alpha}\,\mathrm{sinc}(2\pi\sqrt{27}M\omega)\right], \tag{2.33}$$

where $\mathrm{sinc}(x) \equiv \sin(x)/x$ and $\hat{\alpha} \approx \sqrt{32/27}$ (see Eq. (30) in Ref. [18]). Decanini, Folacci and coworkers [77, 78] have applied the complex angular momentum approach to analyse the absorption cross section. They recovered Sanchez's result in the high-frequency regime, with a more accurate coefficient of $\hat{\alpha} = 8\pi e^{-\pi}$, and gave higher-order corrections. Furthermore, in Ref. [77] it was shown that regular oscillations are a universal feature of cross sections for massless fields absorbed by spherically-symmetric BHs.

We now seek to extend the complex angular momentum analysis to the massive-field case (see also Ref. [79]). As before, the oscillatory contribution to the cross section is related to a sum of the residues of so-called Regge poles, and the asymptotic properties of the Regge pole spectrum may be determined by the geodesic analysis. We used the approach of Ref. [80] to show that, in the high-frequency regime, the Regge pole λ_n is

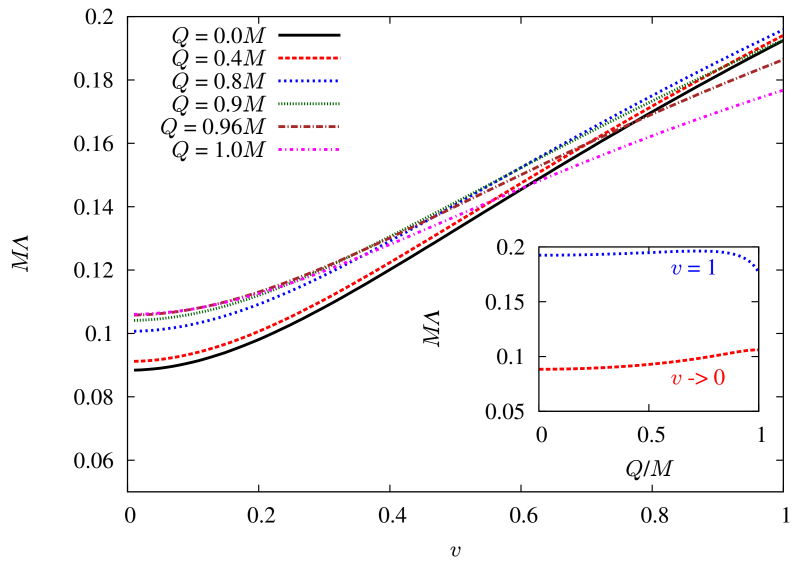

Figure 2.5: Lyapunov exponent Λ associated with the peak in the potential barrier. The inset shows the exponent as a function of Q/M in the nearly-bound ($v \to 0$) and null ($v = 1$) cases.

approximately

$$\lambda_n = v b_c \omega + i(n + 1/2)\hat{\beta} + \mathcal{O}(\omega^{-1}), \tag{2.34}$$

where $\hat{\beta} = v b_c \Lambda$ and Λ is the Lyapunov exponent [81] associated with the unstable circular orbit, i.e.,

$$\Lambda = \frac{1}{\dot{t}}\sqrt{\frac{1}{2}\frac{d^2 V_r}{dr^2}} = \frac{v f_c}{r_c}\sqrt{k_c}, \tag{2.35}$$

where

$$\begin{aligned} k_c \quad = \quad & \frac{1}{v^2 r_c^4 f_c}\left\{(4v^2 - 1)M r_c^3 + [8M^2(1 - v^2) - 4Q^2 v^2] r_c^2 \right. \\ & \left. -12MQ^2(1 - v^2) r_c + 4Q^4(1 - v^2)\right\}. \end{aligned} \tag{2.36}$$

The Lyapunov exponent is shown in Fig. 2.5.

Following the steps in Ref. [77], it is possible to show that the high-frequency approximation to the cross section is given by

$$\sigma_{\text{hf}} \approx \frac{F(v, q)\pi M^2}{v^2}\left[1 - 8\pi\hat{\beta}e^{-\pi\hat{\beta}}\,\text{sinc}\,(2\pi v b_c \omega)\right]. \tag{2.37}$$

This approximation is compared with numerically-determined cross sections in Fig. 2.8, showing excellent agreement.

2.4 Low-frequency regime

In this section we analyze the low-frequency limit of the Reissner-Nordström absorption cross section for the massive chargeless scalar field, following the method of Ref. [21]. The results obtained in this section are valid in the regime where the incident wavelength of the scalar field is much larger than the radius of the black hole.

We will first analyze the case for general Reissner-Nordström black holes ($r_+ > r_- > 0$) and then specialize to the cases of the Schwarzschild ($Q = 0$, $r_+ = 2M$, $r_- = 0$) and extreme Reissner-Nordström black holes ($Q = M$, $r_+ = r_- = M$).

We consider three different regions: the region very close to the black hole (region I), an intermediate region, in which the frequency and mass terms are much smaller than the other contributions in Eq. (2.4) (region II), and a region distant from the black hole (region III). We match together the solutions in these three regions to get a global solution.

2.4.1 General case

We may rewrite the differential equation (2.4) as

$$\frac{f}{r^2}\frac{d}{dr}\left(fr^2\frac{d}{dr}\varphi\right) + (\omega^2 - V_{RN}(r))\varphi = 0, \tag{2.38}$$

where $\varphi = r^{-1}\psi_{\omega l}$ [cf. Eq. (2.3)] and

$$V_{RN} = f\left(\mu^2 + \frac{l(l+1)}{r^2}\right). \tag{2.39}$$

For region I ($r \approx r_+$), Eq. (2.38) is approximately

$$\frac{d^2\varphi}{dr_*^2} + \omega^2\varphi = 0, \tag{2.40}$$

with $\varphi^I_{RN} \propto e^{-i\omega r_*}$ representing a transmitted wave. We may write the tortoise coordinate explicitly as a function of r, as

$$r_* = r + \frac{r_+^2}{r_+ - r_-}\ln(r - r_+) - \frac{r_-^2}{r_+ - r_-}\ln(r - r_-), \tag{2.41}$$

after fixing the constant of integration appropriately. Let us consider the dominant term of Eq. (2.41), for $r \to r_+$,

$$r_* \sim \frac{r_+^2}{r_+ - r_-}\ln(r - r_+) + r_*^{(0)} \tag{2.42}$$

where $r_*^{(0)}$ is a constant, so that

$$\varphi_{RN}^{I} = A_{\rm RN}^{\rm tra} \, |r - r_+|^{-i\omega\alpha} \,. \tag{2.43}$$

Here $A_{\rm RN}^{\rm tra}$ is a complex constant, and $\alpha = r_+^2/(r_+ - r_-)$.

In order to find the solution in region II we take the limit $\omega \to 0$, $\mu \to 0$ in Eq. (2.38). Since we are interested in computing the absorption cross section in the limit $M\omega, M\mu \ll 1$, we may restrict ourselves to the $l = 0$ mode, which is the dominant term in this limit [1]. Thus, the differential equation reduces to

$$\frac{d^2}{dr^2}\varphi_{RN} - \frac{(r_+ + r_- - 2r)}{(r - r_+)(r - r_-)}\frac{d}{dr}\varphi_{RN} = 0, \tag{2.44}$$

with solution given by

$$\varphi_{RN}^{II} = \zeta \ln\left(\frac{r - r_+}{r - r_-}\right) + \tau. \tag{2.45}$$

where ζ and τ are constants to be determined.

We now seek an overlap between the solutions in regions I and II. We may rewrite Eq. (2.43) as

$$\varphi_{RN}^{I} \approx A_{\rm RN}^{\rm tra} \left(1 - i\omega\alpha \ln(r - r_+)\right). \tag{2.46}$$

If we take the limit $r \to r_+$ in Eq. (2.45) we obtain

$$\varphi_{RN}^{II} = \zeta \ln(r - r_+) - \zeta \ln(r_+ - r_-) + \tau. \tag{2.47}$$

Comparing Eqs. (2.46) and (2.47) yields

$$\begin{aligned} \zeta &= -i\omega\alpha A_{\rm RN}^{\rm tra}, \\ \tau &= (1 - i\omega\beta)\, A_{\rm RN}^{\rm tra}, \end{aligned} \tag{2.48}$$

where $\beta = \alpha \ln(r_+ - r_-)$.

For region III ($r \gg r_+$) we can rewrite Eq. (2.38) as

$$\left\{\frac{d^2}{dr^2} + \left[(\omega^2 - \mu^2) + \frac{2M(2\omega^2 - \mu^2)}{r} - \frac{l(l+1)}{r^2}\right]\right\} r f^{1/2}\varphi = 0, \tag{2.49}$$

[1] In Ref. [21] it is shown that the low-frequency limit of the transmission coefficient for small black holes behaves as ω^{2l+2}, so that the $l = 0$ contribution is dominant in this limit.

where we neglect terms of $\mathcal{O}\left(1/r^2\right)$ that are proportional to ω^2 and μ^2, and terms of order $1/r^3$ and higher. The solution to the above equation can be written as:

$$\varphi_{RN}^{III} = a\frac{F_l(\eta, \omega v r)}{r} + b\frac{G_l(\eta, \omega v r)}{r}, \tag{2.50}$$

where $\eta = -M\omega(1+v^2)/v$, and $F_l(\eta, x)$ and $G_l(\eta, x)$ are the regular and irregular Coulomb wave functions, respectively [82]. In the far-field, we may write

$$\varphi_{RN}^{III} \approx A_{\rm RN}^{\rm ref} e^{i\vartheta} + A_{\rm RN}^{\rm inc} e^{-i\vartheta}, \tag{2.51}$$

where $\vartheta = \omega v r - l\pi/2 - \eta \ln(2M\omega v r) + \arg\Gamma(l + 1 + i\eta)$. Here $A_{\rm RN}^{\rm inc}$ and $A_{\rm RN}^{\rm ref}$ are related to a and b by

$$A_{\rm RN}^{\rm inc} = \frac{-a + ib}{2i}, \qquad A_{\rm RN}^{\rm ref} = \frac{a + ib}{2i}. \tag{2.52}$$

For $\omega r \ll 1$ and $l = 0$, Eq. (2.50) reduces to

$$\varphi_{RN}^{III} = a\varpi\omega v + \frac{b}{\varpi r}, \tag{2.53}$$

where we have used for the Coulomb wave functions

$$F_0(\eta, x) = \varpi x, \qquad G_0(\eta, x) = \frac{1}{\varpi}, \tag{2.54}$$

and

$$\varpi^2 = \frac{2\pi\eta}{e^{2\pi\eta} - 1} = \frac{-2\pi M\omega(1 + v^2)/v}{e^{-2\pi M\omega(1+v^2)/v} - 1}. \tag{2.55}$$

In the asymptotic limit, Eq. (2.45) becomes

$$\varphi_{RN}^{II} = -\zeta\frac{r_+ - r_-}{r} + \tau. \tag{2.56}$$

Using Eqs. (2.48), (2.53) and (2.56), we find

$$\begin{aligned} a &= \tfrac{A_{\rm RN}^{\rm tra}}{\varpi\omega v}\left(1 - i\omega\beta\right), \\ b &= i r_+^2 \omega\varpi A_{\rm RN}^{\rm tra}. \end{aligned} \tag{2.57}$$

We substitute Eq. (2.57) in Eq. (2.52) and obtain

$$\begin{aligned} A_{\rm RN}^{\rm inc} &= -A_{\rm RN}^{\rm tra}\tfrac{\left(1 + r_+^2\omega^2\varpi^2 v - i\omega\beta\right)}{2i\varpi\omega v}, \\ A_{\rm RN}^{\rm ref} &= A_{\rm RN}^{\rm tra}\tfrac{\left(1 - r_+^2\omega^2\varpi^2 v - i\omega\beta\right)}{2i\varpi\omega v}. \end{aligned} \tag{2.58}$$

The reflection coefficient is given by

$$|R_{\omega l}|^2 = \left|\frac{A^{\rm ref}_{\rm RN}}{A^{\rm inc}_{\rm RN}}\right|^2 = \left|\frac{1 - r_+^2\omega^2\varpi^2 v - i\omega\beta}{1 + r_+^2\omega^2\varpi^2 v - i\omega\beta}\right|^2, \tag{2.59}$$

which, recalling Eq. (2.21), gives for the absorption cross section, for $l = 0$, in the approximation $\omega \approx 0$ and $m \approx 0$:

$$\sigma = \frac{\pi}{\omega^2 v^2}\left(\frac{4r_+^2\omega^2\varpi^2 v}{(1 + r_+^2\omega^2\varpi^2 v)^2 + \omega^2\beta^2}\right). \tag{2.60}$$

We can take only the first term in the denominator of Eq. (2.60) and write

$$\sigma = \frac{4\pi r_+^2\varpi^2}{v} = \frac{4(\pi r_+)^2(2M\mu)(1+v^2)}{v^2\sqrt{1-v^2}\left\{1 - \exp\left(-\frac{2\pi M\mu(1+v^2)}{v\sqrt{1-v^2}}\right)\right\}}, \tag{2.61}$$

where we also wrote ω in terms of v.

For velocities above $v_c = 2\pi M\mu$ we can make the expansion

$$1 - \exp\left(-\frac{2\pi M\mu(1+v^2)}{v\sqrt{1-v^2}}\right) = \frac{2\pi M\mu(1+v^2)}{v\sqrt{1-v^2}}. \tag{2.62}$$

Substituting Eq. (2.62) in Eq.(2.61), we obtain

$$\sigma^{(1)}_{\rm lf} = \frac{\mathcal{A}}{v}, \tag{2.63}$$

where $\mathcal{A} = 4\pi r_+^2$ is the area of the Reissner-Nordström black hole. If we consider now the limit $v \to 0$ in Eq. (2.61), we obtain

$$\sigma^{(2)}_{\rm lf} = \frac{4(\pi r_+)^2(2M\mu)}{v^2}. \tag{2.64}$$

We then have for the low-frequency limit

$$\sigma_{\rm lf} = \begin{cases} \sigma^{(1)}_{\rm lf} = \mathcal{A}/v, & v \gtrsim v_c, \\ \sigma^{(2)}_{\rm lf} = \frac{4(\pi r_+)^2(2M\mu)}{v^2}, & v \lesssim v_c, \end{cases} \tag{2.65}$$

where v_c is the transition velocity. If we take $\mu = 0$ in Eq. (2.65) we see that $\sigma^{(1)}_{\rm lf} = \mathcal{A}$, while $\sigma^{(2)}_{\rm lf} = 0$, retrieving the general result for the low-frequency absorption cross section of massless scalar fields [83, 84].

2.4.2 Schwarzschild case

Having outlined the procedure for the Reissner-Nordström case in the previous subsection, we can directly find the results for the Schwarzschild case by inserting $r_+ = 2M$ and $r_- = 0$ in the previous expressions. We have then, from Eq. (2.61),

$$\sigma = \frac{4\pi(2M)^2\varpi^2}{v} = \frac{(4M\pi)^2(2M\mu)(1+v^2)}{v^2\sqrt{1-v^2}\left\{1-\exp\left(-\frac{2\pi M\mu(1+v^2)}{v\sqrt{1-v^2}}\right)\right\}} \tag{2.66}$$

Taking the appropriate limits of Eq. (2.66), we obtain

$$\sigma_{\text{lf}} = \begin{cases} \sigma_{\text{lf}}^{(1)} = 16\pi/v, & v \gtrsim v_c, \\ \sigma_{\text{lf}}^{(2)} = \frac{(4M\pi)^2(2M\mu)}{v^2}, & v \lesssim v_c. \end{cases} \tag{2.67}$$

These results were originally obtained by Unruh, in 1976 [21].

2.4.3 Extreme case

For the extreme Reissner-Nordström case, in which $r_+ = r_-$, we can repeat the procedure of subsection 2.4.1 with minor modifications. We have Eq. (2.38) with $V_{RN} \to V_e$, where

$$V_e = \left(1 - \frac{M}{r}\right)^2 \left(\mu^2 + \frac{l(l+1)}{r^2}\right). \tag{2.68}$$

The tortoise coordinate for the extreme case is

$$r_* = r + 2M\ln(r-M) - \frac{M^2}{r-M}. \tag{2.69}$$

We consider only the dominant term of Eq. (2.69), for $r \to M$, i.e.,

$$r_* = -\frac{M^2}{r-M} + r_*^{(0)}. \tag{2.70}$$

The solution in region I is given by

$$\varphi_e^I = A_e^{\text{tra}} \exp\left[i\omega M^2/(r-M)\right]. \tag{2.71}$$

For region II, the radial equation reduces to

$$\frac{d^2}{dr^2}\varphi_e + \frac{2}{(r-M)}\frac{d}{dr}\varphi_e = 0, \tag{2.72}$$

with solution given by

$$\varphi_e^{II} = \frac{\zeta_e}{r-M} + \tau_e. \tag{2.73}$$

If we take the limit $\omega \to 0$ in Eq. (2.71), we obtain

$$\varphi_e^{I} = A_e^{\rm tra}\left(1 + i\frac{\omega M^2}{r-M}\right). \tag{2.74}$$

Comparing Eqs. (2.73) and (2.74) yields

$$\begin{aligned}\zeta_e &= i\omega M^2 A_e^{\rm tra},\\ \tau_e &= A_e^{\rm tra}.\end{aligned} \tag{2.75}$$

For region *III* we have again the solution (2.50) and for low frequencies we have Eq. (2.53). Considering Eq. (2.73) in the limit $r \to \infty$, we obtain

$$\varphi_e^{II} = \frac{\zeta_e}{r} + \tau_e. \tag{2.76}$$

Using Eqs. (2.53), (2.75) and (2.76), we find

$$\begin{aligned}a &= A_e^{\rm inc}/(\varpi\omega v),\\ b &= iM^2\omega\varpi A_e^{\rm inc}.\end{aligned} \tag{2.77}$$

We substitute Eq. (2.77) in Eq. (2.52) to obtain

$$\begin{aligned}A_e^{\rm inc} &= -A_e^{\rm tra}\tfrac{\left(1+M^2\omega^2\varpi^2 v\right)}{2i\varpi\omega v},\\ A_e^{\rm ref} &= A_e^{\rm tra}\tfrac{\left(1-M^2\omega^2\varpi^2 v\right)}{2i\varpi\omega v},\end{aligned} \tag{2.78}$$

which gives us for the absorption cross section, for $l = 0$,

$$\sigma = \frac{\pi}{\omega^2 v^2}\left(\frac{4M^2\omega^2\varpi^2 v}{(1+M^2\omega^2\varpi^2 v)^2}\right), \tag{2.79}$$

in the low-frequency regime. Considering only the first term in the denominator of Eq. (2.79) and writing ω in terms of v, we are left with

$$\sigma = \frac{4\pi M^2\varpi^2}{v} = \frac{4(\pi M)^2(2M\mu)(1+v^2)}{v^2\sqrt{1-v^2}\left\{1-\exp\left(-\frac{2\pi M\mu(1+v^2)}{v\sqrt{1-v^2}}\right)\right\}}. \tag{2.80}$$

Taking the appropriate limits, we obtain

$$\sigma_{\rm lf} = \begin{cases}\sigma_{\rm lf}^{(1)} = 4\pi M^2/v, & v \gtrsim v_c,\\ \sigma_{\rm lf}^{(2)} = \frac{4(\pi M)^2(2M\mu)}{v^2}, & v \lesssim v_c.\end{cases} \tag{2.81}$$

2.5 Numerical computations

In this section we present numerical results for the absorption cross section, obtained by solving the radial equation, Eq. (2.4), numerically for general frequencies. We integrate the solution from (close to) the event horizon to a large r. By matching the numerical solutions onto the asymptotic forms in Eq. (2.6), we obtain the reflection and transmission coefficients and, via Eqs. (2.20)–(2.21), and therefore the absorption cross section of the massive chargeless scalar field for the Reissner-Nordström spacetime.

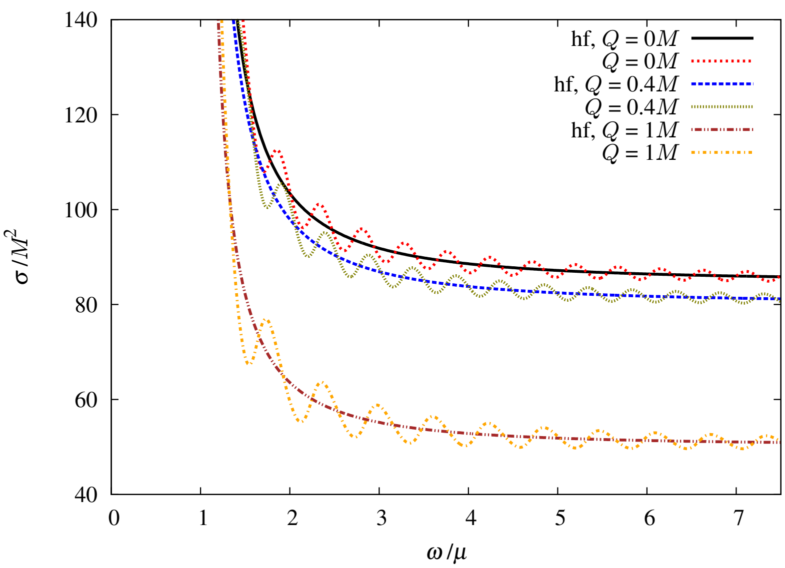

Figure 2.6: Total absorption cross section for $M\mu = 0.4$ and for different values of the black hole charge Q. We also plot the classical (high-frequency) limit $\sigma_{\rm hf}$ in each case.

In Fig. 2.6 we compare the scalar-wave absorption cross section with the geodesic capture cross section $\sigma_{\rm hf} = \pi b_c^2$ [cf. Eq. (2.26)]. We see that σ exhibits regular oscillations around $\sigma_{\rm hf}$. We note that the critical impact parameter b_c, and hence also the absorption cross section, diminishes as the the charge-to-mass ratio Q/M increases. This is in agreement with results for the non-massive case [31].

In Fig. 2.7 we examine the effect of varying the mass of the scalar field μ. We see that, in the case $M\mu > M\mu_c(Q,l)$, the cross section diverges as $1/v^2$ in the limit $\omega \to \mu$, as expected from Eq. (2.21). As described in Sec. 2.4, in the very low-frequency regime the cross section instead diverges as $1/v$. In the high-frequency limit ($\omega \gg 1$ and $\omega/\mu \gg 1$ [or

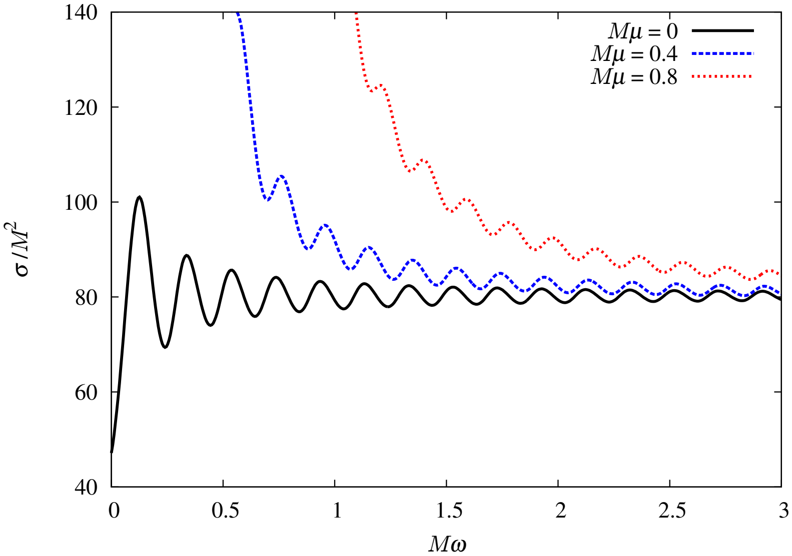

Figure 2.7: Total absorption cross section for $Q/M = 0.4$ and different values of $M\mu$.

equivalently $v \to 1$]), Fig. 2.7 shows that the massive results converge to their massless counterparts.

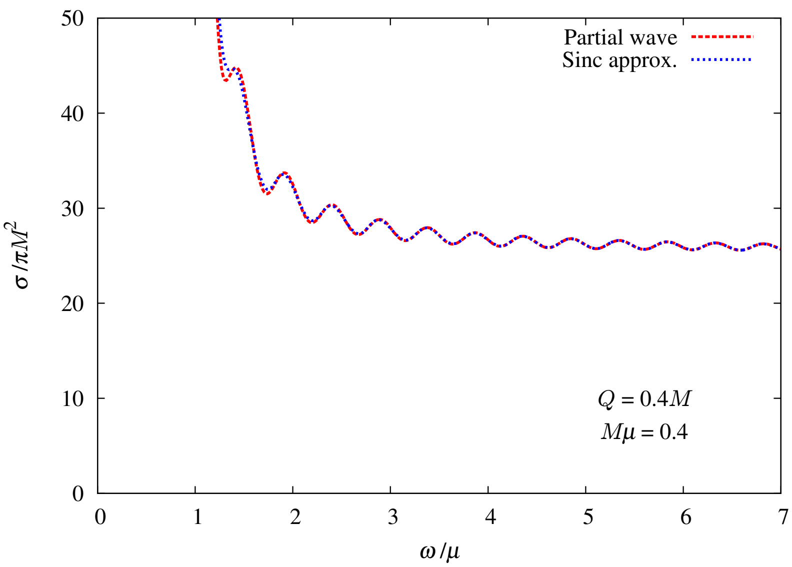

Figure 2.8: Comparison of the 'sinc approximation', Eq. (2.37), with numerical results from the partial-wave method, for the case $M\mu = 0.4$, $Q/M = 0.4$. Similar levels of agreement are found for all Q/M, in the moderate-to-large ω regime.

Figure 2.8 shows that the oscillations in the cross section are well modelled by the sinc approximation in Eq. (2.37). As anticipated [cf. Eq. (2.37)], the width of the oscillation (in ω) approaches $1/(vb_c)$ in the limit $\omega \to \infty$.

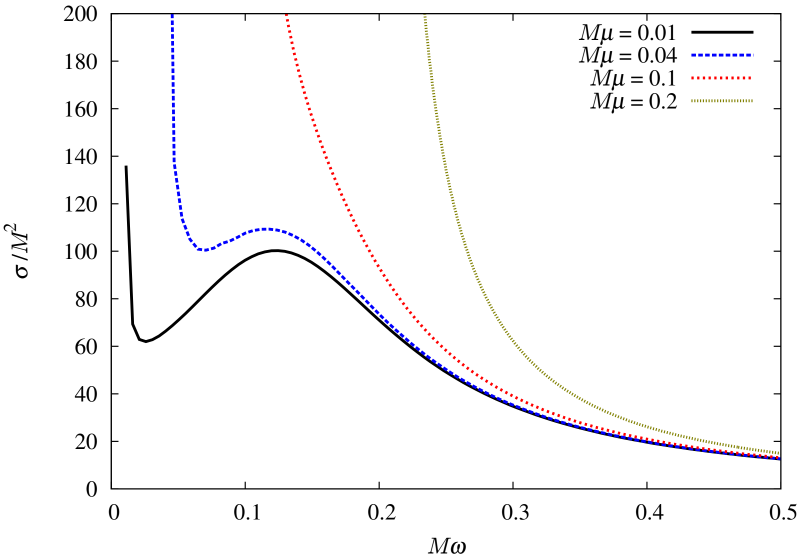

Figure 2.9: Partial absorption cross section for the monopole ($l = 0$) mode for charge-to-mass ratio $Q/M = 0.4$, and four choices of $M\mu$. Note that the local minimum disappears as $M\mu$ increases above $M\mu_c = 0.195$.

In Fig. 2.9 we show the partial absorption cross section for $l = 0$ and different values of the mass coupling $M\mu$, above and below the critical mass $M\mu$ [for $Q/M = 0.4$ and $l = 0$, $(M\mu)_c = 0.195$]. For $M\mu < M\mu_c$ the absorption cross section presents a local minimum. For $M\mu \gtrsim (M\mu)_c$, $\sigma_{l=0}$ becomes a monotonic function of the frequency.

In Fig. 2.10 we compare the partial absorption cross section for $l = 0$ with the analytical results given by Eq. (2.65) for $Q/M = 0.4$ and $M\mu = 0.04$, showing that the the low-frequency limit of the absorption cross section transits smoothly from $\sigma_{\text{lf}}^{(1)}$ to $\sigma_{\text{lf}}^{(2)}$ around v_c.

Figures 2.11 and 2.12 show the total and partial absorption cross section for $M\mu = 0.04$ and $M\mu = 0.4$, respectively. For $M\mu = 0.04$ we see that the monopole ($l = 0$) gives the main contribution for $\omega/\mu \lesssim 5$. As shown in Sec. 2.4, in the low-frequency limit the absorption cross section tends to A/v, which diverges as $\omega \to \mu$. For $M\mu = 0.4$ we see that both the partial cross sections for $l = 0$ and $l = 1$ diverge in this limit. This occurs because the value of the mass coupling in this case is very close to the critical mass for

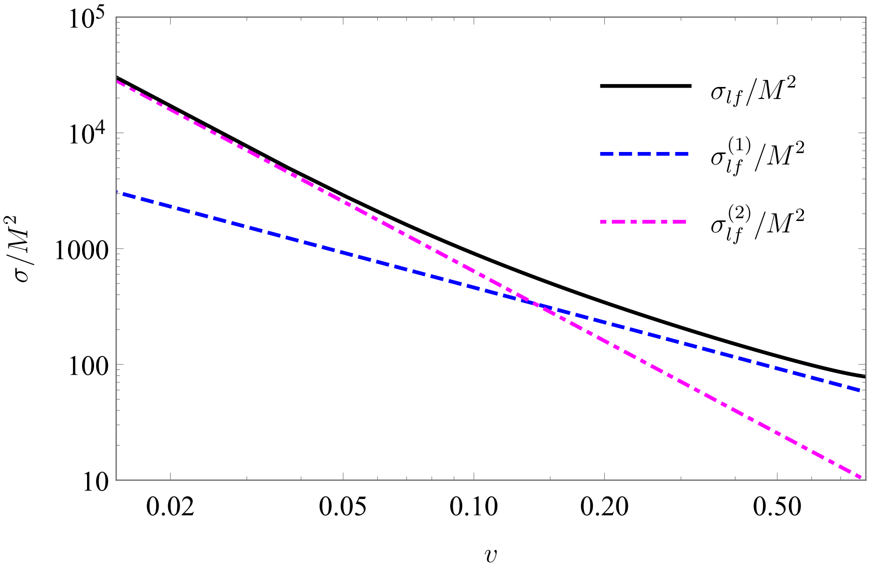

Figure 2.10: Comparison between the partial absorption cross section $\sigma_{l=0}$ [solid line], and the approximate analytical results of Eq. (2.65) [broken lines], for the case $Q/M = 0.4$ and $M\mu = 0.022$. A transition in behavior is visible near $v_c \approx 0.138$.

$l = 1$ [for $Q/M = 0.4$ and $l = 1$, $(M\mu)_c = 0.405$]. We note that, in this case, since $M\mu = 0.4$, the low-frequency approximation A/v, although still valid for the partial cross section $\sigma_{l=0}$, is not a good approximation for the total low-frequency absorption cross section, as the condition $M\mu \ll 1$ is not fully satisfied and $\sigma_{l=1}$ also diverges in this limit.

In Fig. 2.13 we plot the transmission and reflection coefficients for $M\mu = 0.04$ and $M\mu = 0.4$ ($Q/M = 0.4$). We observe that in the case with smaller mass coupling ($M\mu = 0.04$) the transmission coefficient starts at zero and then goes to unity as ω increases, for all values of l. In the case with mass coupling $M\mu = 0.4$, the transmission coefficient for $l = 0$ is close to the unity for all frequencies. This may be understood by noting that $M\mu > M\mu_c$ in this case, and so there is no effective potential barrier for unbound modes; hence near-total absorption is to be expected.

In Fig. 2.14 we show the transmission and reflection coefficients for the monopole ($l = 0$) for a selection of values of the mass coupling. We can see that for $M\mu = 0.04$ the transmission coefficient starts near zero, but, as we choose larger values of the mass coupling, the value at $\omega = \mu$ ($v = 0$) increases. Beyond the critical mass $M\mu > M\mu_c = 0.193$ the value at $\omega = \mu$ is very close to unity.

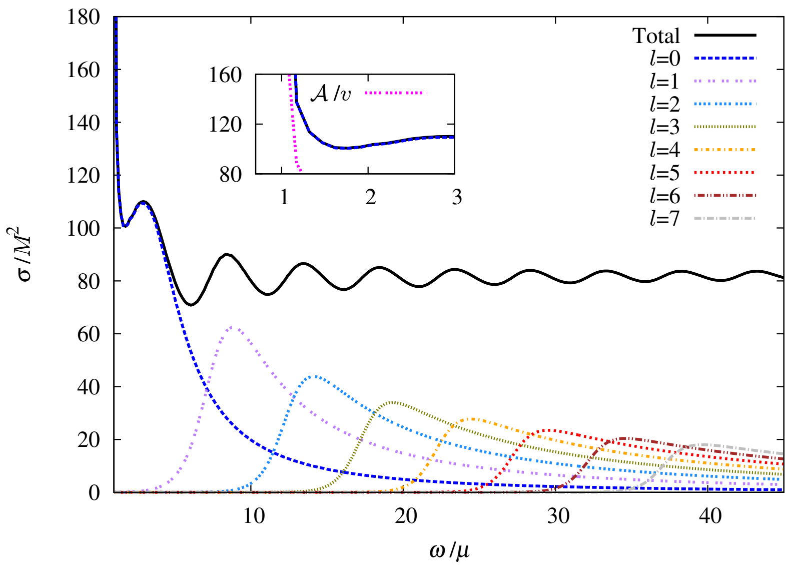

Figure 2.11: Total and partial absorption cross sections for $Q/M = 0.4$ and $M\mu = 0.04$. The inset shows the low-frequency limit of the absorption cross section.

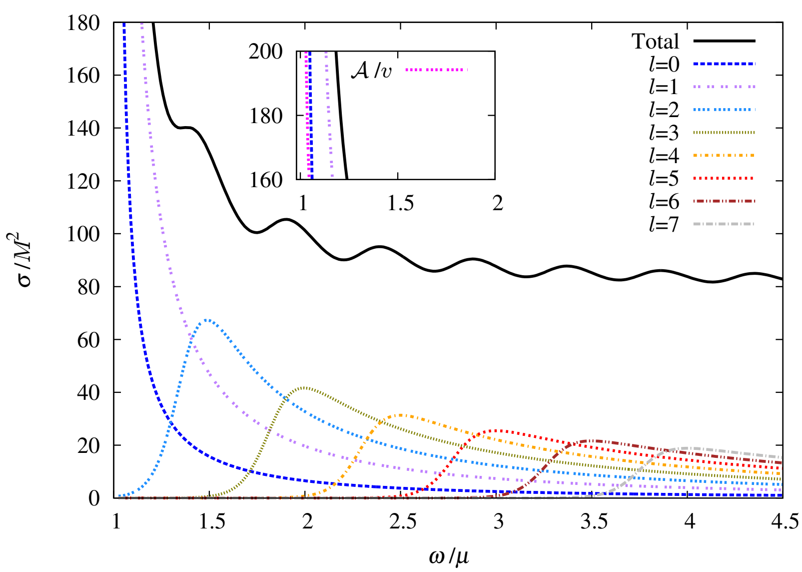

Figure 2.12: Total and partial absorption cross sections for $Q/M = 0.4$ and $M\mu = 0.4$. The inset shows the low-frequency limit of the absorption cross section.

2.6 Discussion

We have computed the absorption cross section of a massive chargeless scalar field by a Reissner-Nordström black hole for a range of frequencies. We compared our results

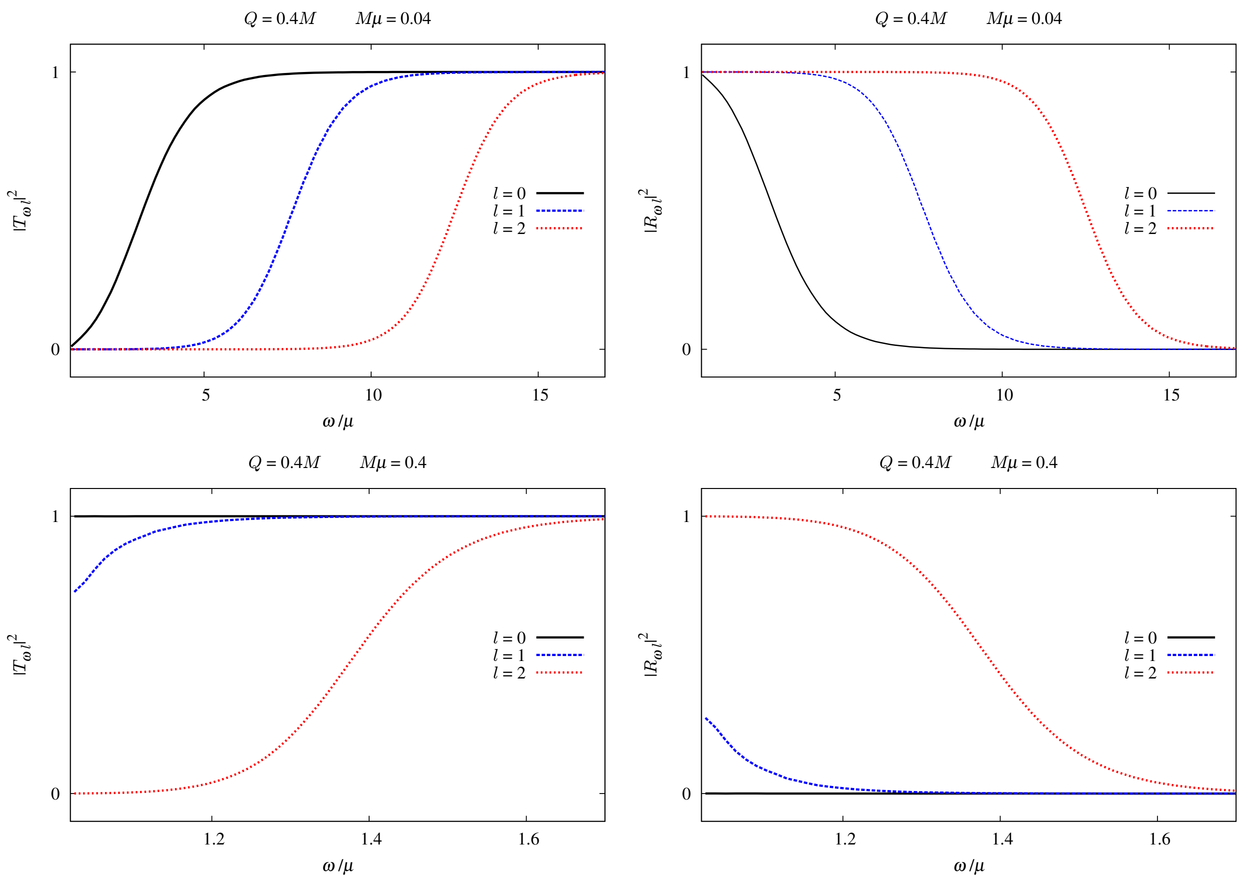

Figure 2.13: Transmission (left plots) and reflection (right plots) coefficients for $Q/M = 0.4$ and for mass couplings $M\mu = 0.04$ (top plots) and $M\mu = 0.4$ (bottom plots), for $l = 0$, 1 and 2.

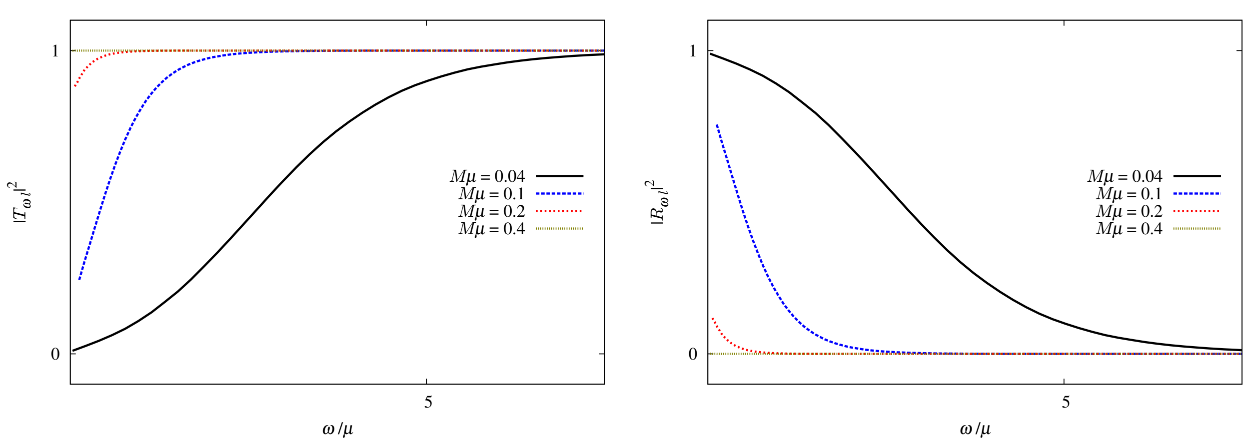

Figure 2.14: Transmission (left) and reflection (right) coefficients for $Q/M = 0.4$ and $l = 0$, for different choices of $M\mu$.

against (semi-)analytic approximations derived in the high- and low-frequency regimes.

In the moderate-to-high frequency regime, we have verified that the total absorption cross section oscillates around the geodesic capture cross section, as quantitatively described in Sec. 2.3. We have shown that the regular oscillations in the cross section (as a function of frequency) are encapsulated by the 'sinc' approximation [Eq. (2.37)], which we derived via the complex angular momentum formalism. Following Refs. [77, 78], we showed that the properties of the oscillations in the cross section (i.e. their frequency and amplitude) are set by the frequency and Lyapunov exponent of the unstable orbit in the spacetime at $r = r_c$.

For $M\mu \lesssim M\mu_c$ [20], we found that absorption in the monopole exhibits a local minimum (Fig. 2.9), whereas for $M\mu \gtrsim M\mu_c$ the absorption by the monopole increases monotonically as $v \to 0$. The critical mass $M\mu_c$ increases somewhat with charge-to-mass ratio Q/M, as shown in Fig. 2.2. For $M\mu > M\mu_c(l)$, the mode l is essentially entirely absorbed by the black hole. Hence, if $M\mu > M\mu_c(l = 0)$ then, by Eq. (2.21), the cross section will diverge as v^{-2} (rather than v^{-1}) in the limit $v \to 0$.

We have also found analytical solutions for the low-frequency limit, showing that the absorption cross section can go to different values depending on the velocity of the field. Recently a new dark matter candidate has been proposed by Hui *et al.* [85], in the form of a scalar field with mass $m \approx 10^{-22}\,\mathrm{eV}/c^2$ and de Broglie wavelength $\lambda_B \approx 1\,\mathrm{kpc}$. Its corresponding velocity is $v \approx 4 \times 10^{-4}$, found from $v = (1 + \lambda_B^2/\lambda_C^2)^{-1/2}$, where $\lambda_C = h/mc \approx 0.4\,\mathrm{pc}$ is the Compton wavelength. For a black hole mass $M_1 = 3.6 \times 10^6 M_\odot$ (e.g. Sgr. A* [86]), we find $v_c \approx 1.7 \times 10^{-5}$ and thus $v > v_c$; whereas for a supermassive black hole of mass $M_2 = 2 \times 10^8 M_\odot$ (e.g. Andromeda's supermassive black hole has mass $(1.1 - 2.3) \times 10^8 M_\odot$ [87]) we find $v_c = 9.4 \times 10^{-4}$ and thus $v < v_c$. This suggests that both regimes of Eq. (2.65) are potentially relevant in the scenario of Hui *et al.*, and that disparate cross sections are possible. For example, $\sigma_{lf}^{(1)} \approx 3.6 \times 10^{24}\mathrm{m}^2$ for M_1 (Sgr. A*) and $\sigma_{lf}^{(2)} \approx 2.6 \times 10^{28}\mathrm{m}^2$ for M_2 (Andromeda).

In the scenario explored here, the black hole's charge has a rather passive influence on the (uncharged) field, via the influence of charge on the spacetime geometry. We have found that, in general, the effect of black hole charge is to shift key features of the absorption profile of the Schwarzschild black hole. Let us briefly compare a charged black hole with an uncharged black hole of identical mass. The former appears 'smaller' than the latter, in several regards, as the former (i) has a smaller horizon area, (ii) has a smaller critical impact parameter b_c, (iii) casts a smaller shadow when illuminated by background radiation, (iv) possesses an unstable circular orbit with a smaller radius (and higher orbital frequency), and (v) exhibits (in general) a smaller scalar-wave absorption cross section, than the latter. These points are interrelated. The critical impact parameter b_c determines the size of the shadow [(ii)] and also the absorption cross section in the high-frequency regime. Via Eq. (2.37), the impact parameter determines the wavelength of the oscillations-with-frequency seen in (e.g.) Figs. 2.6–2.8. The amplitude and decay of these oscillations are set by the critical impact parameter [Eq. (2.24)] and the Lyapunov exponent of the unstable circular orbit [Eq. (2.35)], whose dependence on Q/M and v is subtle (see Fig. 2.3).

The field mass creates qualitatively new effects, leading to (e.g.) a divergence in the cross section as $v \to 0$, and total absorption in low multipoles $l + 1/2 \lesssim \gamma M \mu$, where the numerical coefficient γ may be inferred from Fig. 2.2. For any known massive Standard Model fields on a solar-mass black hole spacetime, $M\mu \gg 1$; in such cases, the horizon scale is many orders of magnitude larger than the Compton wavelength of the massive field. However, this is not necessarily true for primordial black holes, or for (posited) ultralight particles such as the axion. To get (e.g.) $M\mu \sim 10^{-2}$, one may have $M \sim 10^8\,\text{kg}$ in the case of the Higgs boson; $M \sim 10^{11}\,\text{kg}$ in the case of the neutral pion; or (e.g.) $M \sim 2 \times 10^{30}\,\text{kg}$ for a (posited) axion of mass $\mu \sim 10^{-12}\,\text{eV}$.

Chapter 3

Absorption of a massive and charged scalar field by charged static black holes

In this chapter we compute the absorption cross section for a charged and massive scalar field in a Reissner-Nordström background for the full range of frequencies, using a numerical approach. We compare our numerical results with the low- and high-frequency limits, which we obtain analytically. We also analyse the superradiant scattering implications in the partial and total absorption cross sections.

3.1 The field equations

The Klein-Gordon equation for a charged and massive scalar field in this geometry can be written as

$$(\nabla_\nu - iqA_\nu)(\nabla^\nu - iqA^\nu)\Phi = \mu^2\Phi, \tag{3.1}$$

where μ and q are the mass and charge of the scalar field, respectively, and $A^\nu = (Q/r, 0, 0, 0)$ is the vector potential of the background electromagnetic field. We can solve Eq. (3.1) by making a separation of variables, such as

$$\Phi_{\omega l} = \frac{\psi_{\omega l}(r)}{r} P_l(\cos\theta) e^{-i\omega t}, \tag{3.2}$$

where $\psi_{\omega l}(r)$ satisfies the radial equation

$$f\frac{d}{dr}\left(f\frac{d}{dr}\psi_{\omega l}\right)+V_{\mathit{eff}}(r)\psi_{\omega l}=0, \tag{3.3}$$

with the effective potential

$$V_{\mathit{eff}}(r)=\left[\left(\omega-\frac{qQ}{r}\right)^2-f\left(\mu^2+\frac{l(l+1)}{r^2}+\frac{f'}{r}\right)\right]. \tag{3.4}$$

Since we are interested in absorption and scattering properties, we assume that the scalar field is unbounded, so that $\omega > \mu$.

We can use the tortoise coordinate r_*, defined by $dr_*/dr = f^{-1}$, in Eq. (3.3) and obtain a Schrödinger-like equation, namely

$$\frac{d^2}{dr_*^2}\psi_{\omega l}+V_{\mathit{eff}}(r)\psi_{\omega l}=0. \tag{3.5}$$

Taking the asymptotic limits of Eq. (3.5) we find the solutions

$$\psi_{\omega l}(r)\approx\begin{cases} T_{\omega l}\, e^{-i\xi r_*}, & \text{for } r\to r_+, \\ e^{-i\rho r_*}+R_{\omega l}e^{i\rho r_*}, & \text{for } r\to\infty, \end{cases} \tag{3.6}$$

where $\xi \equiv \omega - qQ/r_+$ and $\rho \equiv \sqrt{\omega^2-\mu^2}$. $T_{\omega l}$ and $R_{\omega l}$ are associated to the transmitted and reflected parts of the wave. By imposing the conservation of the flux, we find the relation

$$|R_{\omega l}|^2+\frac{\xi}{\rho}|T_{\omega l}|^2=1, \tag{3.7}$$

where $|R_{\omega l}|^2$ is the reflection coefficient and $|T_{\omega l}|^2$ is the trasmission coefficient.

When $qQ < 0$, $\xi > 0$ and we have an incoming wave at the horizon, implying that there is no superradiance for this case. On the other hand, when $qQ > 0$ and $\omega < |qQ|/r_+$ we have $\xi < 0$. In this case, the sign of the exponential $e^{-i\xi r_*}$ is switched and instead of an incoming wave at the horizon we have an outgoing wave. This implies in a superradiant scattering, since this outgoing wave at the horizon will reinforce the outgoing wave at infinity.

The absorption cross section is given by

$$\sigma=\sum_{l=0}^{\infty}\sigma_l, \tag{3.8}$$

where the partial absorption cross section σ_l is given by

$$\begin{aligned}\sigma_l &= \frac{\pi}{\rho^2}(2l+1)(1-|R_{\omega l}|^2)\\ &= \pi\frac{\xi}{\rho^3}(2l+1)|T_{\omega l}|^2.\end{aligned} \tag{3.9}$$

3.2 Analytical results

3.2.1 Low-frequency limit

In this subsection we compute the absorption cross section in the limit $\omega \ll 1$. In order to find an analytical solution we also assume $\mu \ll 1$ and $qQ/r_+ \ll 1$. We follow the same method used by Unruh in Ref. [21], which consists in making a separation of the parameter space in three different regions, namely:

- Region I, very close to the black hole event horizon, i.e., $r \to r_+$;
- Region II, low-frequency limit, where ω, μ and qQ/r_+ are much smaller than 1;
- Region III, far away from the black hole event horizon, i.e., $r \gg r_+$.

We find similar equations to the ones obtained in Sec. 2.4 for each region, which are

$$\varphi_{\omega l}(r) \approx \begin{cases} A^{tra}e^{-i\xi r_*}, & \text{for Region I,}\\ \zeta \ln\left(\frac{r-r_+}{r-r_-}\right) + \tau, & \text{for Region II,}\\ a\frac{F_l(\bar\eta,\omega v r)}{r} + b\frac{G_l(\bar\eta,\omega v r)}{r}, & \text{for Region III,}\end{cases} \tag{3.10}$$

where $\varphi_{\omega l} \equiv \psi_{\omega l}/r$; $F_l(\bar\eta, \omega v r)$ and $G_l(\bar\eta, \omega v r)$ are the regular and irregular spherical wave functions, respectively; A^{tra}, ζ, τ, a and b are constants, and

$$\bar\eta = -\frac{M(\omega^2+\rho^2)}{\rho} + \frac{qQ}{2\rho}. \tag{3.11}$$

We then make an interpolation between the regions and find the low-frequency absorption cross section, given by

$$\sigma_{\rm lf} = \frac{\mathcal{A}}{\rho}\left(\omega - \frac{qQ}{r_+}\right), \tag{3.12}$$

where $\mathcal{A} = 4\pi r_+^2$ is the area of the black hole. We see that for $q = 0$, Eq. (3.12) gives us $\mathcal{A}/v$, where $v = \sqrt{1-\mu^2/\omega^2}$, which is the result obtained for the massive chargeless scalar field in a Reissner-Nordström background, as shown in Sec. 2.4 [62].

3.2.2 High-frequency limit

In the limit $\omega \gg \mu$ the field can be analyzed as a charged particle. Is this case the particle does not follow a geodesic, since it is subjected to the Lorentz force caused by the charged black hole. From Eq. (1.14), we write

$$\left(\frac{du}{d\phi}\right)^2 = -f(u)u^2 + (1-f(u))\frac{\mu^2}{L^2} + \frac{Q^2u^2q^2}{L^2} - \frac{2QqEu}{L^2} + \frac{E^2-\mu^2}{L^2}, \tag{3.13}$$

where $u \equiv 1/r$ and $f(u) = 1 - 2Mu + Q^2u^2$. E and L are the energy and the angular momentum of the particle, respectively, which, in the semiclassical limit can be associated to $E \to \omega$ and $L \to l + 1/2$, respectively.

The high-frequency absorption cross section is given by $\sigma_{\text{hf}} = \pi b_c^2$, where the critical impact parameter is given by $b_c = L_c/\sqrt{E_c^2 - \mu^2}$ and L_c and E_c are the critical angular momentum and critical energy, respectively. With Eq. (3.13) and its derivative we can find b_c and, consequently, the high-frequency absorption cross section. We have found a lengthy closed-form solution for the critical impact parameter b_c, which we will not exhibit here.

3.3 Numerical analysis

We can solve the radial equation (3.3) numerically, from very close to the black hole event horizon to very far away from it, using the asymptotical expressions, given by Eq. (3.6) and their derivatives. We can use the mass of the black hole as a normalization factor and fix the values of Q, q and μ. With the radial solution we are able to compute numerically the reflection coefficient and the absorption cross section.

Figure 3.1 shows the reflection coefficient for $M\mu = 0.4$, $Q/M = 0.8$, $l = 0$, and different choices of Mq. In this plot we exhibit only the part of the reflection coefficient that is greater than 1. We see that, as we increase the charge of the field, keeping its mass fixed, the maximum of the reflection coefficient grows and moves to the right, i. e., happens for bigger values of the frequency.

If we fix $Mq = 1.6$ and vary $M\mu$, as in Fig. 3.2, we see that for smaller values of $M\mu$ we have greater values of the reflection coefficient. We also notice a modification in the

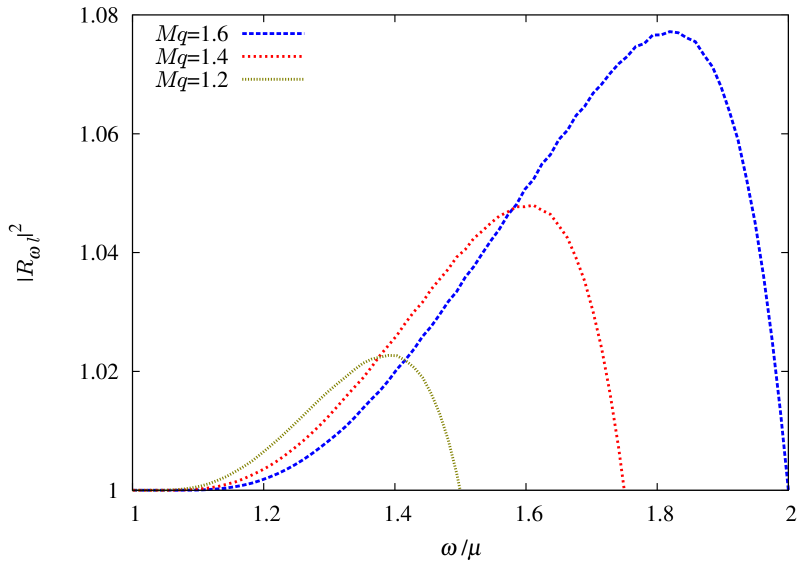

Figure 3.1: Reflection coefficient as a function of the frequency for $M\mu = 0.4$, $Q/M = 0.8$, $l = 0$, and different choices of Mq.

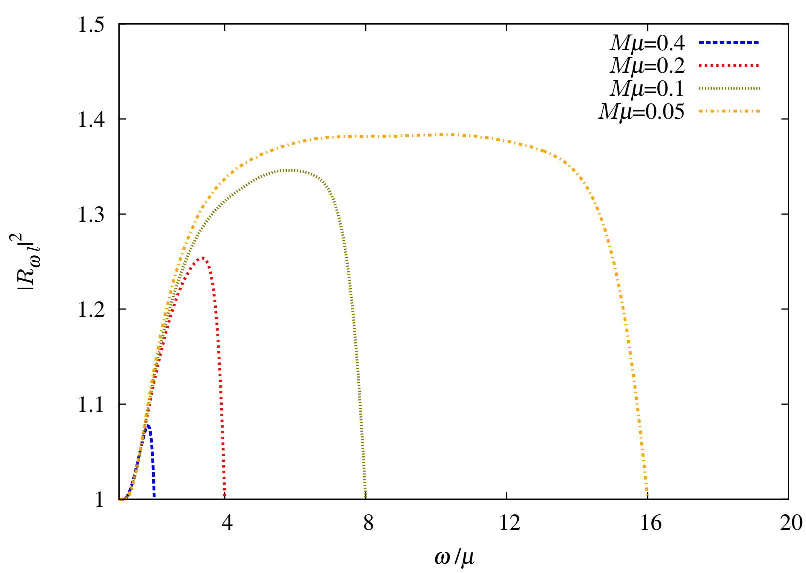

Figure 3.2: Reflection coefficient for $Q/M = 0.8$, $Mq = 1.6$, and different values of $M\mu$. As in Fig. 3.1, here we only exhibit the values of $|R_{\omega l}|^2$ which are greater than 1.

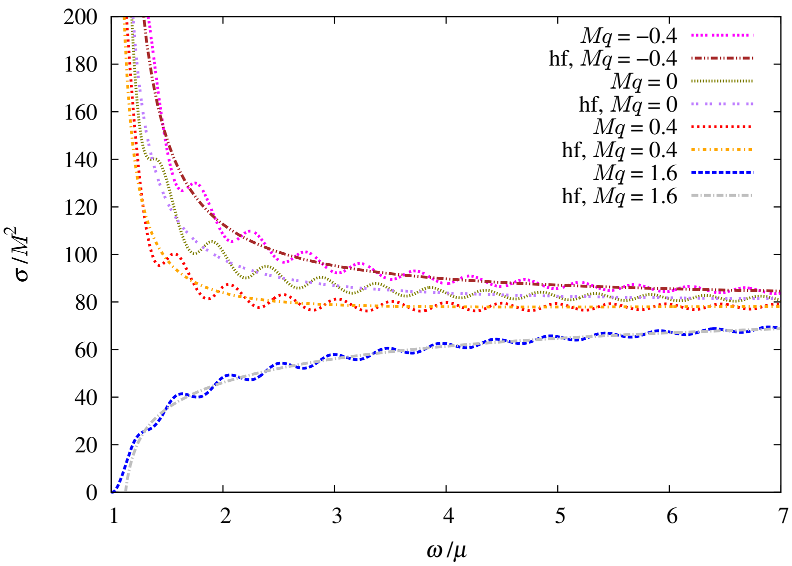

Figure 3.3: Total absorption cross section as a function of the frequency, for $M\mu = 0.4$, $Q/M = 0.4$, and different choices of Mq.

shape of the reflection coefficient as we vary the parameter $M\mu$.

In Fig. 3.3 we compare the high-frequency limit of the absorption cross section with the numerical results for a fixed black hole charge and different choices of the scalar field charge. We observe that (i) the numerical results oscillate around the analytical approximation, even for intermediate values of the frequency, and (ii) as we increase the charge of the field the absorption cross section decreases. We can also observe from Fig. 3.3 that, depending on the charge of the field, we can have a finite value for the absorption cross section in the limit $\omega/\mu \to 1$, contrasting with the chargeless massive field case, in which we always have a divergent absorption cross section in this limit.

Figure 3.4 presents the total absorption cross section for different choices of the mass coupling $M\mu$. We see that, for fixed values of Q/M and Mq, as we increase the mass coupling the total absorption cross section also increases.

In Fig. 3.5 we compare our numerical results for the $l = 0$ case with the low-frequency absorption cross section σ_{lf}, given by Eq. (3.12). We see that for very small mass couplings $M\mu$, σ_{lf} gives a good approximation for the absorption cross section, but as we increase the mass coupling, the approximation gets worse, once that the numerical results go to infinity faster than the analytical ones.

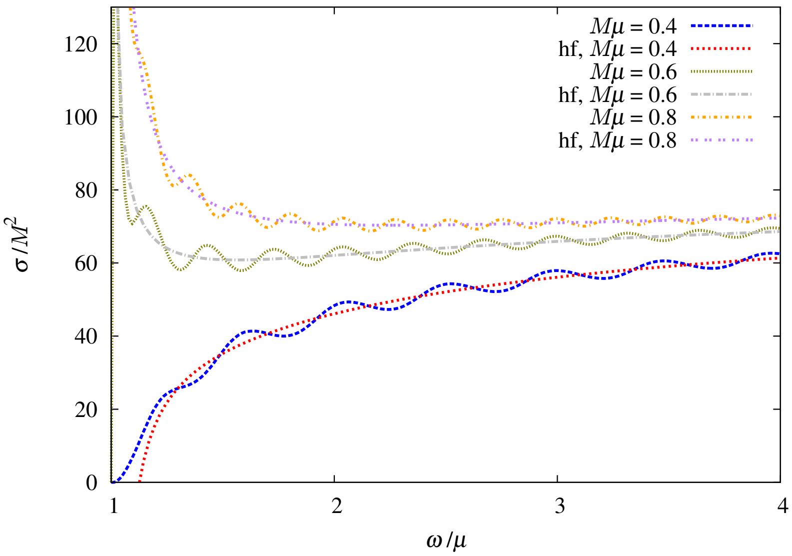

Figure 3.4: Total absorption cross section for $Q/M = 0.4$, $Mq = 1.6$, and different values of $M\mu$. As in Fig. 3.3, here we also exhibit the corresponding high-frequency result.

In Fig. 3.6 we show the partial and total absorption cross sections as function of the frequency for $M\mu = 0.4, Q/M = 0.4$, and $Mq = -0.4$. In this case $Qq < 0$, therefore we do not have superradiance. Moreover, in the low frequency limit the total absorption cross section goes to infinity.

In Fig. 3.7 we present the partial and total absorption cross sections for $M\mu = 0.4, Q/M = 0.8$, and $Mq = 1.6$. In the inset we can observe that for $1 < \omega/\mu \lesssim 2$ the total and partial absorption cross sections for $l = 0$ and $l = 1$ have negative values, implying that, in this case, we have superradiant scattering.

3.4 Discussion

We studied the Klein-Gordon equation for a charged and massive scalar field in a Reissner-Nordström background. We found the reflection coefficient and the absorption cross section, comparing numerical and approximate analytical results. Some of the features are similar to the chargeless scalar case, but the charge introduces new aspects.

We obtained that the total absorption cross section exhibits a wiggly pattern as a consequence of the individual contributions of the partial absorption cross sections, which

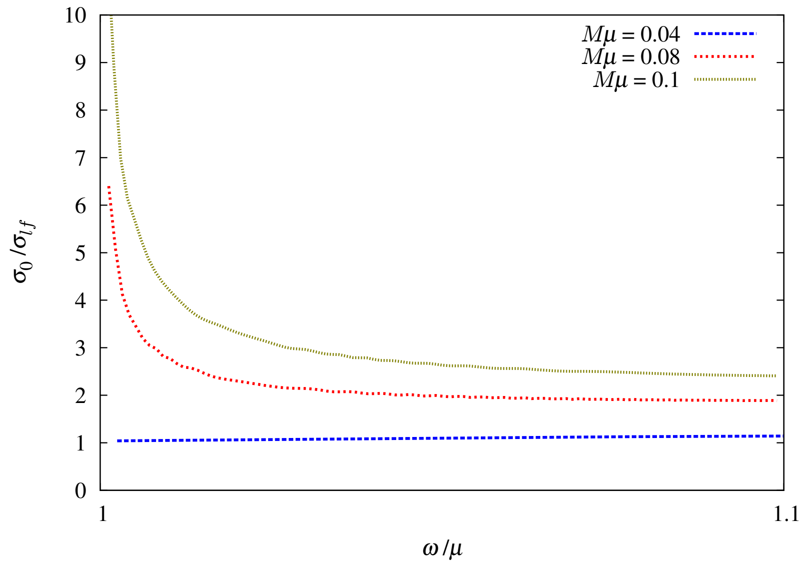

Figure 3.5: Comparison between the partial absorption cross section for $l = 0$ (σ_0) obtained numerically, and the low-frequency approximation ($\sigma_{\rm lf}$) for different choices of $M\mu$. We have chosen $Q/M = 0.4$, and $Mq = 0.1$

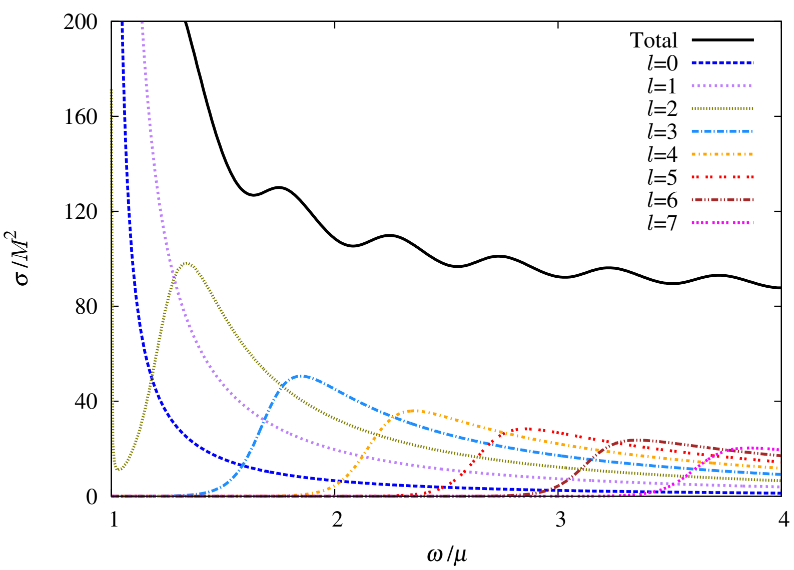

Figure 3.6: Partial and total absorption cross sections for $M\mu = 0.4$, $Q/M = 0.4$, and $Mq = -0.4$.

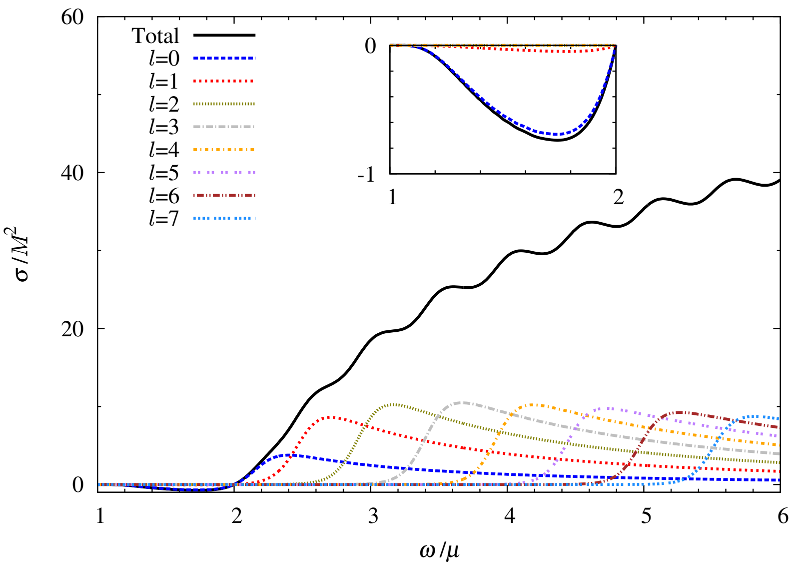

Figure 3.7: Partial and total absorption cross sections for $M\mu = 0.4$, $Q/M = 0.8$, and $Mq = 1.6$.

present maxima for different values of the frequency. Another interesting feature observed is that as we increase the charge coupling qQ, the absorption cross section gets smaller. This is due to the presence of a repulsive electromagnetic interaction (the Lorentz force) for $qQ > 0$ competing with the gravitational interaction, causing the decrease of the absorption.

If the charges of the field (q) and of the black hole (Q) have opposite signs, the absorption cross section is bigger than for the chargeless field case, due to the Lorentz attraction between the charges.

It is also worth emphasizing that for $Qq > 0$, in the limit $\omega \to \mu$, we can have finite values for the absorption cross section of the charged massive field; while for the case in which $q = 0$ the total absorption cross section always tends to infinity in this limit. Therefore the Lorentz repulsion force can render finite the low-frequency limit of the absorption cross section.

Concerning the analytical results, for the high-frequency limit we have been able to find the geometric optics limit of the absorption cross section and the numerical results oscillate around this limit. A similar behaviour is observed in the absorption of the chargeless massive scalar field by a Reissner-Nordström black hole. For the low-frequency limit we found an analytical approximation for the absorption cross section in the case when $M\mu$ and Qq/r_+ are very small. The result we found can be regarded as a generalization of the one obtained for the chargeless massive scalar field [62].

We have shown that we can have superradiance of a charged and massive scalar field in a Reissner-Nordström background and that this superradiance increases with the increase of Qq and with the decrease of $M\mu$. As we have seen, both the partial and the total absorption cross section can be negative. Partial waves are associated to spherical waves which, when appropriately summed, give rise to a planar wave. Our results show that planar scalar waves can be superradiantly amplified by black holes. This contrasts with the case of the rotating Kerr black hole [27], for which we also have negative partial scalar absorption cross sections, but they combine in a way that the total scalar absorption cross section is always positive. Even for the acoustic black hole analogue system with rotation, namely the draining bathtub, superradiance is not enough to imply in a negative total absorption cross section [88].

We can understand this difference between the uncharged rotating and charged black hole cases by realizing that for the rotating case we have, for the total scalar absorption cross section, besides the sum in l, a sum in m. Consequently, when the partial contributions of m are added, a positive sum is always obtained, resulting that planar scalar waves impinging in a Kerr black hole never present negative total absorption cross section.

Superradiant amplification of planar waves has also been reported for optical systems, related to electromagnetic scattering in active media [89–91].

Chapter 4

Absorption of a massless and chargeless scalar field by Kerr-Newman black holes

We compute numerically the absorption cross section of planar massless scalar waves impinging upon a Kerr-Newman black hole with different incidence angles. We investigate the influence of the black hole electric charge and angular momentum in the absorption spectrum, comparing our numerical computations with analytical results for the limits of high and low frequency.

4.1 Field equations

A scalar field $\Phi(x^\mu)$ is governed by the Klein-Gordon equation, which in a curved spacetime can be written in its covariant form as

$$\frac{1}{\sqrt{-g}}\partial_\mu\left(\sqrt{-g}g^{\mu\nu}\partial_\nu\Phi\right) = 0, \tag{4.1}$$

where $g_{\mu\nu}$ are the covariant components of the Kerr-Newman metric, which can be obtained directly from Eq. (1.28). $g^{\mu\nu}$ are the contravariant components of the metric and g is the metric determinant.

We can decompose the scalar field in wavelike solutions of Eq. (4.1), as follows:

$$\Psi = \sum_{l=0}^{+\infty} \sum_{m=-l}^{+l} \frac{U_{\omega lm}(r)}{\sqrt{r^2+a^2}} S_{\omega lm}(\theta) e^{im\phi - i\omega t}. \tag{4.2}$$

The functions $S_{\omega lm}$, appearing in Eq. (4.2), are the standard oblate spheroidal harmonics [92], which satisfy the following equation

$$\left(\frac{d^2}{d\theta^2} + \cot\theta \frac{d}{d\theta}\right) S_{\omega lm} + \left(\lambda_{lm} + a^2\omega^2\cos^2\theta - \frac{m^2}{\sin^2\theta}\right) S_{\omega lm} = 0, \tag{4.3}$$

where λ_{lm} are the eigenvalues of the spheroidal harmonics. These angular functions are normalized as follows:

$$\int d\theta \, \sin\theta \, |S_{\omega lm}(\theta)|^2 = \frac{1}{2\pi}. \tag{4.4}$$

Through the definition of the tortoise coordinate $r_\star$ in the Kerr-Newman spacetime, namely,

$$r_* \equiv \int dr \left(\frac{r^2+a^2}{\Delta}\right), \tag{4.5}$$

the differential equation obeyed by the radial function $U_{\omega lm}$ can be rewritten as

$$\left(\frac{d^2}{dr_*^2} + V_{\omega lm}\right) U_{\omega lm}(r_*) = 0, \tag{4.6}$$

with $V_{\omega lm}$ given by

$$\begin{aligned} V_{\omega lm}(r) &= \left(\omega - m\frac{a}{r_+^2+a^2}\right)^2 \\ &+ \left[2Mr - 2r^2 - \Delta + \frac{3r^2}{r^2+a^2}\Delta\right]\frac{\Delta}{(r^2+a^2)^3} \\ &- \left(a^2\omega^2 + \lambda_{lm} - 2ma\omega\right)\frac{\Delta}{(r^2+a^2)^2}. \end{aligned} \tag{4.7}$$

In Fig. 4.1 we plot the function $-M^2 V_{\omega lm}$ for different values of the rotation parameter (left panel) and BH charge (right panel), fixing $\omega = 0.1$ and $l = m = 1$ in both cases. We note that the larger are the BH rotation and charge, the larger is $-M^2 V_{\omega lm}$. Moreover, $-M^2 V_{\omega lm}$ presents a maximum and then goes to $-M^2\omega^2$ at infinity.

The radial equation (4.6) has a set of independent solutions usually labelled as *in, up, out* and *down*. The *in* modes are the appropriate ones to study absorption and scattering

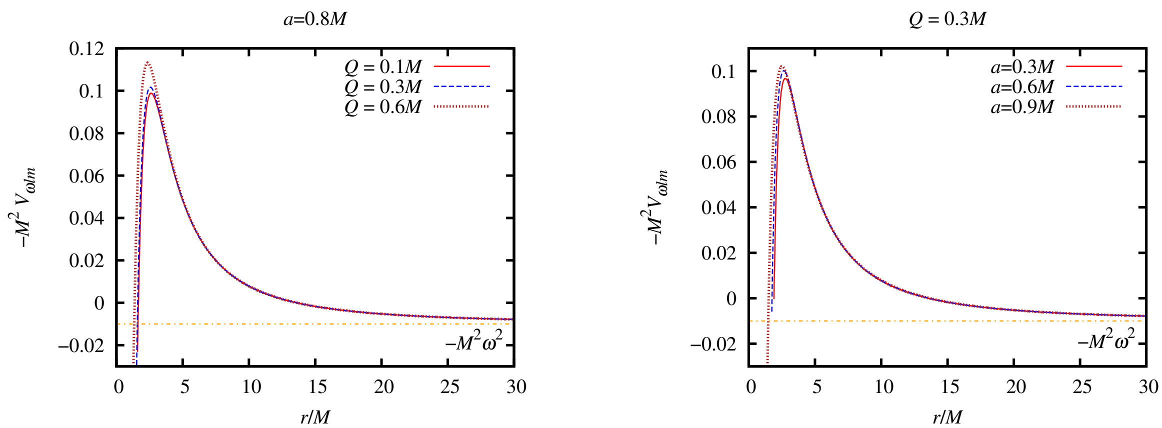

Figure 4.1: LEFT: The function $-M^2V_{\omega lm}$ is plotted for $Q/M = 0.4$ and different values of a. RIGHT: We plot $-M^2V_{\omega lm}$ as function of r for a fixed value of the BH angular momentum, $a = 0.8M$, and different values for the BH charge, Q. For both cases we choose $M\omega = 0.1$ and $l = m = 1$.

processes, since they denote purely incoming waves from the past null infinity. These modes have the following asymptotic behavior

$$U_{\omega lm}(r_*) \sim \begin{cases} \mathcal{I}_{\omega lm}e^{-i\omega r_*} + \mathcal{R}_{\omega lm}e^{i\omega r_*} & (r_*/M \to \infty), \\ \mathcal{T}_{\omega lm}e^{-i(\omega - m\Omega_{\rm H})r_*} & (r_*/M \to -\infty), \end{cases} \tag{4.8}$$

in which $\Omega_{\rm H} \equiv \frac{a}{r_+^2+a^2}$ is the event horizon angular velocity. The coefficients $\mathcal{R}_{\omega lm}$ and $\mathcal{T}_{\omega lm}$ are related to the reflection and transmission coefficients, respectively, and obey the equation

$$\left|\frac{\mathcal{R}_{\omega lm}}{\mathcal{I}_{\omega lm}}\right|^2 = 1 - \frac{\omega - m\Omega_{\rm H}}{\omega}\left|\frac{\mathcal{T}_{\omega lm}}{\mathcal{I}_{\omega lm}}\right|^2. \tag{4.9}$$

From this relation one can see that for $0 < \omega < m\Omega_{\rm H}$, $|\mathcal{R}_{\omega lm}|^2 > |\mathcal{I}_{\omega lm}|^2$. This enhancement in the amplitude of the reflected wave is known as superradiance [40].

4.2 Absorption cross section

The absorption cross section can be well described by analytical approximate results in the low- and high-frequency regimes. In the low-frequency regime, it was shown that the absorption cross section of massless scalar waves for stationary BHs, such as a Kerr-Newman BH, is given by the area of the event horizon. In the high-frequency limit, the absorption cross section tends to the capture cross section of null geodesics. These limiting results are important to check the accuracy of our numerical results, which are exhibited in Sec. 4.3. We anticipate that our numerical results, both in the low- and high-frequency regimes present great agreement with the analytical limits.

We can obtain an expression for the absorption cross section through the partial-wave approach, so that the total absorption cross section of massless and chargeless scalar waves impinging upon a Kerr-Newman BH with an incidence angle γ, is

$$\sigma = \sum_{l=0}^{\infty} \sum_{m=-l}^{l} \frac{4\pi^2}{\omega^2} \left| S_{\omega lm}(\gamma) \right|^2 \left(1 - \left| \frac{\mathcal{R}_{\omega lm}}{\mathcal{I}_{\omega lm}} \right|^2 \right). \tag{4.10}$$

According to the value assumed by the azimuthal number m, we can distinguish the modes between corotating ($m > 0$) and counterrotating ($m < 0$) with the BH. Hence, the total absorption cross section can be seen as a sum of the corotating

$$\sigma^{co} = \sum_{l=0}^{\infty} \sum_{m=1}^{l} \frac{4\pi^2}{\omega^2} \left| S_{\omega l(+m)}(\gamma) \right|^2 \left(1 - \left| \frac{\mathcal{R}_{\omega l(+m)}}{\mathcal{I}_{\omega l(+m)}} \right|^2 \right), \tag{4.11}$$

and the counterrotating contributions [1]

$$\begin{aligned} \sigma^{counter} &= \sum_{l=0}^{\infty} \frac{4\pi^2}{\omega^2} \left| S_{\omega l0}(\gamma) \right|^2 \left(1 - \left| \frac{\mathcal{R}_{\omega l0}}{\mathcal{I}_{\omega l0}} \right|^2 \right) \\ &+ \sum_{l=0}^{\infty} \sum_{m=1}^{l} \frac{4\pi^2}{\omega^2} \left| S_{\omega l(-m)}(\gamma) \right|^2 \left(1 - \left| \frac{\mathcal{R}_{\omega l(-m)}}{\mathcal{I}_{\omega l(-m)}} \right|^2 \right), \end{aligned} \tag{4.12}$$

where we split the absorption cross section into superradiant modes (σ^{co}) and non-superradiant ones ($\sigma^{counter}$).

4.2.1 Capture cross section

In the high-frequency regime the absorption cross section approaches the capture cross section of null geodesics, which is given by [27]

$$\sigma_{\rm hf} = \frac{1}{2} \int_{-\pi}^{\pi} b_c^2(\chi, \gamma) d\chi, \tag{4.13}$$

[1] Note that the $m = 0$ mode is included among the counterrotating modes.

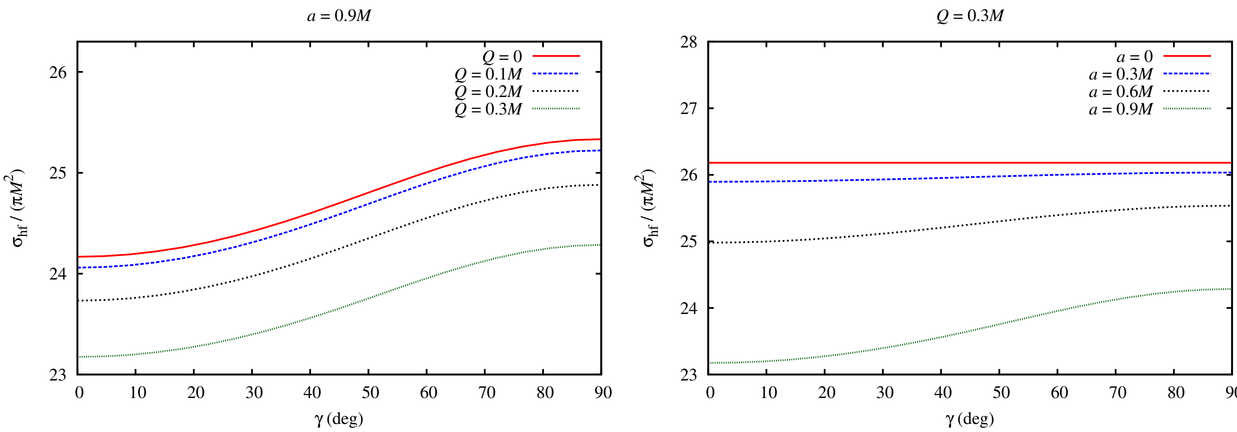

Figure 4.2: LEFT: The capture cross section for a fixed value of the rotation parameter ($a = 0.9M$) and different values of the charge-to-mass ratio ($Q/M = 0$, 0.1, 0.2, and 0.3). RIGHT: The capture cross section for a fixed value of the BH charge ($Q = 0.3M$) and different values of the BH rotation ($a/M = 0$, 0.3, 0.6, and 0.9).

where $b_c(\chi, \gamma)$ is the critical impact parameter and χ is an angle defined in the plane of the impinging wave, as shown in Fig. 1.1. In the case when b_c is constant we recover $\sigma_{\text{hf}} = \pi b_c^2$, which is the high-frequency absorption cross section for static geometries. We find the critical impact parameter by solving the equations for $R(r_c) = 0$ and $R'(r_c) = 0$, where $R(r)$ is given by Eq. (1.39).

The capture cross section is exhibited in Fig. 4.2 as a function of the null geodesic angle of incidence. We consider different values for the BH rotation parameter (right panel) and electric charge (left panel), showing that the capture cross section diminishes as we increase the values of the Kerr-Newman BH spin and charge-to-mass ratio. For the static case ($a = 0$) the capture cross section is independent of the incidence angle, but for $a > 0$ the capture cross section increases as we increase γ, reaching its maximum value at the equatorial plane ($\gamma = 90\ deg$).

4.3 Results

Along this section, we exhibit an assortment of our numerical results for the massless and chargeless scalar absorption cross section of the Kerr-Newman BH.

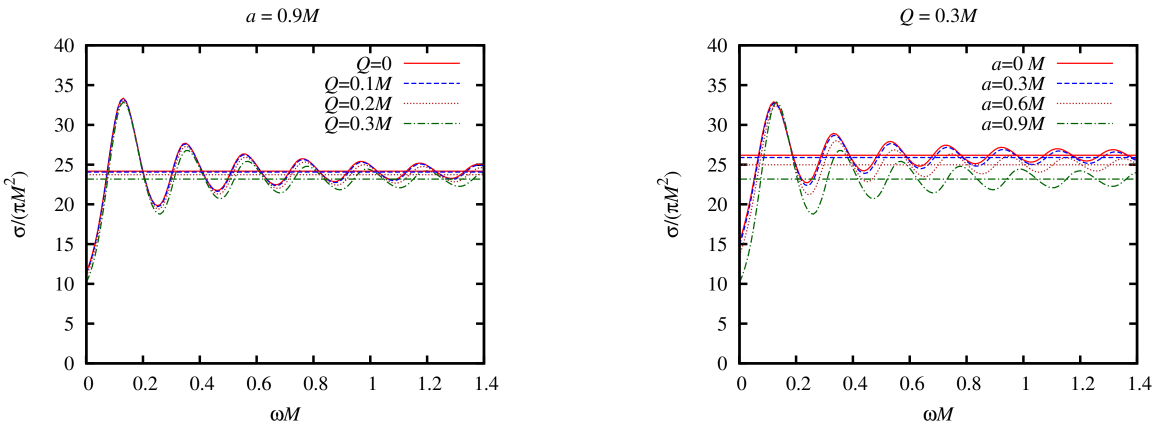

Figure 4.3: LEFT: The total absorption cross section for a fixed BH rotation, $a = 0.9M$, with $Q/M = 0$, 0.1, 0.2, and 0.3. RIGHT: The total absorption cross section for a black hole charge $Q = 0.3M$ and different rotation parameters $a/M = 0$, 0.3, 0.6, and 0.9. Both left and right panels were obtained for on-axis incidences ($\gamma = 0$), and the horizontal lines are the capture cross section of null geodesics in each case.

In Fig. 4.3 we show the total absorption cross section in the on-axis case ($\gamma = 0$) for a fixed rotation parameter (left panel) and for a fixed black hole charge (right panel). In the on-axis case we note that the absorption cross section presents a similar behavior to the static black hole case, i.e., the total absorption cross section starts from a value given by its event horizon area and then oscillates with a decreasing amplitude around its high frequency-limit, which is represented by horizontal lines, approaching this value for larger values of ω. Furthermore, we can see that the larger is the black hole charge and the faster is its spin, the smaller is the total absorption cross section. This behavior is also observed for the capture cross section of null geodesics (see Fig. 4.2).

For off-axis incident waves the oscillating pattern of the absorption cross section is less regular than that of the on-axis case. In order to illustrate this, in Fig. 4.4 we consider incidences along the equatorial plane $\gamma = 90\,deg$. In the left panel of Fig. 4.4, we choose Kerr-Newmann black holes with the same rotation parameter $a = 0.8M$, but with different charge-to-mass ratio $Q/M = 0.1,\, 0.3,\, \text{and}\, 0.6$. We also consider rotating and charged black holes with the same electric charge $Q = 0.3M$ (right panel) and different rotation parameters $a/M = 0.3,\, 0.6,\, \text{and}\, 0.9$. As a general behavior, we can observe, in

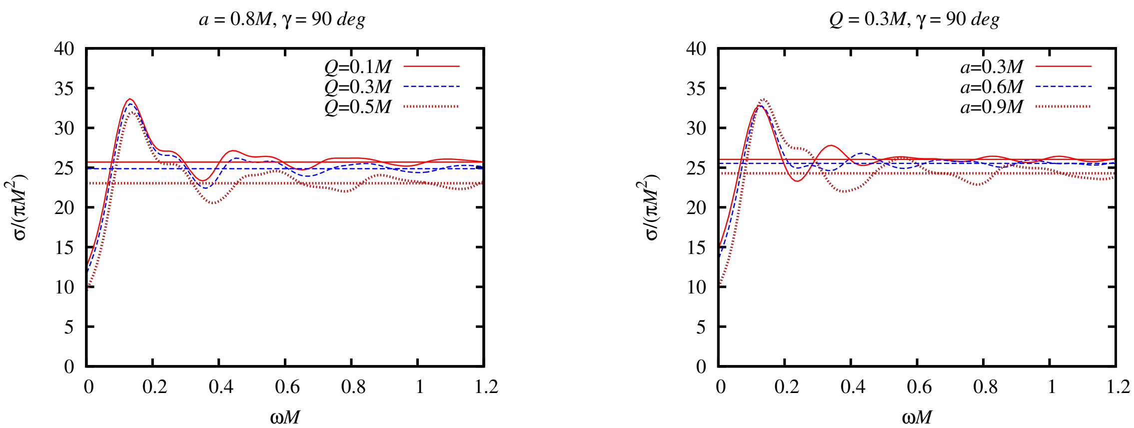

Figure 4.4: LEFT: The total absorption cross section for incidences along the equatorial plane ($\gamma = 90$ deg) for $a = 0.8M$ and $Q/M = 0.1$, 0.3, and 0.5. RIGHT: The total absorption cross section for $\gamma = 90$ deg, with $Q = 0.3M$ and different black hole rotations $a/M = 0.3$, 0.6, and 0.9.

both left and right panels of Fig. 4.4, that it is not possible to identify a regular pattern as in the case of on-axis incidences. As we increase the charge-to-mass ratio the absorption cross section decreases, but maintains its shape. On the other hand, as we increase a the absorption cross section becomes less regular.

In Fig. 4.5 we show the results for the corotating and couterrotating contributions to the total absorption cross section. By examining the corotating and counterrotating contributions to the absorption cross section separately, it is possible to identify a more regular behavior. Also, we see that the contributions of the counterrotating modes to the total absorption cross section are larger than the corotating ones. The corotating modes are more absorbed as either the BH charge or rotation parameter decreases. The counterrotating modes are more absorbed as the BH charge decreases and the behavior for different rotations depends on the frequency regime. In the low-frequency limit the absorption cross section for counterrotating waves decreases as we increase the rotation parameter. In this limit the absorption cross section is dominated by the waves with $m = 0$ and goes to the area of the black hole as $\omega \to 0$. In the high-frequency regime, $\sigma^{counter}$ increases as a increases.

In Fig. 4.6 we present the partial absorption cross sections for the dipole mode ($l = 1$).

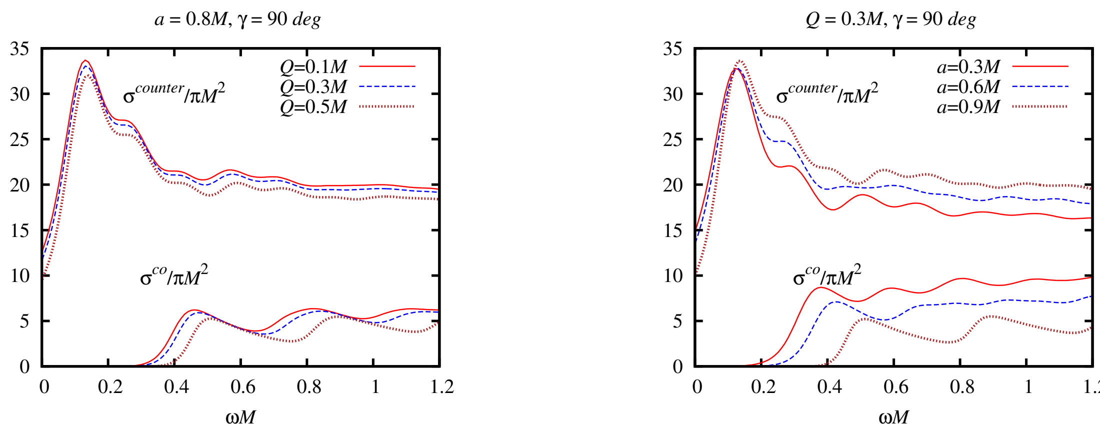

Figure 4.5: LEFT: The corotating (σ^{co}) and counterrotating ($\sigma^{counter}$) contributions to the absorption cross section for $a = 0.8M$, and $Q/M = 0.1$, 0.3, and 0.5. RIGHT: The corotating and counterrotating contributions to the absorption cross section for $Q = 0.3M$, and $a/M = 0.3$, 0.6, and 0.9.

When we increase the black hole charge (left panel), both the corotating ($m = 1$) and counterrotating ($m = -1$) partial cross sections decrease. On the other hand, when we increase the rotation parameter (right panel) the associated values of the corotating partial absorption cross section decrease, while the counterrotating ones increase.

In the Kerr-Newman spacetime, due to superradiance, reflected waves can be amplified, what results in a negative partial absorption cross section. We show the partial absorption cross sections, in Fig. 4.7, for the mode $l = m = 1$, considering incidence along the equatorial plane. For a fixed rotation parameter (left panel), the larger the black hole charge is, the smaller is superradiance. On the other hand, when we increase the rotation parameter (right panel), superradiance increases.

4.4 Discussion

We have obtained numerically the absorption spectrum of planar massless scalar waves for a Kerr-Newman black hole, considering different values for the black hole rotation parameter and electric charge. We have confirmed with our numerical results that in the low-frequency regime the absorption cross section tends to the area of the black hole

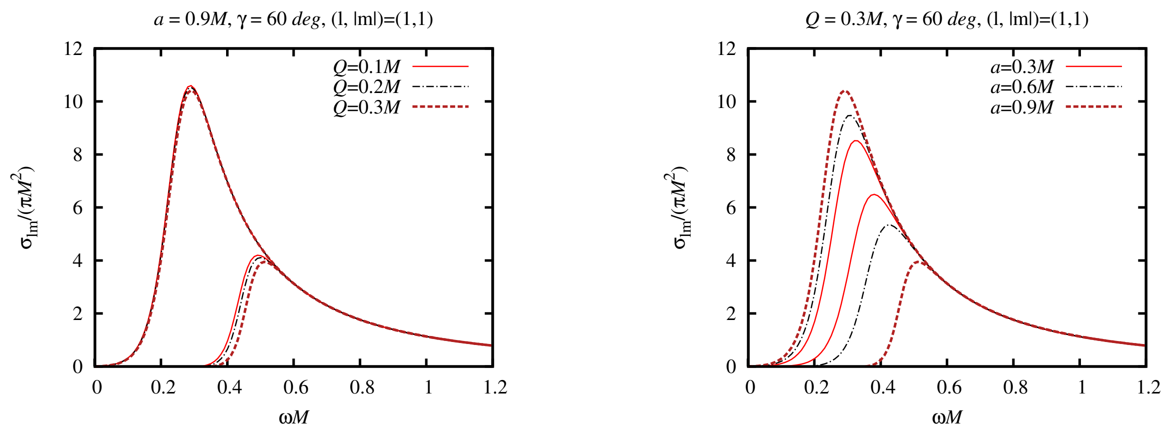

Figure 4.6: LEFT: Conterotating ($m = -1$) and corotating ($m = -1$) partial absorption cross sections for $\gamma = 60$ deg, $a = 0.9M$, and $Q/M = 0.1$, 0.2, and 0.3. RIGHT: Conterotating and corotating partial absorption cross sections for a fixed black hole charge ($Q = 0.3M$), and different rotation parameters $a/M = 0.3$, 0.6, and 0.9. Again, we consider $\gamma = 60$ deg. In both right and left panels, the curves associated to the higher peaks are related to the counterrotating modes while the low peaks are associated to corotating ones.

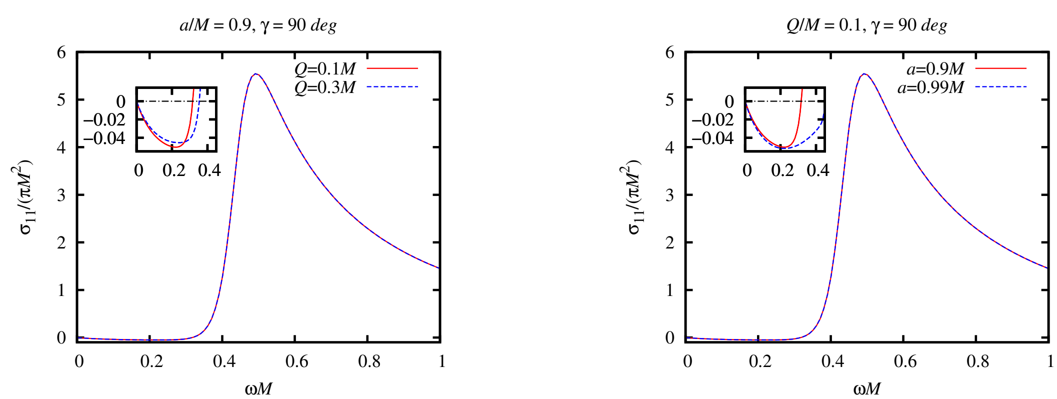

Figure 4.7: LEFT: The partial absorption cross section for the mode $l = m = 1$ with $a = 0.9M$ and $Q/M = 0.1$ and 0.3. RIGHT: The partial absorption cross section for the mode $l = m = 1$ with $Q/M = 0.1$ and $a/M = 0.9$ and 0.99. In both left and right panels, the insets help us to see more clearly the superradiance, which is very small for scalar waves.

horizon, while in the high-frequency regime it approaches the capture cross section of null geodesics.

We have shown that the absorption cross section presents a regular oscillatory behavior around its high-frequency limit when the waves impinge along the rotation axis ($\gamma = 0$). This oscillatory behavior comes from the contributions of waves with different angular momentum, l. As either the charge or the rotation parameter increases, the absorption cross section decreases, what is consistent with the fact that when we increase these parameters both the area and critical impact parameter of the black hole decrease.

For off-axis incidences ($\gamma \neq 0$) we have observed that, in the high-frequency regime, the absorption cross section behaves with less regular oscillations around the geometric capture cross section, what is a consequence of the different contributions given by the co- and counterrotating modes. We have also noted that, for off-axis incidences, the oscillatory pattern becomes more irregular for larger values of the black hole rotation parameter.

When we consider the corotating and counterrotating contributions to the absorption cross section separately, we identify a more regular absorption profile, and we observe that the counterrotating modes are more absorbed than the corotating ones. Moreover, we have obtained that the larger the black hole charge and rotation parameter are, the less absorbed are the corotating waves. For the counterrotating case we have obtained that the waves are more absorbed as the black hole charge decreases, and as we increase the rotation parameter we have different behaviors for different frequency regimes. This happens because in the low-frequency limit the field is dominated by the modes with $m = 0$, tending to the area of the black hole horizon, which decreases as we increase the black hole rotation. As we reach higher values of the frequency, due to the frame dragging effect, the absorption cross section increases for bigger values of the black hole rotation parameter.

We have also considered the case of superradiant scattering, finding that superradiance is larger, the faster the black hole spins and the smaller is the black hole charge. As for the Kerr case, superradiance yields a negative partial absorption cross section, although the total absorption cross section remains positive.

Chapter 5

Clouds around Kerr-Newman black holes

Massive complex scalar fields can form bound states around Kerr black holes. These bound states – dubbed *scalar clouds* – are generically non-zero and finite on and outside the horizon; they decay exponentially at spatial infinity, have a real frequency and are specified by a set of integer "quantum" numbers (n, ℓ, m). For a specific set of these numbers, the clouds are only possible along a 1-dimensional subset of the 2-dimensional parameter space of Kerr black holes, called an *existence line*. In this chapter we make a thorough investigation of the scalar clouds due to neutral (charged) scalar fields around Kerr(-Newman) black holes. We present the location of the existence lines for a variety of quantum numbers, their spatial representation and compare analytic approximation formulas available in the literature with our numerical results, exhibiting a sometimes remarkable agreement.

5.1 Field equations

The charged and massive scalar field obeys Eq. (3.1), where the background electromagnetic 4-potential is given by Eq. (1.32). In order to solve this equation we decompose the scalar field as $\Psi = \sum_{l,m} \Psi_{lm}$ and separate variables as $\Psi_{lm} = R_{lm}(r)S_{lm}(\theta)e^{im\phi}e^{-i\omega t}$ [93], where $S_{lm}(\theta)$ are the spheroidal harmonics, which obey

$$\frac{1}{\sin\theta}\frac{d}{d\theta}\left(\sin\theta\frac{dS_{lm}}{d\theta}\right)+\left(K_{lm}+a^2(\mu^2-\omega^2)-a^2(\mu^2-\omega^2)\cos\theta-\frac{m^2}{\sin^2\theta}\right)S_{lm}=0\ , \quad (5.1)$$

where K_{lm} are separation constants.

The radial functions $R_{lm}(r)$ obey the equation

$$\Delta\frac{d}{dr}\left(\Delta\frac{dR_{lm}}{dr}\right)+\left[H^2+(2ma\omega-K_{lm}-\mu^2(r^2+a^2))\Delta\right]R_{lm}=0, \quad (5.2)$$

where $H\equiv(r^2+a^2)\omega-am-qQr$. We can rewrite Eq. (5.2) using the tortoise coordinates, defined by

$$\frac{dr_*}{dr}\equiv\frac{r^2+a^2}{\Delta}\ , \quad (5.3)$$

and obtain a new radial equation without the first derivative term,

$$\frac{d^2U_{lm}}{dr_*^2}+\left\{\frac{[H^2+(2ma\omega-\mu^2(r^2+a^2)-\lambda_{ml})\Delta]}{(r^2+a^2)^2}\right.$$
$$\left.-\frac{\Delta(\Delta+2r(r-M))}{(r^2+a^2)^3}+\frac{3r^2\Delta^2}{(r^2+a^2)^4}\right\}U_{lm}=0\ , \quad (5.4)$$

in terms of the new functions U_{lm}, defined as

$$U_{lm}\equiv R_{lm}\sqrt{r^2+a^2}\ . \quad (5.5)$$

Next we must impose boundary conditions. Any state in a black hole background should have a purely ingoing boundary condition at the horizon; moreover the bound states we are looking for should have an asymptotically exponentially decaying behavior. Analyzing the radial equation (5.2) we find asymptotic solutions compatible with these requirements

$$R_{lm}(r)\approx\begin{cases} e^{-i(\omega-\omega_c)r_*}, & \text{for } r\to r_H,\\ \frac{e^{-\sqrt{\mu^2-\omega^2}r}}{r}, & \text{for } r\to\infty,\end{cases} \quad (5.6)$$

where we defined the critical frequency ω_c, given by

$$\omega_c\equiv m\Omega_H+q\Phi_H=\frac{ma}{r_H^2+a^2}+\frac{qQr_H}{r_H^2+a^2}\ . \quad (5.7)$$

In order to study bound states, in the following, we shall focus on the case for which the field's frequency equals the critical one, i.e

$$\omega=\omega_c\ . \quad (5.8)$$

Substituting this in the equations found in the previous chapter we are able to find bound solutions. We fix the parameters of the holes, apply the boundary conditions for each problem and find the solutions numerically. We used a shooting method to find the solutions using both a standard FORTRAN solver, as well as a MATHEMATICA routine, with agreement to high accuracy.

The radial equation (5.2) is solved for given cloud quantum numbers (n, l, m) and charge q. The field mass μ is taken as a normalization scale and all quantities will be referred with respect to it. Moreover, we fix the black hole background parameters r_H and Q. In this procedure, we consider the following expansion for the coupling constant K_{lm}

$$K_{lm} + a^2(\mu^2 - \omega^2) = l(l+1) + \sum_{k=1}^{\infty} c_k a^{2k}(\mu^2 - \omega^2)^k, \tag{5.9}$$

where the coefficients c_k may be found in Ref. [92].

As $r \to r_H$, the radial function (with the critical frequency (5.7)) admits a power series expansion,

$$R_{lm} = R_0\left(1 + \sum_{k\geq 1} R_k(r - r_H)^k\right), \tag{5.10}$$

with R_0 being an arbitrary nonzero constant. The coefficients R_k are found by replacing Eq. (5.10) into Eq. (5.2), and solving it order by order in terms of $(r - r_H)$. In our numerical computations, we have considered only the $k = 1, 2$ terms in (5.10) and took, without loss of generality, $R_0 = 1$. The R_k exhibit a non-elucidating dependence on the background parameters (r_H, a, Q), on q and on the quantum numbers (l, m); thus we shall not exhibit them here.

Then, starting with the near horizon expansion (5.10), we search for values of a for which the radial function R_{lm} goes to zero (exponentially) at infinity, as given by the second relation in Eq. (5.6). The numerical integration of Eq. (5.2) results in a one-parameter shooting problem. We have found that, for given input parameters $(r_H, Q, q; l, m)$, solutions with the right asymptotics exist for a discrete set of a, which can be labeled by the number n of nodes of the radial function R_{lm}. In this way we determine the existence lines of the clouds with a given set of quantum numbers, in the parameter space of Kerr-Newman black holes.

We shall now present the results obtained numerically for the clouds. Firstly, we consider the case of a massive scalar field in the Kerr spacetime ($Q = 0$ and $q = 0$); then we discuss the case of a massive charged scalar field in the Kerr-Newman spacetime. We always assume the cosmic censorship hypothesis, so that the singularities are hidden by event horizons; in other words, we never consider over-extreme backgrounds.

5.2 Kerr black hole

For Kerr black holes, the scalar field critical frequency (ω_c) and the background horizon angular velocity are related by $\Omega_H = \omega_c/m$. The existence lines for nodeless clouds and $l = m = 1, 2, 3, 4, 10$ were first exhibited in [59], using a black hole mass M vs. horizon angular velocity Ω_H diagram. This particular type of diagram parameterizes the 2-dimensional parameter space of Kerr black holes in an appropriate way for this problem, due to the relation between the scalar field frequency and the horizon angular velocity. As such, we shall herein represent existence lines using the same type of diagram.

In Fig. 5.1 we plot the existence lines for the clouds with different node numbers, $n = 0, 1, 2$, and angular momentum harmonic indices, $l = m = 1, 2$. As mentioned before, the lines with $n = 0$ and $l = m = 1, 2$ have already been presented in Ref. [59]. The main trend concerning these lines is that as $l = m$ is increased the lines move towards smaller Ω_H. The main new feature presented here is that the solutions with nodes move towards larger values of Ω_H as compared to nodeless solutions with the same l, m, converging to the latter when $M \to 0$. In Section 5.5 we shall provide an intuitive interpretation for the behavior of these and the following existence lines.

It was briefly mentioned in Ref. [59] that the existence lines for nodeless clouds with a given value of m and $l > m$ always move towards larger Ω_H values than the corresponding ones with $m = l$. This is illustrated in Fig. 5.2. The trend we have seen in Fig. 5.1 for the existence lines with nodes establishes a similar pattern when l, m are fixed and we increase n. As such, fixing m, the existence line for any n, l that stands on lowest values of Ω_H is the $n = 0$, $l = m$ line. We recall that the region to the right of a given existence line – in this type of diagram – consists of background spacetimes that are superradiantly

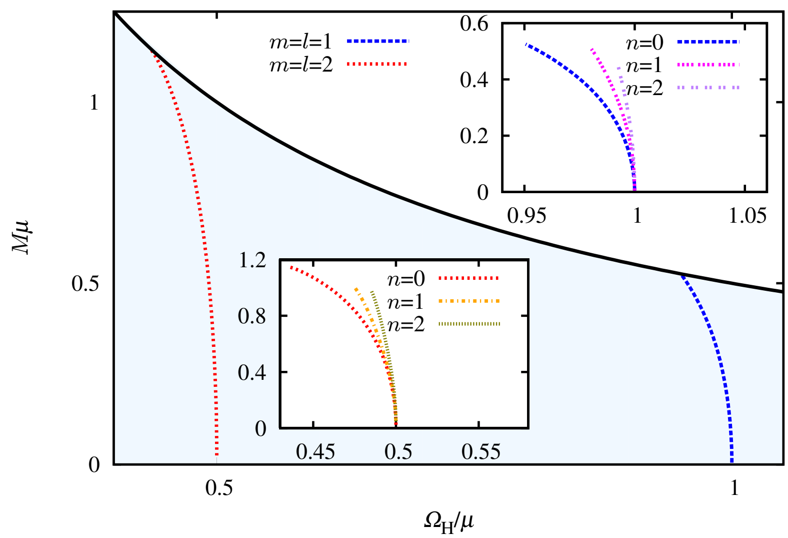

Figure 5.1: Existence lines for scalar clouds with various quantum numbers in the mass vs. horizon angular velocity parameter space of Kerr black holes. The black solid curve represents the extreme case, $a = M$ and Kerr solutions exist below this line. The blue dashed and red dotted lines represent the nodeless solution for $m = l = 1$ and $m = l = 2$, respectively. The insets compare the nodeless solutions ($n = 0$) with the solutions with $n = 1, 2$.

unstable against that particular mode. Consequently, the $m = l$, $n = 0$ existence line defines the boundary of the region between stable and unstable Kerr solutions for a given m mode.

Although there is no general analytic formula for the clouds' existence lines, some limiting cases have been considered in the literature which led to analytic formulas valid within some approximation. Here we shall discuss two such limits, one that applies to fast rotating black holes and another that applies to slowly rotating black holes.

In Ref. [58] Hod first discussed the clouds for the extremal Kerr black hole and in Ref. [94] extended his results for near-extremal black holes, obtaining an analytic approximation given by (cf. Eq. (32) in Ref. [94])

$$\mu = m\Omega_H[1 + 2\bar{\epsilon}^2] \,, \tag{5.11}$$

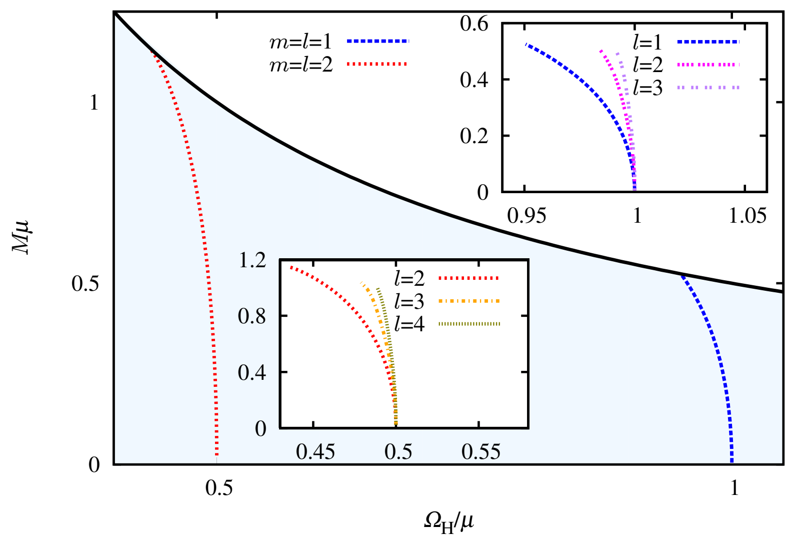

Figure 5.2: Analogous plot to Fig. 5.1, but now the insets compare the solutions for $m = l$ with the solutions with $m < l$, all with $n = 0$.

where

$$\bar{\epsilon} = \frac{m}{2(d+1+2n)} - \frac{m^3}{4d(d+1+2n)^2}\left(\frac{r_H - r_-}{r_H}\right) \tag{5.12}$$

and $d = \sqrt{(2l+1)^2 - 4m^2}$. From these equations we can obtain the existence line for a given cloud with quantum numbers (n, l, m) and for *rapidly* rotating black holes, i.e. near extremality. In Fig. 5.3, however, we plot such line for $n = 0$, $l = m = 1$ in an M vs. a/M diagram for Kerr, but *extrapolating* the formula for all values of a/M.

Another analytic formula can be obtained from the classic work of Detweiler [95], who studied superradiance for small values of the mass coupling, $M\mu \ll 1$. His results can be specialized to the critical frequency $\omega_c = m\Omega_H$. Since $\omega < \mu$ for bound states, we obtain that Detweiler's results apply to *slowly* rotating black holes, i.e. $\Omega_H M \ll 1$; then, an analytical formula can be obtained (solving Eq. (26) of Ref. [95] for μ), namely:

$$\mu = \frac{1}{\sqrt{2}}\left[\frac{p^2}{M^2} - \frac{\sqrt{p^2(p^2 - 4M^2m^2\Omega^2)}}{M^2}\right]^{1/2}, \tag{5.13}$$

where $p = l + n + 1$. In Fig. 5.3 we plot the corresponding existence line for $l = m = 1$ and $n = 0$, extrapolating to all values of a. In this figure, besides the approximations derived from Eq. (5.11) and Eq. (5.13), we plot our numerical results, which are valid (and accurate) for all values of a/M. Somewhat unexpectedly, the analytic approximations are still accurate, well outside their regime of validity. Thus, even though the solution of Detweiler is supposed to be valid only in the slowly rotating case, we see that the numerical and the Detweiler curves overlap in almost all the range for a/M. In the inset it is possible to see that the numerical result tends to the Hod curve close to extremality, as expected. In Fig. 5.4 a similar comparison is made for $n = 0$ and $m = l = 3, 4$.

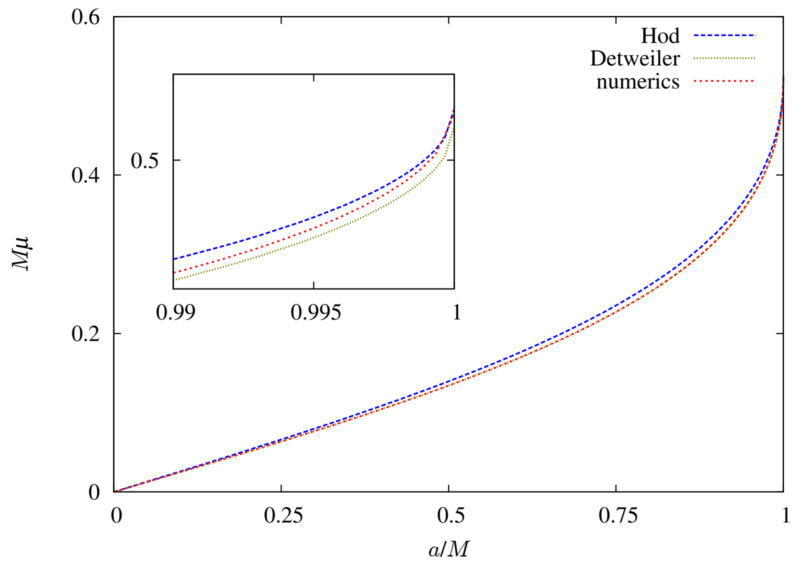

Figure 5.3: Comparison between our numerical solution for the clouds with $n = 0$, $m, l = 1$ and the analytical results by Hod [94], cf. Eq. (5.11), and Detweiler [95], cf. Eq. (5.13), in a mass vs. angular momentum parameter diagram for Kerr black holes.

5.3 Kerr-Newman black hole

In the Kerr-Newman case both the background and the test field have one more parameter. So, to exhibit the existence lines in a useful way, one must fix some quantities. In Fig. 5.5 we fix the background charge $\mu Q = 0.1$ and draw the existence lines for the cloud with $l = m = 1$ and $n = 0$ for various values of the field charge q. The overall trend is that clouds with the same (opposite) charge sign as the background occur for smaller (larger) angular velocities. This is an intuitive behavior. For instance, same charge sign implies Coulomb repulsion and hence require a smaller angular velocity from the background to

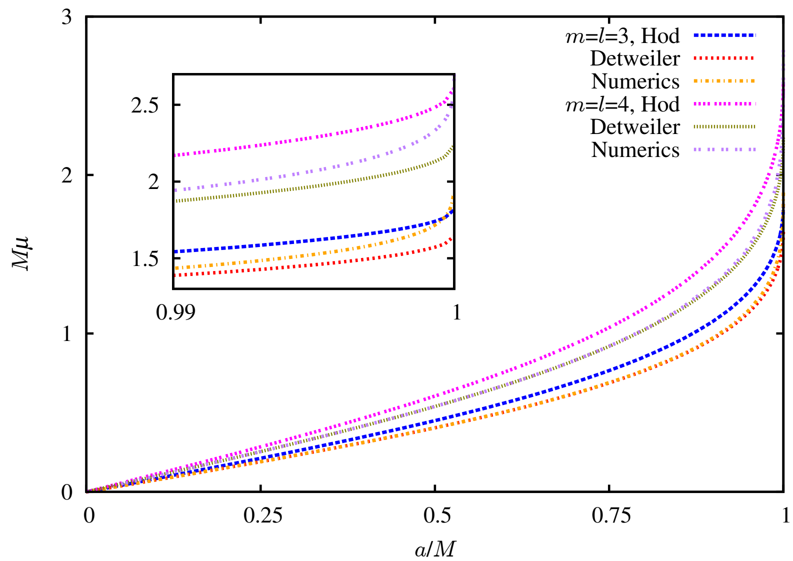

Figure 5.4: Analogous comparison to that in Fig. 5.3 but now for the clouds with $n = 0$, $m = l = 3, 4$. The agreement between the analytic and numerical approximations seems to become slightly worse, outside their regime of validity, when the quantum numbers $m = l$ increase.

maintain the equilibrium.

Another distinct feature of the charged existence lines, already seen in Fig. 5.5 but more clearly exhibited in Figs. 5.6 and 5.7 is that the existence lines do not reach $M = 0$, since the inclusion of background charge implies in a minimum value for the background mass, i.e. $|Q| < M$. Moreover, Fig. 5.6 confirms the trend that increasing the Coulomb repulsion between the field and the background implies that for the same background mass the clouds exist for lower background angular velocity.

Finally, fixing both the background and field charge, the variation of the existence lines when the field's angular momentum quantum numbers are increased is qualitatively similar to that seen in the Kerr case, namely the lines move towards lower angular velocities, as it can be seen in Fig. 5.7. This may be interpreted as a trade off between the angular momentum of the background and that of the cloud, as to maintain equilibrium. Another interesting feature in Fig. 5.7 is that, as the minimum background mass is approached, the angular velocity of the background tends to zero. Observe that the minimum background mass is precisely equal to the charge $\mu Q = \mu M = 0.1$, and that the field mass and charge

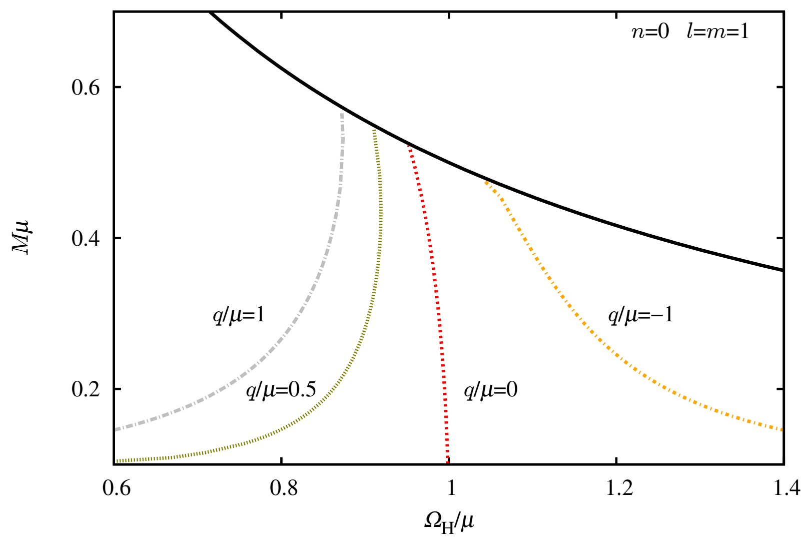

Figure 5.5: Existence lines for charged scalar bound states in the Kerr-Newman background, for $n = 0$ and $l = m = 1$, for different values of the field charge and fixed background charge $\mu Q = 0.1$.

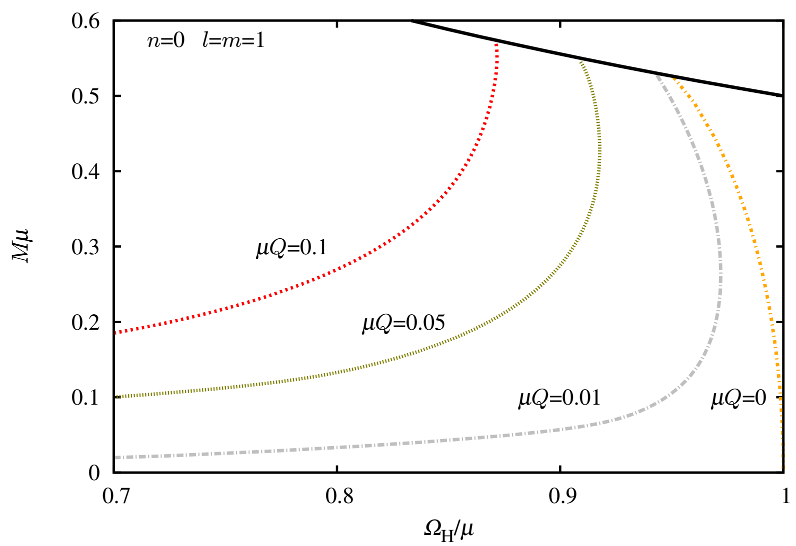

Figure 5.6: Existence lines for charged scalar bound states in the Kerr-Newman background, for $n = 0$ and $l = m = 1$, for different values of the background charge and fixed field charge $q/\mu = 1$.

are also the same $q/\mu = 1$. Thus, the limiting equilibrium configuration is a *marginal* *(charged) cloud* of the type discussed in Refs. [96, 97].

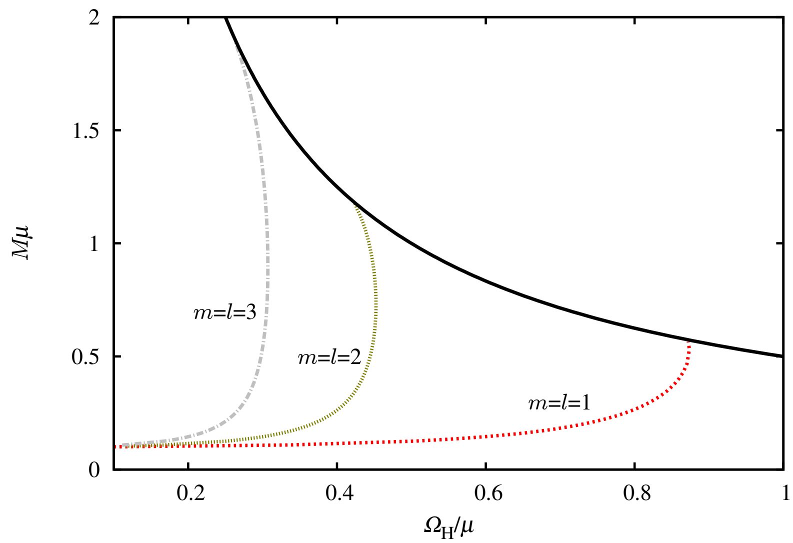

Figure 5.7: Existence lines for charged scalar bound states in the Kerr-Newman background, for $\mu Q = 0.1$, $q/\mu = 1$, $n = 0$ and $m = l = 1, 2$ and 3.

As for the Kerr case, we can compare our numerical results for the Kerr-Newman case with an analytic formula. The latter was obtained from the results of Furuhashi and Nambu [98]. First we note that these authors have shown that in order to have bound states we must have

$$M\mu \gtrsim Qq \ . \tag{5.14}$$

Then they obtained an expression for the real part of the frequency for $M\mu \ll 1$ and $Qq \ll 1$ (cf. Eq. (26) of Ref. [98]). From that expression, we find the analytic formula

$$\mu = \mathcal{R}\left[\frac{2qQ}{3M} + \frac{(1-i\sqrt{3})(6p^2+q^2Q^2)M^2}{2^{2/3}3M^2A} + \frac{(1+i\sqrt{3}A)}{2^{1/3}6M^2}\right] , \tag{5.15}$$

where

$$\begin{aligned} A &= \{-36p^2M^3qQ + 2M^3q^3Q^3 + 54g^2M^4\omega_c \\ &+ [4(-6p^2M^2 - M^2q^2Q^2)^3 \\ &+ 4M^6(-18p^2qQ + q^3Q^3 + 27p^2M\omega_c)^2]^{1/2}\}^{1/3}. \end{aligned} \tag{5.16}$$

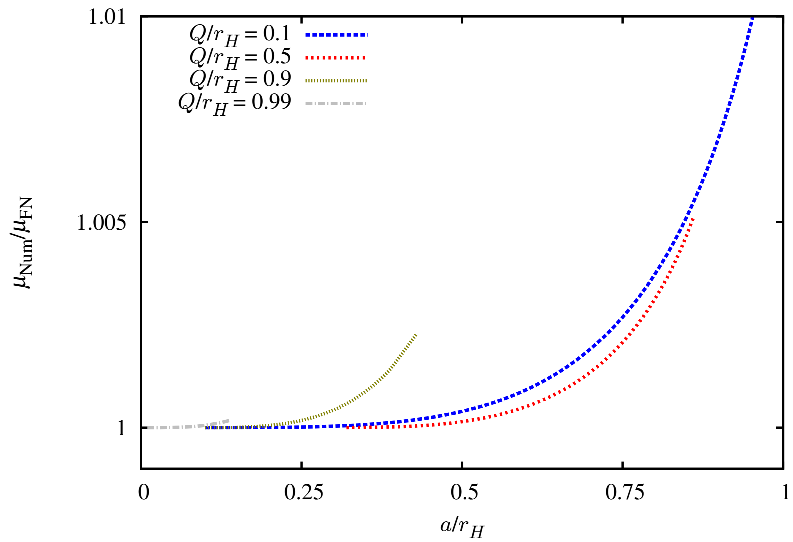

Figure 5.8: Comparison between our numerical solutions and the analytical formula by Furuhashi and Nambu [98], cf. Eq. (5.15), for clouds with $n = 0$, $m = l = 1$ and $qr_H = 0.1$. The numerical and analytical formulas coincide with very good accuracy.

In Fig. 5.8 we compare this analytic formula with our numerical results and, again, conclude that the analytic formula works remarkably well. Observe that in the Kerr-Newman case the existence lines cannot extend in the whole range of a, since they are constrained by the conditions (5.14) and $a^2 + Q^2 < M^2$.

5.4 Clouds tomography

5.4.1 Angular functions

The angular dependence is given by the spheroidal harmonics, $S_{lm}(\theta)$. These harmonics depend on the background angular momentum parameter a. $S_{lm}e^{im\phi}$ reduces to the standard spherical harmonics Y_{lm} when $a = 0$, up to a (l, m)-dependent normalization factor. Since one is typically less familiar with these spheroidal harmonics (than with the spherical harmonics) we will illustrate their angular distribution.

In Fig. 5.9 we give a 3-dimensional plot of some spheroidal harmonics for $\mu r_H = 0.5$. As we increase the value of $l = m$, S_{lm} becomes more flattened, as for spherical harmonics. For the cases plotted, the difference between spherical and spheroidal cases is essentially only an overall scale factor, i.e. the angular distribution is very similar. Obviously the angular dependence is independent of considering the Kerr or the Kerr-Newman background.

In Fig. 5.10 we display a density plot of the absolute value of the spheroidal harmonics over a sphere of unitary radius. The function is normalized, such that it varies between zero and one.

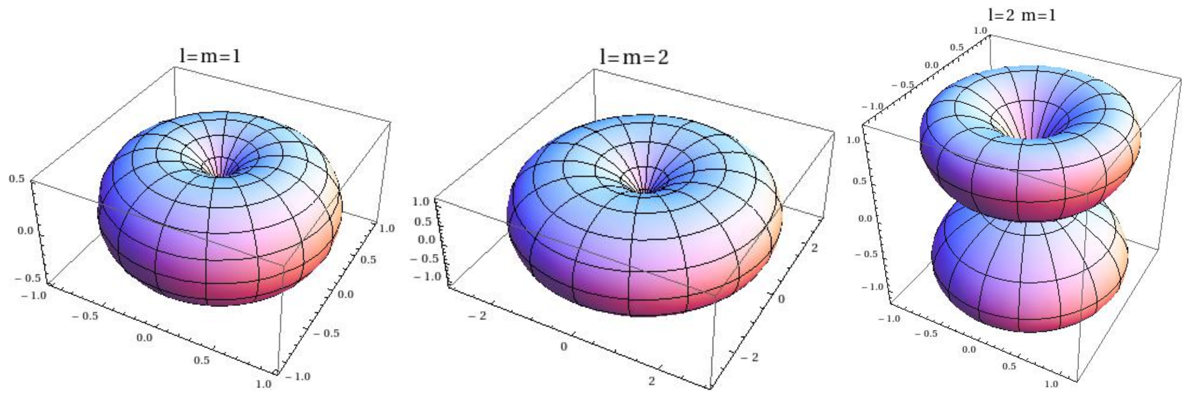

Figure 5.9: 3-dimensional plots of the spheroidal harmonics $|S_{lm}(\theta)|$. All three panels were obtained for $\mu r_H = 0.5$. These correspond, from left to right to $\mu a = 0.399$, $\mu a = 0.133$ and $\mu a = 0.430$.

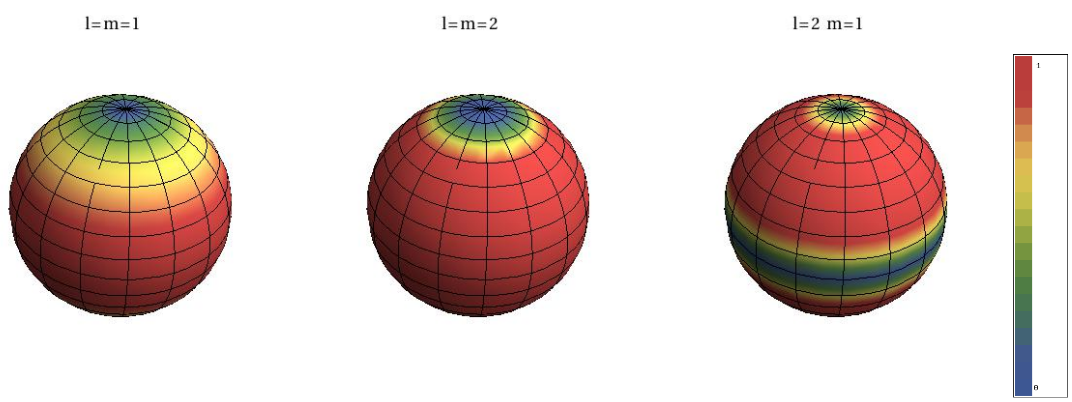

Figure 5.10: Density plots of the spheroidal harmonics $|S_{lm}(\theta)|$ over a sphere of unitary radius. Note that the plot is normalized. All three panels were obtained for $\mu r_H = 0.5$. These correspond, from left to right to $\mu a = 0.399$, $\mu a = 0.133$ and $\mu a = 0.430$.

5.4.2 Radial functions

The radial dependence of the clouds is quite simple and is illustrated in Figs. 5.11 (for Kerr) and 5.12 (for Kerr-Newman), for some values of the rotation parameter, for two values of $l = m$ and for three different numbers of nodes n. The scalar field is always finite on and outside the horizon. On the horizon it needs not be zero. For instance, for $l = m = 1$ clouds it is non-zero on the horizon, cf. Figs. 5.11 and 5.12. Then, the radial function will have n nodes and decrease exponentially asymptotically.

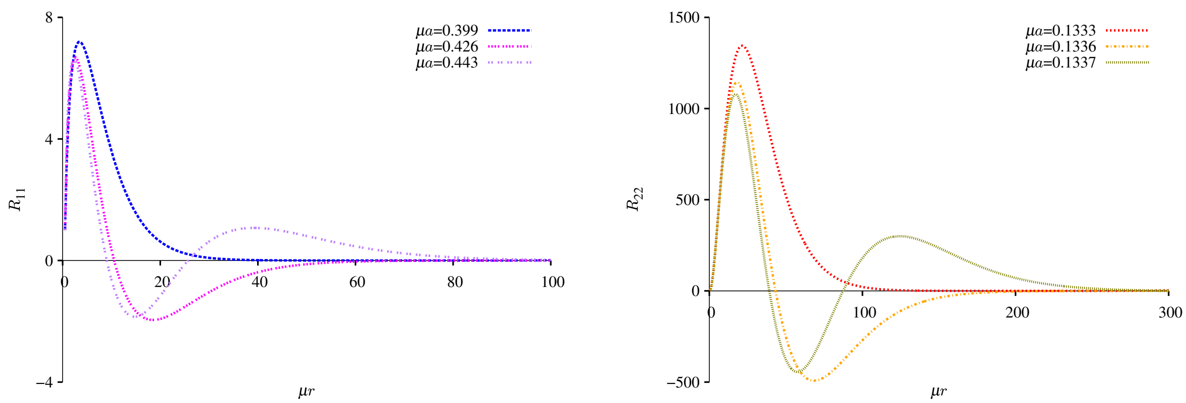

Figure 5.11: Radial solutions R_{11} (left), R_{22} (right) for clouds with $n = 0, 1, 2$ in the Kerr background with $\mu r_H = 0.5$. The corresponding values of a are given in the figure key.

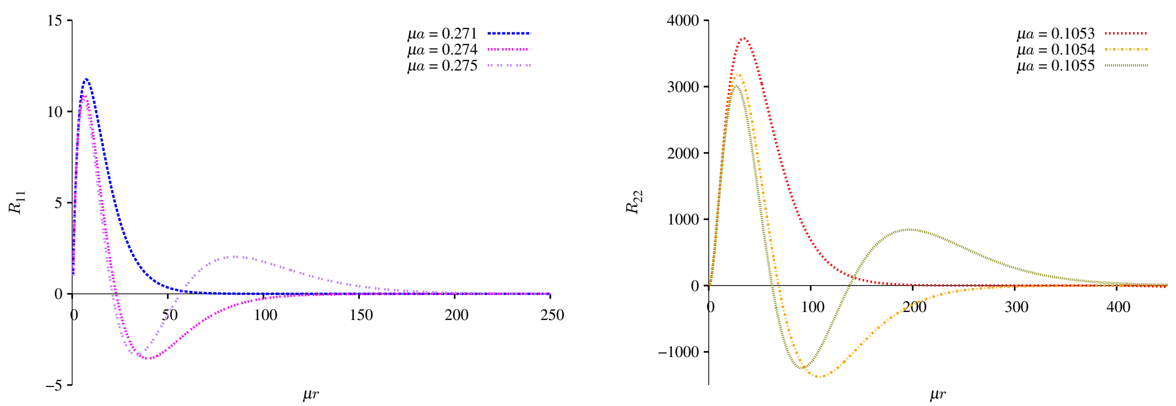

Figure 5.12: Radial solutions R_{11} (left), R_{22} (right) for clouds with $q/\mu = 1$ and $n = 0, 1, 2$ in the background of Kerr-Newman with $\mu r_H = 0.5$, $Q\mu = 0.1$. The corresponding values of a are given in the figure key.

Given the radial profiles, one may ask how close to the horizon the clouds are concentrated. In order to gain some insight into this question, we have plotted in Fig. 5.13 the "position" of the cloud with $l = m = 1, 2, 3, 4, 5, 10$ and $n = 0$. By "position" we mean the value or r, denoted r_{MAX}, for which the function $4\pi r^2 |R_{lm}|^2$ attains its maximum value, cf. Ref. [58]. We can see that as a/M decreases, r_{MAX}/M increases, diverging as $a \to 0$. This behavior is consistent with the fact that Schwarzschild black holes do not support clouds. As extremality is approached, $a \to M$, on the other hand, we recover the result by Hod [e.g, for $l = m = 1$, $r_{MAX}(a/M = 1) = 9.557M = 9.557r_H$]. It is curious to note that our results for small $l = m$ are in agreement with the 'no-short hair' conjecture [99], which states that the 'hair' should extend beyond $3r_H/2$ (which coincides with the position of the circular null geodesic (CNG) for the Schwarzschild case). But for large $l = m$, the maximum, r_{MAX}, approaches the Kerr horizon, as $a \to M$, in agreement with the behavior of the co-rotating CNG [100], which is also plotted in Fig. 5.13. The fact that for large $l = m$, the cloud's "position" can approach arbitrarily close to the horizon was first noted by Hod using the eikonal approximation [101]. These observations support the idea that a more universal measure of the minimal hair extension, valid beyond static black holes, is given by the size of the CNG [102].

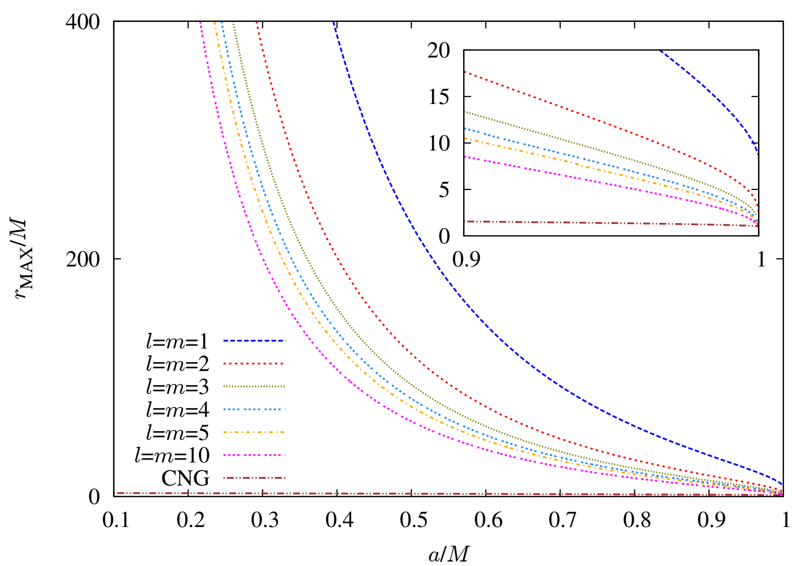

Figure 5.13: "Position" of the clouds, r_{MAX}/M (see definition in the text), as a function of a/M for a cloud with $n = 0$, $l = m = 1$ in the Kerr background.

Finally, in order to have an overview of the full spatial distribution of the clouds and of their energy density, we exhibit in Fig. 5.14 a three dimensional plot of both the scalar field distribution (left panel) and the energy density (right panel), for a cloud with $n = 0$, $l = m = 1$. The particular cloud plotted occurs for background values $r_H/M = 1.46$ and $a/M = 0.89$. For the plot we have normalized the scalar field mode such that $|\Psi_{11}(r = r_H, \theta = \pi/2)| = 1$. The plot takes the Boyer-Lindquist coordinates (r, θ), as standard spherical coordinates and uses the "polar" coordinates $z = r\cos\theta$ and $\rho = r\sin\theta$. Observe that both the scalar field and the energy density are localized in a toroidal region, well beyond r_H. This is expected by virtue of the angular distribution of the corresponding spheroidal harmonic, shown in Figs. 5.9 and 5.10. Note that the scalar field vanishes on the z-axis. Also, the white space around the origin corresponds to the event horizon (a semi-circle, more clearly seen on the left panel), where the scalar field is non-zero. The energy density plotted is the time-time component of $T_\beta{}^\alpha$, where the scalar field energy-momentum tensor is:

$$T_{\alpha\beta} = 2\Phi^*_{,(\alpha}\Phi_{,\beta)} - g_{\alpha\beta}[\Phi^*_{,\gamma}\Phi^{,\gamma} + \mu^2\Phi^*\Phi] \ . \tag{5.17}$$

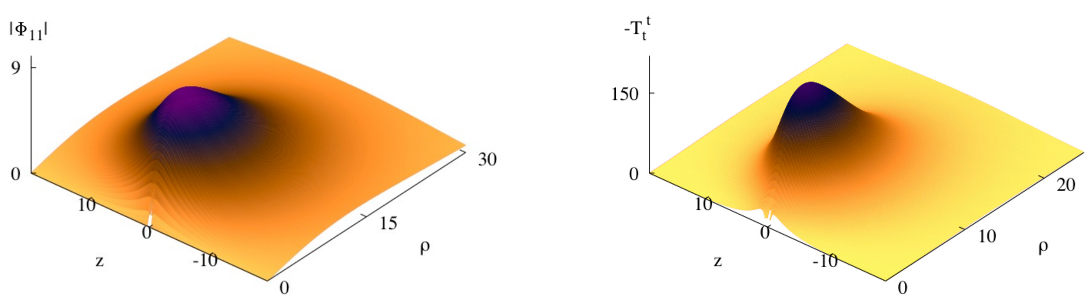

Figure 5.14: Three dimensional spatial distribution of a cloud (left panel) with $n = 0$ and $m = l = 1$ and its energy density (right panel) in terms of "polar" coordinates (ρ, z). Both are essentially supported along an equatorial torus, due to the angular distribution of the corresponding spheroidal harmonic.

5.5 Discussion

In the Kerr case, the dependence of the existence lines with the quantum numbers (n, l, m) can be summarized as follows. In a black hole mass (M) vs. black hole horizon angular velocity (Ω_H) diagram:

- Nodeless lines $(n = 0)$ with $m = l$ are approximately vertical lines and occur for decreasing values of Ω_H as the angular quantum numbers $l = m$ increase. Lines with different values of $l = m$ are disconnected. This is in agreement with the naive expectation that the collapse of the cloud is prevented by (stationary) rotation effects and that decreasing the rotation of the black hole one must increase the rotation of the cloud and vice-versa. This overall trend had already been observed in Ref. [59].

- Fixing $m = l$ and increasing the number of nodes n, i.e. moving to more excited configurations, the existence line moves to slightly higher values of Ω_H. All these lines are connected: they converge when the black hole mass tends to zero. Again, a naive interpretation is that clouds with nodes are excited states, hence more energetic and thus require a larger background rotation for equilibrium. Their "weight" however, becomes irrelevant as the background mass vanishes, which agrees with the convergence of these existence lines in the $M \to 0$ limit.

- Fixing m and n and increasing l, again the existence line moves to slightly higher values of Ω_H, and again all these lines are connected as the black hole mass tends to zero. This overall trend was also briefly mentioned in Ref. [59].

Adding charge to both the background and the field introduces two qualitatively new effects in the same type of diagram as before:

- When the background charge and the field charge have the same (opposite) sign, the existence line for a given set of quantum numbers moves to lower (higher) values of Ω_H, for fixed M. Again, this is in agreement with the naive expectation that there is now Coulomb repulsion (attraction) between the background black hole and the cloud that needs to be balanced by smaller (higher) background rotation.

- The existence lines stop being essentially vertical. The reason is that they cannot approach the $M \to 0$ limit, since there is a minimal black hole mass for a given black hole charge Q which still allows the existence of an event horizon. In the $Qq > 0$ case, fixing the field charge equal to the field mass, one observes that as the minimal mass is approached, then $\Omega_H \to 0$ and $M \to Q$. The configuration approached is a marginal charged cloud, in the nomenclature of Ref. [97].

We have also described the spatial distribution of the clouds. A full picture is obtained by describing the angular and radial dependence separately. We have given examples of both spheroidal harmonics and of radial functions. An interesting property of the latter is that an appropriately defined radial "position" for the clouds increases as the rotation of the background decreases. Thus, the smaller radial position is obtained for extremal black holes and it is in agreement with a generalization of the 'no-short hair' conjecture suggested by Hod [102].

As already observed, cloud solutions can be taken as a smoking gun for the existence of Kerr-(Newman) black holes with scalar hair, as fully non-linear solutions of the Einstein-Klein-Gordon(-Maxwell) system [59]. But that does not imply that all hairy black holes are revealed by such a test field analysis. A remarkable example concerns Myers-Perry black holes, which can support a scalar hair which relies on non-linear effects [103].

The analysis in this work was restricted to the simple case of scalar fields on Kerr(-Newman) black holes, for which the wave equation separates. Similar results are expected to hold as well for other rotating black hole backgrounds afflicted by superradiant instabilities, as well as other fields that may trigger such instabilities. In all such cases scalar (or other spin fields) clouds should occur at the threshold of the superradiant instability. One particularly interesting case that we expect is the existence of Proca clouds around Kerr black holes (see [97] for the study of Proca quasi-bound states around Schwarzschild black holes).

We would also like to comment on the stability of the clouds discussed in this work. Since they only exist along lines in the Kerr 2-dimensional parameter space, one may expect that the clouds are unstable solutions. An argument that they are actually dynamical attractors is the following. First observe that ω/m defines an angular velocity for the cloud. The bound state condition $\omega = \omega_c = m\Omega_H$, can then be interpreted as the angular velocity of the cloud being synchronous with that of the black hole horizon. Now let us fix a Kerr background with a given horizon angular velocity Ω_H and consider a quasi-bound state with a frequency $\mathcal{R}(\omega)$ slightly smaller (larger) than ω_c. The quasi-bound state will be in the superradiant (decaying) regime. Thus it will be amplified (absorbed) by the black hole. Following the evolution of the background black hole in a quasi-static approximation, the black hole loses (gains) mass and angular momentum and its angular velocity decreases (increases). The process only stops when the horizon angular velocity of the evolving black hole approaches $\Omega_H \to \mathcal{R}(\omega)/m$, at which point the imaginary part of the quasi-bound state frequency approaches zero. Thus it seems plausible that clouds are dynamical equilibrium configurations; in other words, that dynamics wants to lock quasi-bound states in synchronous rotation with the black hole. This argument is reminiscent of the synchronization of orbital and rotation periods of astronomical bodies (like the Moon-Earth system) due to tidal effects and friction. This analogy supports the idea of a connection between tidal acceleration and superradiant scattering around spinning black holes [104].

Finally, a more involved picture is found when turning on a suitable self-interaction potential of the scalar field. Then the (non-linear) Klein-Gordon equation possesses bound state solutions already in a flat spacetime background – *the Q-balls* [105, 106]. Remarkably, spinning Q-balls survive when replacing the Minkowski background with a Kerr metric, provided the relation (5.8) connecting the scalar field frequency and the black hole event horizon velocity is satisfied (note that the variables do not separate in this case). The resulting solutions exhibit a more complicated pattern than the clouds presented herein, covering a compact region of the 2-dimensional parameter space of the Kerr black holes, rather than existence lines [107].

Chapter 6

Clouds in acoustic analogues

Under certain conditions sound waves in fluids experience an acoustic horizon with analogue properties to those of a black hole event horizon. In particular, a draining bathtub-like model can give rise to a rotating acoustic horizon and hence a rotating black hole (acoustic) analogue. We show that sound waves, when enclosed in a cylindrical cavity, can form stationary waves around such rotating acoustic holes. These acoustic perturbations display similar properties to the scalar clouds that have been studied around Kerr and Kerr-Newman black holes; thus they are dubbed *acoustic clouds*. We make the comparison between scalar clouds around Kerr black holes and acoustic clouds around the draining bathtub explicit by studying also the properties of scalar clouds around Kerr black holes enclosed in a cavity. Acoustic clouds suggest the possibility of testing, experimentally, the existence and properties of black hole clouds, using analog models.

6.1 Massless scalar field in the Kerr background

To solve the Klein-Gordon equation for a *massless* scalar field, $\Box\Phi = 0$, on the Kerr background, we make a harmonic/Fourier decomposition of the scalar field, which is considered to be a sum of modes of the type $\Phi_{lm} = e^{i(m\phi-\omega t)}S_{lm}(\theta)R_{lm}(r)$ and use the line element given by (1.15). For this case we find the radial equation

$$\Delta\frac{d}{dr}\left(\Delta\frac{dR_{lm}}{dr}\right) + \left[H^2 + (2ma\omega - K_{lm})\Delta\right] R_{lm} = 0 \qquad (6.1)$$

where $H \equiv (r^2 + a^2)\omega - am$ and K_{lm} are separation constants which come from the spheroidal harmonics.

In the limit $r \to r_H$ we require a purely ingoing wave, while in the asymptotic case we have an outgoing wave:

$$R_{lm}(r) \approx \begin{cases} e^{-i(\omega-\omega_c)r_*}, & \text{for } r \to r_H \ , \\ e^{i\omega r_*}, & \text{for } r \to \infty \ . \end{cases} \tag{6.2}$$

With the solutions given by (6.2) no stationary configurations exist. To have such solutions we shall impose, besides $\omega = \omega_c$, a different boundary condition, as we shall describe in Section 6.3.

6.2 Massless scalar field in the draining bathtub background

In order to find the solution of the massless Klein-Gordon equation in the draining bathtub effective geometry given by Eq. (1.42) we again consider a Fourier/mode decomposition. The modes have the form

$$\Phi_m(r,\phi,t) = e^{i(m\phi-\omega t)}\psi_m(r), \tag{6.3}$$

where $\psi_m(r)$ obeys

$$\frac{1}{r}\left(1-\frac{A^2}{r^2}\right)\frac{d}{dr}\left[r\left(1-\frac{A^2}{r^2}\right)\frac{d\psi_m}{dr}\right] + \left[\omega^2 - \frac{2Bm\omega}{r^2} - \frac{m^2}{r^2}\left(1-\frac{A^2+B^2}{r^2}\right)\right]\psi_m = 0. \tag{6.4}$$

We can rewrite Eq. (6.4) as

$$\frac{d^2}{dr_*^2}\zeta_m + \left[\left(\omega - \frac{Bm}{r^2}\right)^2 - V_m(r)\right]\zeta_m = 0 \ , \tag{6.5}$$

with

$$V_m(r) = \left(1-\frac{A^2}{r^2}\right)\left[\frac{m^2-1/4}{r^2} + \frac{5A^2}{4r^2}\right] \ , \tag{6.6}$$

where $\zeta_m = \sqrt{r}\psi_m$ and the Regge-Wheeler coordinate can be defined by

$$\frac{d}{dr_*} = \left(1-\frac{A^2}{r^2}\right)\frac{d}{dr} \ . \tag{6.7}$$

We find that the solutions at the horizon and at infinity behave similarly as before

$$\psi_{\omega m}(r) \approx \begin{cases} e^{-i(\omega-\omega_c)r_*}, & \text{for } r \to r_H \ , \\ e^{i\omega r_*}, & \text{for } r \to \infty \ , \end{cases} \tag{6.8}$$

with

$$\omega_c = mB/A^2 = m\Omega_H \ . \tag{6.9}$$

6.3 Cloud configurations of a massless scalar field case

To find clouds, *i.e.* bound-state like solutions, we enclose the massless scalar field in a cavity whose boundary is located at

$$r = r_0 \ . \tag{6.10}$$

We impose two different boundary conditions to our problem: The first is of Dirichlet type, such that the scalar field vanishes at the cavity's boundary, $R_{lm}(r_0) = 0$. The second is a Neumann boundary condition, such that the derivative of the field vanishes at the cavity's boundary, $dR_{lm}(r_0)/dr = 0$[1].

6.3.1 Kerr black hole in a cavity

To obtain the radial function, we shall integrate Eq. (6.1) numerically. For that purpose, we consider the expansion (5.9) for the separation constants K_{lm}, with $\mu = 0$.

In Fig. 6.1 we display the mirror location r_0 in terms of the horizon angular velocity Ω_H, both scaled to the horizon radius, varying the cloud quantum numbers m, l and n, for both Dirichlet boundary conditions (left panels) and Neumann boundary conditions (right panels). The first observation is that, generically, $r_0/r_H \to \infty$, $\Omega_H \to 0$. This illustrates the fact that there are no massless clouds for Schwarzschild black holes in a

[1] These boundary conditions are associated to a cylindrical mirror with low (Dirichlet) and high (Neumann) acoustic impedance [108, 109], the latter being perhaps more easily implemented experimentally, since it corresponds to a rigid cylinder.

cavity. Indeed this is expected from the known results of the massive case: there are no (massive) scalar clouds for the Schwarzschild black hole, even though it is possible to have arbitrarily long-lived quasi-bound states [110]. The second generic observation is that, as we approach the mirror to the black hole horizon we need to increase Ω_H in order to have clouds. Conversely, and taking precisely the extremal case ($\Omega_H r_H = 0.5$), we observe that increasing the value of $m = l$ the position of the mirror tends to the horizon. We shall come back to this point later.

The dependence on the cloud's quantum numbers observed in Fig. 6.1 can be summarized as follows. Increasing $l = m$, implies that, for fixed mirror position r_0/r_H, clouds exist for smaller horizon angular velocity $\Omega_H r_H$. This trend is analogous to the one observed for massive scalar clouds (without mirror) in Ref. [67]. They can be heuristically interpreted in terms of a mechanical equilibrium between the black hole-cloud gravitational attraction and angular momentum driven repulsion due to the black hole-cloud energy currents, *cf.* Ref. [67]. Another feature we can see is that when we increase either n or l, for fixed r_0/r_H, the corresponding cloud occurs for bigger values of $\Omega_H r_H$. This is due to the fact that clouds with bigger n or l represent clouds with greater energy.

Finally concerning the differences between Dirichlet and Neumann boundary conditions, Fig. 6.1 shows that both cases present the same qualitative behavior, but that for the same angular velocity Ω_H, clouds with Neumann boundary conditions occur for a smaller r_0. This is quite natural, as one can always obtain a Neumann cloud from a Dirichlet cloud by decreasing the size of the cavity to where it stands at the point where the radial derivative of the radial function vanishes, which occurs inside the cavity with the Newman boundary condition.

Fig. 6.2 illustrates the radial profile of the massless scalar clouds for Dirichlet (left panel) and Neumann (right panels) boundary conditions for $l = m = 1$. For both cases we choose $r_0 = 20 r_H$ and show three distinct solutions corresponding to different numbers of nodes $n = 0, 1$ and 2. The radial profile has the typical form of standing waves with fixed boundary conditions.

Let us comment that we have verified qualitatively that similar clouds exist not only for *massive* but also for *self-interacting* scalar fields around Kerr black holes in cavity,

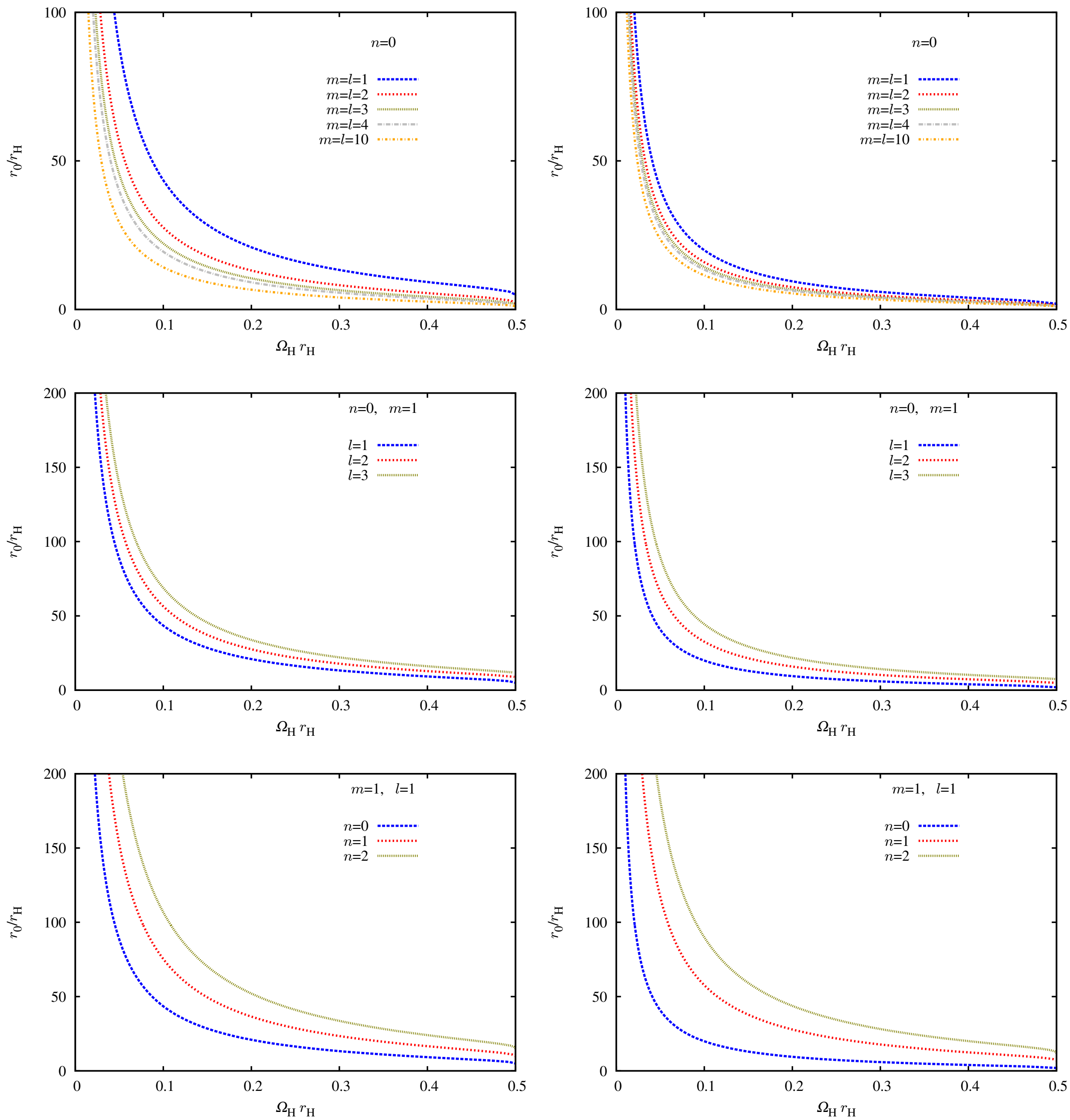

Figure 6.1: Massless scalar clouds around Kerr black holes surrounded by a mirror at $r = r_0$ with a Dirichlet (left panels) or a Neumann (right panels) boundary condition for different 'quantum numbers', as specified in the keys.

generalizing the ones studied in Ref. [107] for asymptotically flat spacetimes.

Fig. 6.3 shows the position of the clouds r_{MAX} compared with the radial value of the CNG for co-rotating orbits on the equatorial plane of the Kerr background. We see that as we increase the values of $l = m$ the cloud approaches the value of the CNG in the limit

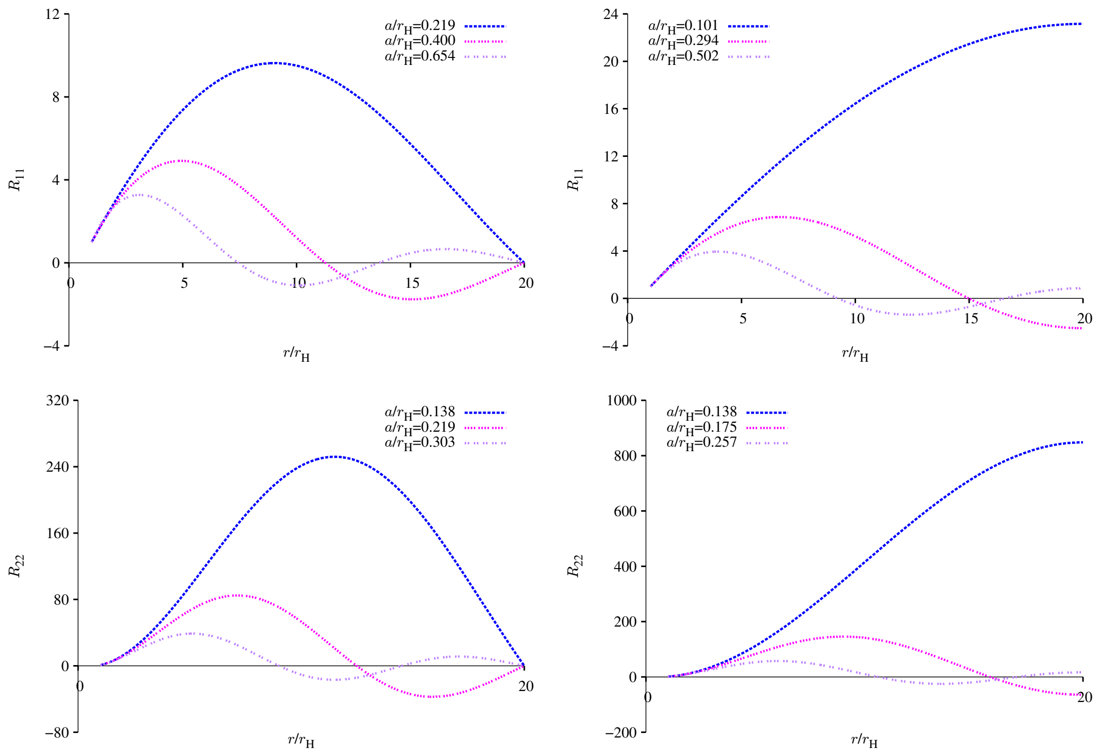

Figure 6.2: Radial solutions R_{11} with $r_0/r_H = 20$ for Dirichlet (left panels) and Neumann (right panels) boundary conditions.

$a/r_H \to 1$. Recall that, as observed earlier, when $a/r_H \to 1$, r_0 also tends to the horizon. Thus, the position of these massless clouds can be arbitrarily close to the black hole, in agreement with the results for the massive case.

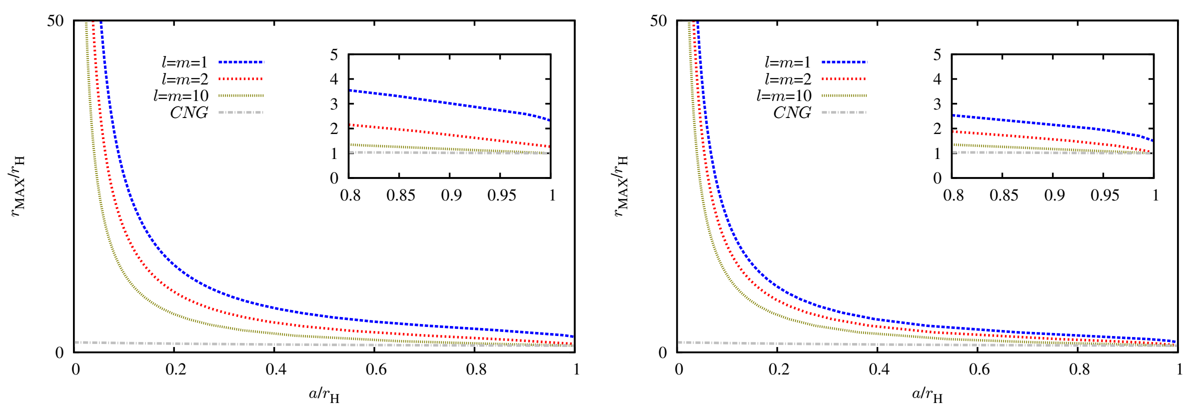

Figure 6.3: Position of the clouds for the Kerr case, for different values of $l = m$ compared with the CNG for Dirichlet (left panel) and Neumann (right panel) boundary conditions.

6.3.2 Draining bathtub

To find the acoustic clouds we integrate Eq. (6.4), considering $\omega = \omega_c$ and imposing mirror-like conditions. In the present case the clouds will be labelled by only two 'quantum numbers': the azimuthal harmonic index m and the node number n.

In Fig. 6.4 we compare clouds with different quantum numbers for Dirichlet and Neumann boundary conditions. The observed behavior is completely analogous to that seen for the Kerr case discussed in the previous subsection: (i) as $r_0/r_H \to \infty$, $\Omega_H \to 0$; (ii) as we approach the mirror to the acoustic hole, Ω_H increases; (iii) as m decreases, the angular velocity $\Omega_H r_H$ increases for fixed mirror position r_0/r_H; (iv) as n increases, the angular velocity $\Omega_H r_H$ increases for fixed mirror position r_0/r_H; (v) for the Neumann boundary condition the existence lines occur for smaller values of Ω_H, for the same r_0 chosen for Dirichlet boundary conditions.

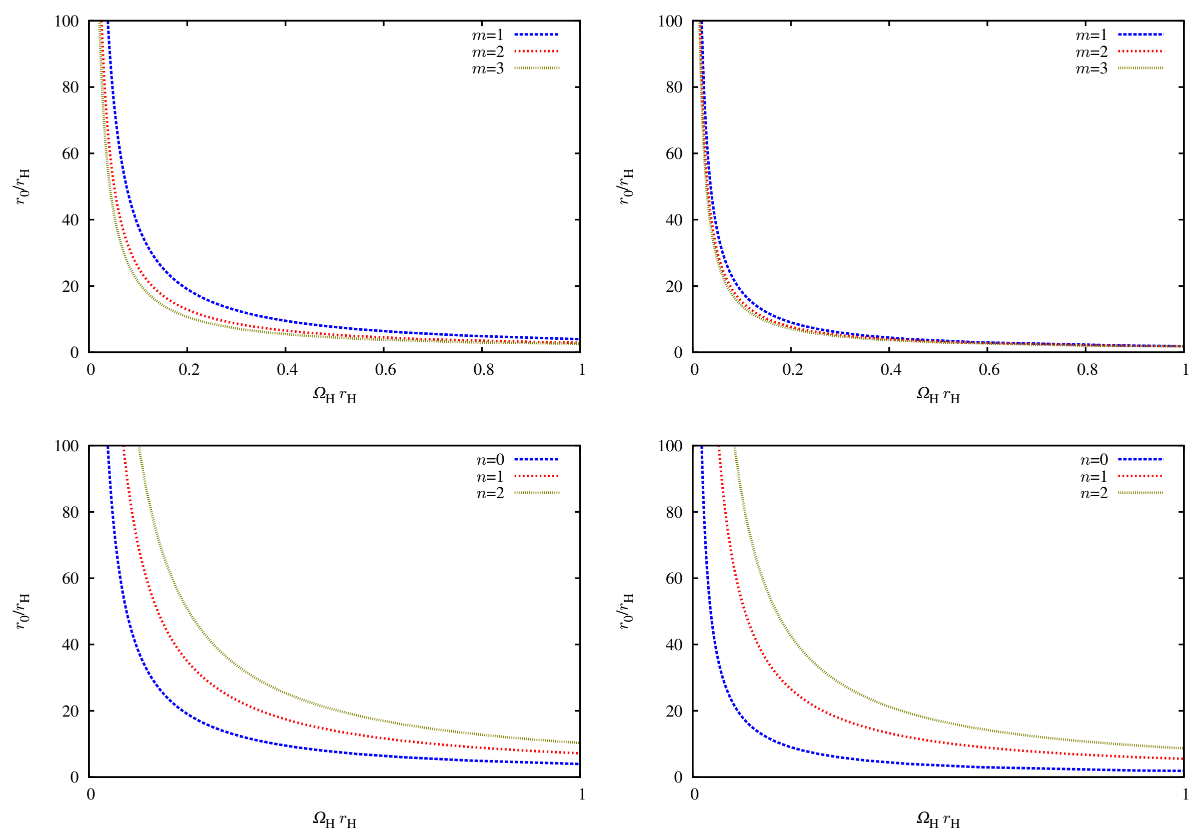

Figure 6.4: Massless scalar clouds for the draining bathtub for Dirichlet (left panel) and Neumann (right panel) boundary conditions, for different quantum numbers.

In Figs. 6.5, 6.6, 6.7 and 6.8 we make some 3-dimensional plots of the spatial distribution of acoustic clouds for Dirichlet and Neumann boundary conditions.

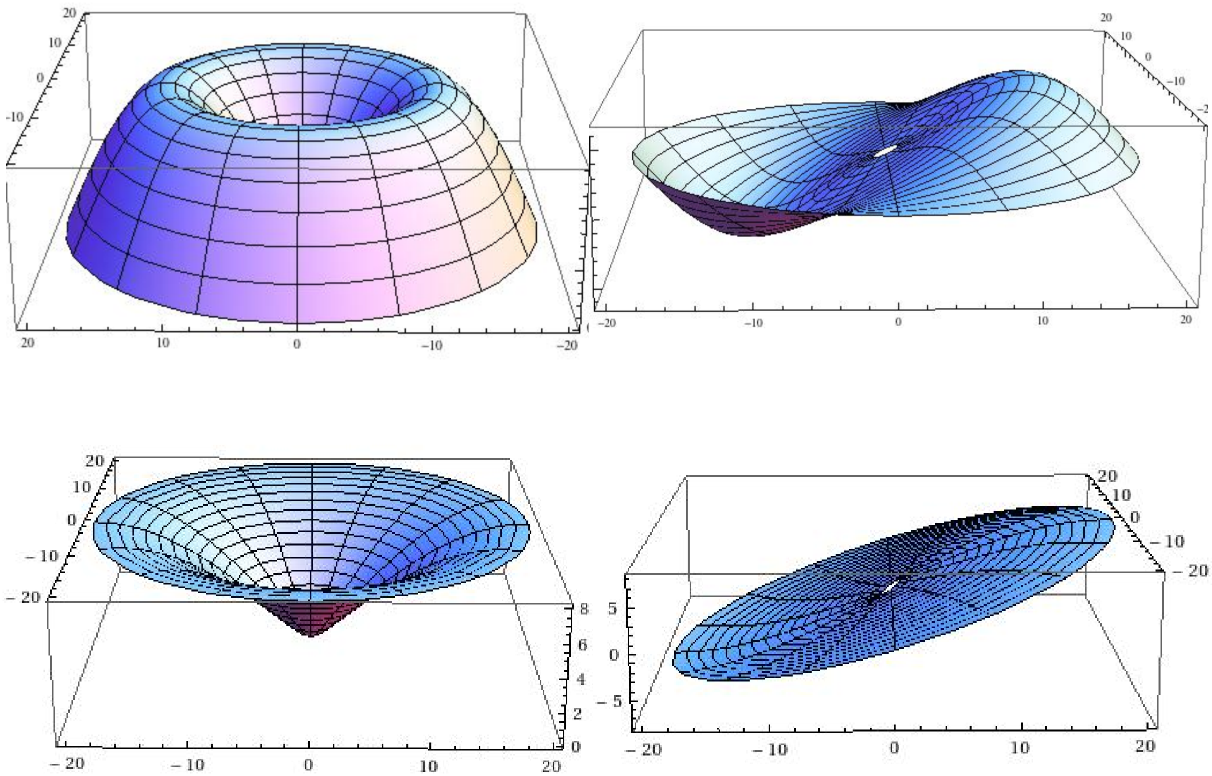

Figure 6.5: Acoustic clouds on the r, ϕ plane for Dirichlet (top) and Neumann (bottom) boundary conditions with $m = 1$ and $n = 0$. We plot the $|\Phi_m|$ on the left panels and the real part of Φ_m on the right panels. We fix the mirror position in $r_0/r_H = 20$, and the circulation is $B/r_H = 0.19$, for the Dirichlet case, and $B/r_H \simeq 0.09$, for the Neumann case.

One may wonder if an analytic solution may be found for Eq. (6.4). Studies of the draining bathtub model have actually concluded that the radial function in this case can be expressed in terms of Heun functions (see *e.g.* [111]). It seems, however, that not much use can be made of these functions to find the relevant information to obtain the acoustic clouds. For the acoustic hole, there is no theoretical restriction that prevents taking $B > A$; in other words, there is no extremal case for this analogue model, for

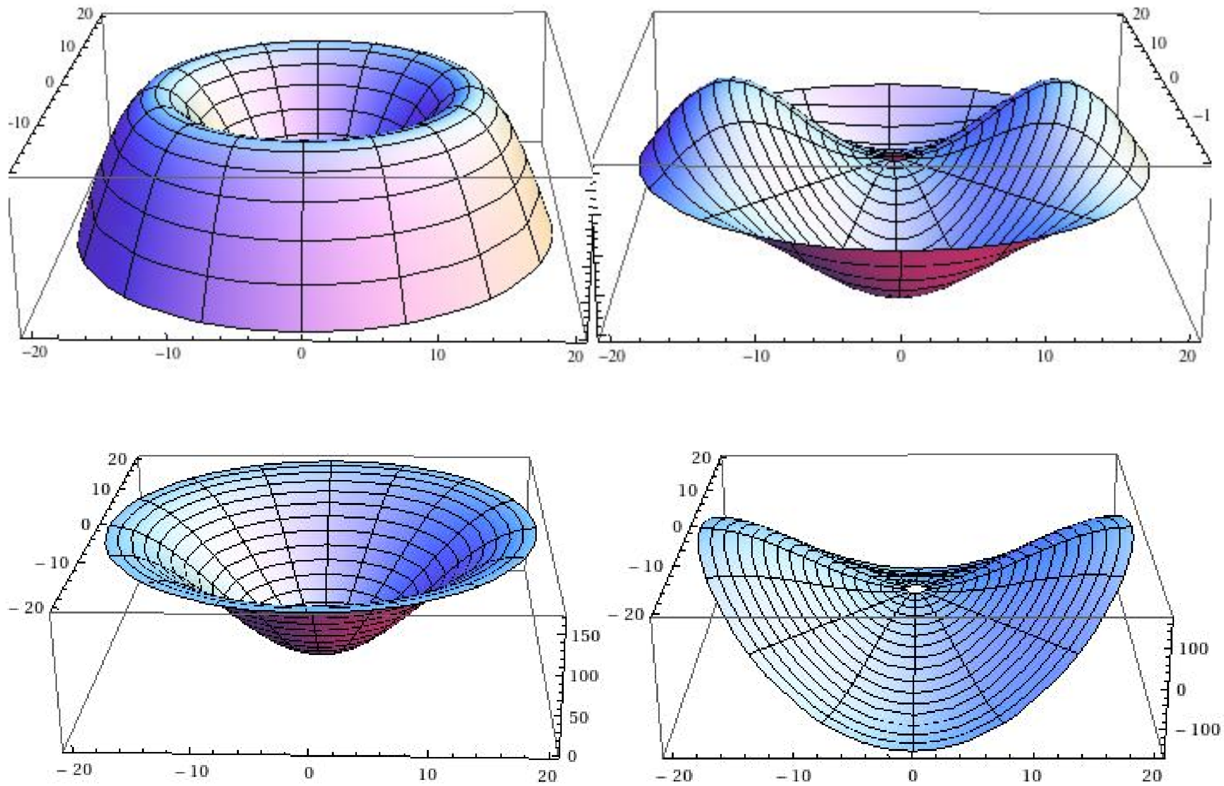

Figure 6.6: Spatial distribution of nodeless acoustic clouds with Dirichlet (top) and Neumann (bottom) boundary condition and $m = 2$, on the r, ϕ plane. On the left panel we present $|\Phi_m|$, while on the right panel we show the real part of Φ_m, for a fixed t. In all plots the outer edge is the cylindrical mirror and the inner boundary is the draining bathtub horizon. We have fixed $r_0/r_H = 20$ and the cloud supporting background has $B/r_H \simeq 0.13$, for the Dirichlet case, and $B/r_H \simeq 0.08$, for the Neumann case.

which there could be some extra simplification for the radial equation, as it happens for the clouds around extremal Kerr black holes [58].

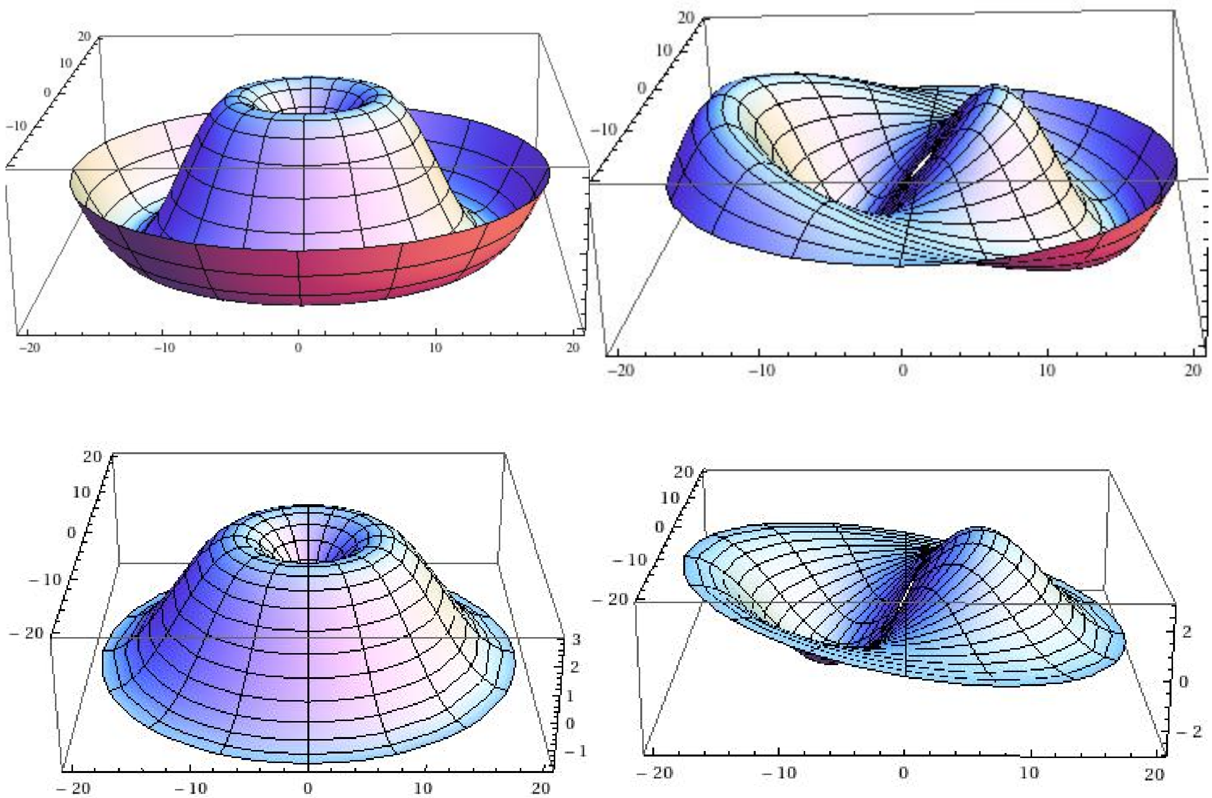

Figure 6.7: Same as in Fig. 6.5, but for nodeful acoustic clouds with $n = 1$ and $m = 1$, on the r, ϕ plane. Again, we have fixed $r_0/r_H = 20$ and the cloud supporting background has $B/r_H \simeq 0.35$, for the Dirichlet case, and $B/r_H \simeq 0.27$, for the Neumann case.

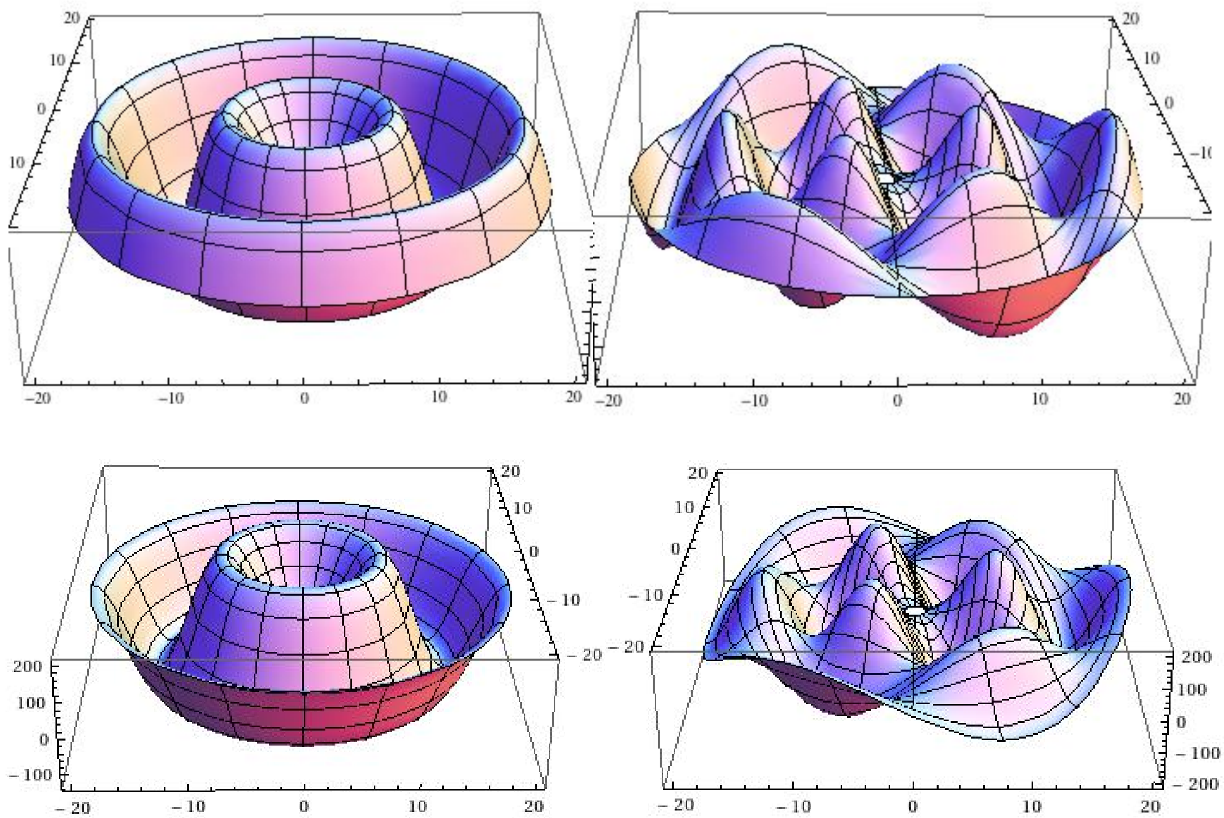

Figure 6.8: Same as in Fig. 6.5 but with $n = 2$ and $m = 3$. The position of the mirror is $r_0/r_H = 20$, and the circulation is $B/r_H = 0.22$, for the Dirichlet case, and $B/r_H = 0.19$, for the Neumann case.

Chapter 7

Stationary scalar clouds in a static fluid

Systems with superradiant instability present the possibility of finding bound states, i.e., clouds. In this chapter we investigate clouds in a system formed by a static fluid placed between two concentric cylinders, with the inner cylinder rotating with constant angular momentum. The resulting equations can be used to describe both sound and gravity waves.

7.1 Sound waves in a static profile

Assuming cylindrical symmetry, the Klein-Gordon equation can be reduced to an ordinary differential equation for the radial coordinate r. Indeed, with the *ansatz*

$$\psi(t, r, \vartheta, z) = \frac{\varphi(r)}{\sqrt{r}} e^{-i\omega t + im\theta}, \tag{7.1}$$

with $\varphi(r)$ obeying

$$\partial_r^2 \varphi + \left[\frac{\omega^2}{c_s^2} - \frac{1}{r^2}\left(m^2 - \frac{1}{4}\right)\right]\varphi = 0, \tag{7.2}$$

where $\omega > 0$ is the frequency of the wave and $m \in \mathbb{Z}$ is the azimuthal wave number. The most general solution of Eq. (7.2) is given in terms of Bessel functions, namely

$$\varphi(r) = D_1 \sqrt{r} J_m\left(\frac{\omega r}{c_s}\right) + D_2 \sqrt{r} Y_m\left(\frac{\omega r}{c_s}\right), \tag{7.3}$$

where D_1 and D_2 are constants. We note that the equations above, specially the wave equation, have analogous version which hold if surface (gravity) waves are considered instead of sound waves.

7.2 Boundary conditions

Typically, the presence of stationary scalar clouds is intimately linked to the phenomenon of superradiance, requiring rotational energy to occur. The simplest way to accomplish this is to consider the non-trivial metric produced by a rotating fluid. However, since our fluid is static, this requirement has to be fulfilled in some other way.

Here, we consider a rotating cylinder, of radius R_0, placed inside the fluid. A larger cylindrical surface, of radius R_1 and concentric with respect to the first cylinder, encloses the system. The inner cylinder rotates with a constant angular velocity Ω. This system was first considered in Ref. [112].

We assume further that the cylinders can exchange energy and momentum with incident waves. This interaction between the cylinder and the waves is characterized by a complex number, called the impedance Z_ω of the cylinder, that relates the pressure change to the radial velocity perturbation on the cylinder [113]. The real part of the impedance is called resistance and relates to the energy flow. We assume $\mathrm{Re}(Z_\omega) > 0$, corresponding to a surface which absorbs energy. The imaginary part, on the other hand, is called reactance and is related to the natural oscillation frequency of the surface.

In terms of the impedance, the boundary condition for both sound and surface waves in the rest frame of the inner cylinder is

$$\left.\left(\frac{\partial_r \psi}{\psi}\right)\right|_{r=R_0} = -\frac{i\rho_0\omega}{Z_\omega}. \tag{7.4}$$

When the cylinder rotates uniformly with angular velocity Ω, we may transform to a new angular coordinate $\widetilde{\phi} = \phi + \Omega t$, which effectively amounts to the replacement of ω with $\tilde{\omega} = \omega - m\Omega$ in (7.4). In terms of the radial field φ, we have

$$\left.\partial_r \varphi\right|_{r=R_0} = \left(\frac{1}{2R_0} - i\rho_0 \frac{\tilde{\omega}}{Z_{\tilde{\omega}}}\right) \left.\varphi\right|_{r=R_0}. \tag{7.5}$$

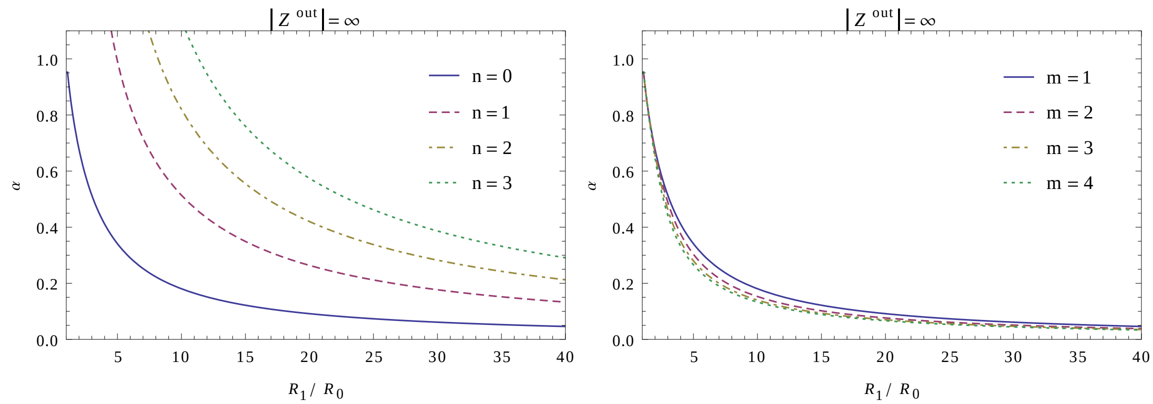

Figure 7.1: Existence lines for different values of n (left plot) and m (right plot). For both cases we consider $|Z^{out}| = \infty$.

For the external cylinder, the boundary condition is given by

$$\left(\frac{\partial_r \psi}{\psi}\right)\bigg|_{r=R_1} = +\frac{i\rho_0\omega}{Z_\omega^{out}}, \tag{7.6}$$

which can be written as

$$\partial_r \varphi|_{r=R_1} = \left(\frac{1}{2R_1} + i\rho_0 \frac{\omega}{Z_\omega^{out}}\right) \varphi|_{r=R_1}, \tag{7.7}$$

7.3 Stationary clouds

Combining Eq. (7.3) with the boundary equations, given by Eqs. (7.5) and (7.7), we find

$$\frac{i(\sigma-1)J_m + \sigma Z J_m'}{i(\sigma-1)Y_m + \sigma Z Y_m'} = \frac{i\hat{J}_m - Z^{out}\hat{J}_m'}{i\hat{Y}_m - Z^{out}\hat{Y}_m'}, \tag{7.8}$$

where $J_i = J_i(m\alpha\sigma)$, $Y_i = Y_i(m\alpha\sigma)$, $\hat{J}_i = J_i(m\alpha\sigma R_1/R_0)$, $\hat{Y}_i = Y_i(m\alpha\sigma R_1/R_0)$, $\sigma = \omega/m\Omega$, $\alpha = \Omega R_0/c_s$, $Z = Z_{\tilde{\omega}}/(\rho_0 c_s)$, $Z^{out} = Z_\omega^{out}/(\rho_0 c_s)$.

In order to find the clouds solutions we fix $\sigma = 1$, i.e. $\omega = \omega_c = m\Omega$, what gives us

$$\frac{J_m'}{Y_m'} = \frac{i\hat{J}_m - Z^{out}\hat{J}_m'}{i\hat{Y}_m - Z^{out}\hat{Y}_m'}. \tag{7.9}$$

We note that Eq. (7.9) does not depend on the impedance of the inner cylinder, such that we only have to choose Z^{out}. We solve Eq. (7.9) using a shooting method, choosing different values for Z^{out}.

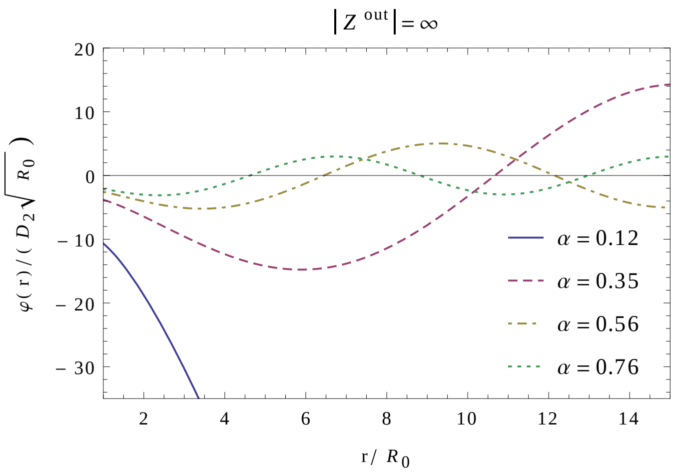

Figure 7.2: Radial solution for $R_1/R_0 = 15$ and $|Z^{out}| = \infty$. Each value of α corresponds to a different node number.

The first case we consider is the case for $|Z^{out}| = \infty$. In Fig. 7.1 we see that these clouds exist in a one dimensional line in the two dimensional phase space formed by α and R_1/R_0. As we increase the value of n, for a fixed α, the corresponding cloud occurs for a bigger value of R_1/R_0. This happens because as we increase n we go to more energetic solutions. On the other hand, as we increase m, for a fixed α, the corresponding cloud happens for a smaller value of R_1/R_0. This is due to an equilibrium between the angular momentum of the cloud and of the internal cylinder. We also observe that as $R_1/R_0 \to \infty$, $\alpha \to 0$. This happens because we do not have clouds when the internal cylinder is static, such that the existence lines do not cross the abscissa axis.

In Fig. 7.2 we exhibit the radial solutions given by Eq. (7.2), for $|Z^{out}| = \infty$, $m = 1$, $R_1/R_0 = 15$, and different values of α, what corresponds to various node numbers. Here we can see that choosing $|Z^{out}| = \infty$ is equivalent to setting a Neumann boundary condition.

Fig. 7.3 presents the existence lines for $Z^{out} = -0.01i$. For this case we obtain the same general behaviour as the one described for Fig. 7.1, with the difference that for the same R_1/R_0, clouds happen for bigger values of α.

In Fig. 7.4 we present the radial solution for different number of nodes with $Z^{out} = -0.01i$. For this case, we see that this choice of impedance is equivalent to setting a Dirichlet boundary condition.

For Fig. 7.5 we have fixed $Z^{out} = -i$. We have the same general behavior as the one

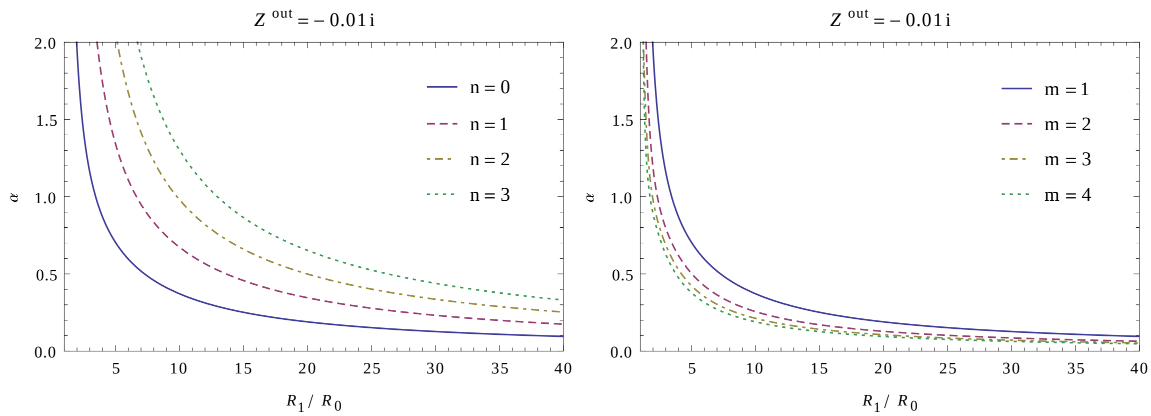

Figure 7.3: Existence lines for different values of n (left) and of m (right). For these cases we have chosen $Z^{out} = -0.01i$.

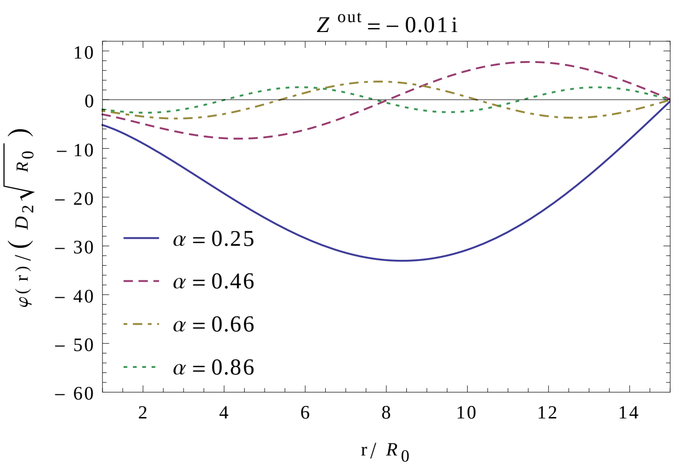

Figure 7.4: Radial solution with different number of nodes for $R_1/R_0 = 15$ and $Z^{out} = -0.01i$.

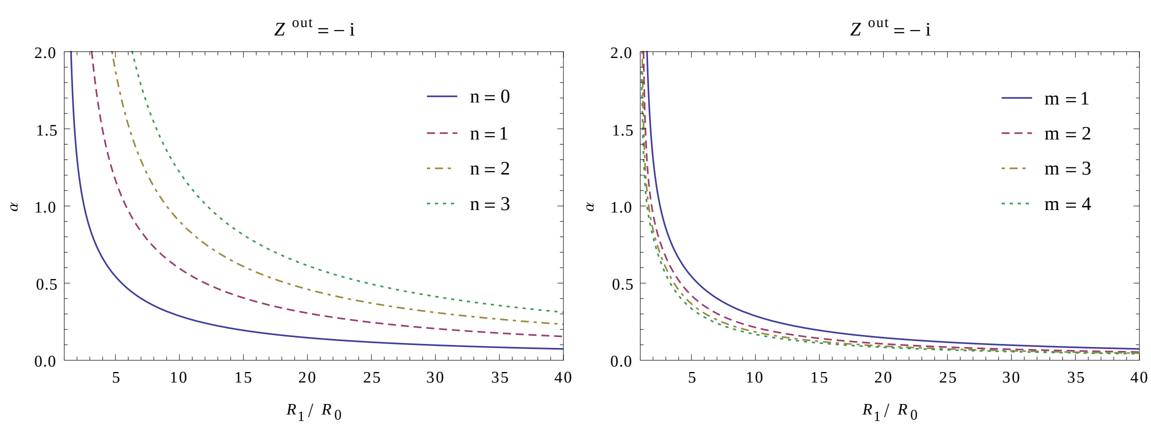

Figure 7.5: Existence lines for $Z^{out} = -i$ with different n (left) and m (right).

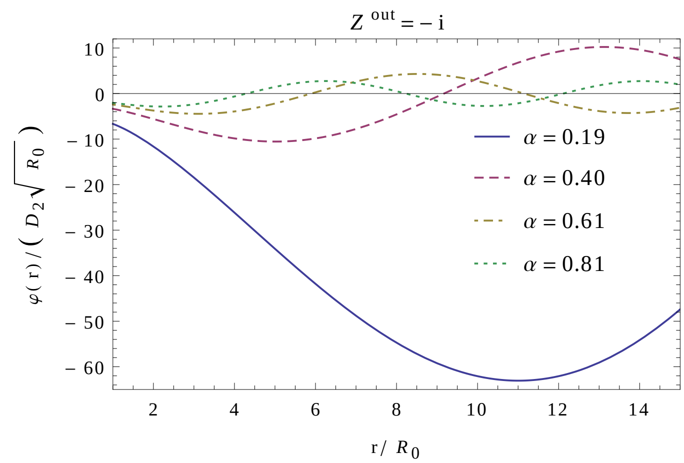

Figure 7.6: Radial solution with different number of nodes for $R_1/R_0 = 15$ and $Z^{out} = -i$.

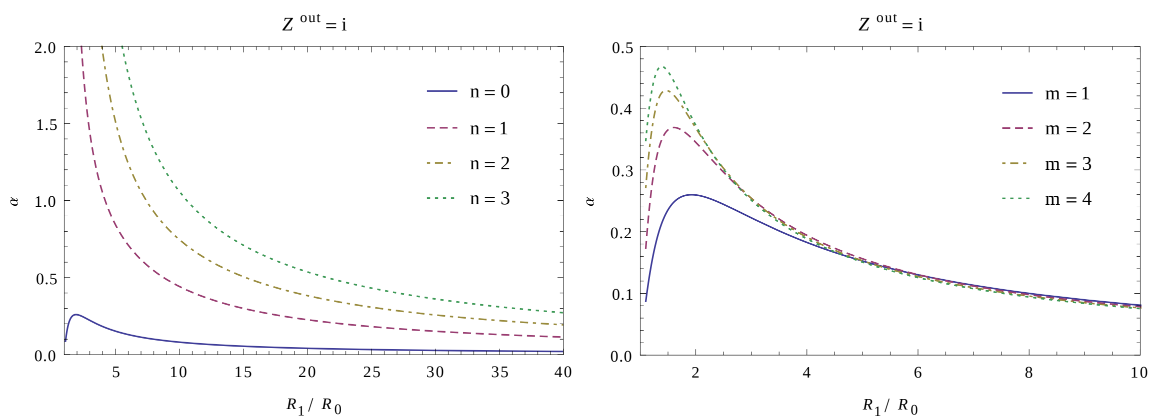

Figure 7.7: Existence lines for $Z^{out} = i$ with different n (left) and m (right).

present in Figs. 7.2 and 7.4, but now for a fixed R_1/R_0 the clouds happens for intermediate values of α. We can also observe this feature in Fig. 7.6, since we are choosing a boundary condition that is a combination of a Neumann and a Dirichlet boundary condition.

The last case we consider is for $Z^{out} = i$, as shown in Fig. 7.7. For this case, the existence line for $n = 0$ presents a maximum. We also note that, as we increase the value of m, the value of the maximum increases.

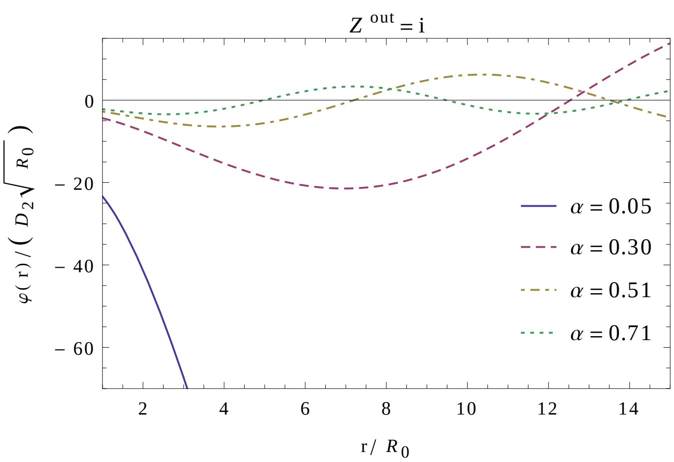

Figure 7.8: Radial solution with different number of nodes for $R_1/R_0 = 15$ and $Z^{out} = i$.

Conclusion

In this thesis we considered scalar fields around black holes and analogues, focusing on the absorption cross sections and bound states. We considered the propagation of scalar fields around black holes, computing the absorption cross section for the full range of frequencies. For the high-frequency limit we considered the eikonal approximation, using the equations of motion for particles to compute the absorption cross section in this limit.

We first considered a massive scalar field impinging upon a charged black hole, finding that, as we increase the black hole charge the absorption cross section decreases, what is compatible with the decrease of the black hole area and critical impact parameter. For the low-frequency regime we find two different limits for the absorption cross section, depending on the velocity of the field. We have shown that for ultralight particles both limits can be relevant.

Next, we considered a massive and charged scalar field around a charged black hole. We have seen that, as we increase qQ, the absorption cross section gets smaller. This happens because in this case we have an electromagnetic repulsion competing with the gravitational interaction. For this case we can have superradiance and both the partial and total absorption cross section can be negative, what means that planar waves can be superradiantly scattered.

We also considered the case of a massive scalar field around a charged rotating black hole, for various incidence angles. For on-axis incidence the absorption cross section presents a regular behaviour and decreases as we increase either the angular momentum or the charge of the black hole. For off-axis incidence the absorption cross section becomes less regular, such that is better to consider the corrotating and counterrotating modes separately. For this case we also have superradiance, although, due to the sum in m the total absorption cross section is always positive.

Concerning the bound state solutions, we found scalar clouds by solving the Klein-Gordon equation for a massive and charged scalar field in a Kerr-Newman background. We found that these clouds exist only for certain values of the parameters of the black hole and of the scalar field, what gives us existence lines in the parameter space. Each existence line is characterized by quantum numbers n, l and m, which are analogue to the quantum numbers of the Hydrogen atom.

We compared our numerical results for the existence lines with some analytic approximations found in the literature, which in principle are valid for either small or high rotation. Somewhat surprisingly, in the cases studied here, these approximations yield a fairly accurate estimate even far away from their *a priori* validity region.

Such clouds around black holes indicate that we can have hairy solutions for the corresponding geometries, if we consider higher order effects of the scalar field. However, this is not the only way to obtain hairy black holes. For instance, we can have the formation of hair due to nonlinear effects.

Clouds are possible at the threshold of superradiant instabilities, therefore we should be able to find these bound states for other unstable spacetimes. For instance, we can consider clouds in geometries which are not asymptotically flat, such as Kerr-de Sitter and Kerr-anti-de Sitter.

We also considered acoustic clouds for sound waves in a draining bathtub. In this case, the clouds are characterized by two quantum numbers: n and m. We also considered a massless scalar field in a Kerr background inside a cavity, in order to make comparisons with the acoustic analogue case.

Analogue models can make more clear the distinction between phenomena that are due to the kinematics or the dynamics of the system. We have seen that we can also find bound states for the draining bathtub, even though they have a completely different dynamics from black holes. But it is not clear what we would obtain by considering the backscattering of these clouds in the geometry.

The results obtained for the draining bathtub point to a new possibility of research for analogue models, namely the experimental investigation of acoustic clouds, even though analogue systems can be difficult to implement and control in the laboratory.

The last case we considered was composed of a static fluid placed between two concentric cylinders, where the inner cylinder is rotating with constant angular momentum. The angular momentum spreads in the fluid, but, provided that we consider a small enough time scale, we can regard the fluid as being static. This provides a very simple model were we can find superradiance, and thus, clouds. This model can be used for sound waves, as well as for surface waves.

We have found configurations very similar to the ones found in the draining bathtub, when we considered the imaginary part of the impedance of the external cylinder to be negative. But, when it is positive, we have found that the existence lines for $n = 0$ only occur for small enough values of the angular momentum of the inner cylinder.

Bibliography

[1] R. H. Fowler, “On dense matter,” *Mon. Not. Roy. Astron. Soc.*, vol. 87, pp. 114–122, 1926.

[2] S. Chandrasekhar, “The maximum mass of ideal white dwarfs,” *Astrophys. J.*, vol. 74, pp. 81–82, 1931.

[3] U. Das and B. Mukhopadhyay, “New mass limit for white dwarfs: super-Chandrasekhar type Ia supernova as a new standard candle,” *Phys. Rev. Lett.*, vol. 110, no. 7, p. 071102, 2013, 1301.5965.

[4] J. R. Oppenheimer and G. M. Volkoff, “On Massive neutron cores,” *Phys. Rev.*, vol. 55, pp. 374–381, 1939.

[5] C. E. Rhoades, Jr. and R. Ruffini, “Maximum mass of a neutron star,” *Phys. Rev. Lett.*, vol. 32, pp. 324–327, 1974.

[6] K. Schwarzschild, “Über das Gravitationsfeld eines Massenpunktes nach der Einsteinschen Theorie,” *Sitzungsber. Preuss. Akad. Wiss. Berlin (Math. Phys.)*, vol. 7, pp. 189–196, 1916, physics/9905030.

[7] H. Reissner, “Über die Eigengravitation des elektrischen Feldes nach der Einsteinschen Theorie,” *Ann. Phys.*, vol. 355, pp. 106–120, 1916.

[8] G. Nordstrom, “On the Energy of the Gravitational Field in Einstein’s Theory,” *Proc. Kon. Ned. Akad. Wet.*, vol. 20, p. 1238, 1918.

[9] R. P. Kerr, “Gravitational field of a spinning mass as an example of algebraically special metrics,” *Phys. Rev. Lett.*, vol. 11, pp. 237–238, 1963.

[10] E. T. Newman, R. Couch, K. Chinnapared, A. Exton, A. Prakash, and R. Torrence, "Metric of a Rotating, Charged Mass," *J. Math. Phys.*, vol. 6, pp. 918–919, 1965.

[11] G. W. Gibbons, "Vacuum Polarization and the Spontaneous Loss of Charge by Black Holes," *Commun. Math. Phys.*, vol. 44, pp. 245–264, 1975.

[12] S. Davidson, S. Hannestad, and G. Raffelt, "Updated bounds on millicharged particles," *JHEP*, vol. 05, p. 003, 2000, hep-ph/0001179.

[13] V. Cardoso, C. F. B. Macedo, P. Pani, and V. Ferrari, "Black holes and gravitational waves in models of minicharged dark matter," *JCAP*, vol. 1605, no. 05, p. 054, 2016, 1604.07845.

[14] H. Falcke, F. Melia, and E. Agol, "Viewing the shadow of the black hole at the galactic center," *Astrophys. J.*, vol. 528, p. L13, 2000, astro-ph/9912263.

[15] R.-S. Lu, A. E. Broderick, F. Baron, J. D. Monnier, V. L. Fish, S. S. Doeleman, and V. Pankratius, "Imaging the Supermassive Black Hole Shadow and Jet Base of M87 with the Event Horizon Telescope," *Astrophys. J.*, vol. 788, p. 120, 2014, 1404.7095.

[16] S. R. Dolan and T. Stratton, "Rainbow scattering in the gravitational field of a compact object," 2017, 1702.06127.

[17] R. A. Matzner, "Scattering of massless scalar waves by a schwarzschild 'singularity'," *Journal of Mathematical Physics*, vol. 9, no. 1, pp. 163–170, 1968.

[18] N. Sanchez, "Absorption and emission spectra of a Schwarzschild black hole," *Phys. Rev. D*, vol. 18, p. 1030, 1978.

[19] C. F. B. Macedo, L. C. S. Leite, and L. C. B. Crispino, "Absorption by dirty black holes: Null geodesics and scalar waves," *Phys. Rev. D*, vol. 93, p. 024027, 2016.

[20] E. Jung and D. Park, "Effect of scalar mass in the absorption and emission spectra of Schwarzschild black hole," *Class. Quantum Grav.*, vol. 21, pp. 3717–3732, 2004.

[21] W. Unruh, "Absorption Cross-Section of Small Black Holes," *Phys. Rev. D*, vol. 14, pp. 3251–3259, 1976.

[22] C. Doran, A. Lasenby, S. Dolan, and I. Hinder, "Fermion absorption cross section of a Schwarzschild black hole," *Phys. Rev. D*, vol. 71, p. 124020, 2005.

[23] S. Dolan, C. Doran, and A. Lasenby, "Fermion scattering by a Schwarzschild black hole," *Phys. Rev. D*, vol. 74, p. 064005, 2006.

[24] L. C. Crispino, S. R. Dolan, and E. S. Oliveira, "Electromagnetic wave scattering by Schwarzschild black holes," *Phys. Rev. Lett.*, vol. 102, p. 231103, 2009, 0905.3339.

[25] C. Vishveshwara, "Scattering of Gravitational Radiation by a Schwarzschild Black-hole," *Nature*, vol. 227, pp. 936–938, 1970.

[26] K. Glampedakis and N. Andersson, "Scattering of scalar waves by rotating black holes," *Class. Quantum Grav.*, vol. 18, pp. 1939–1966, 2001, gr-qc/0102100.

[27] C. F. B. Macedo, L. C. S. Leite, E. S. Oliveira, S. R. Dolan, and L. C. B. Crispino, "Absorption of planar massless scalar waves by Kerr black holes," *Phys. Rev. D*, vol. 88, p. 064033, 2013, 1308.0018.

[28] L. C. S. Leite, L. C. B. Crispino, E. S. De Oliveira, C. F. B. Macedo, and S. R. Dolan, "Absorption of massless scalar field by rotating black holes," *Int. J. Mod. Phys. D*, vol. 25, no. 09, p. 1641024, 2016.

[29] S. R. Dolan, "Scattering and Absorption of Gravitational Plane Waves by Rotating Black Holes," *Class. Quantum Grav.*, vol. 25, p. 235002, 2008, 0801.3805.

[30] T. Nakamura and H. Sato, "Absorption of Massive Scalar Field by a Charged Black Hole," *Phys. Lett. B*, vol. 61, pp. 371–374, 1976.

[31] L. C. Crispino, S. R. Dolan, and E. S. Oliveira, "Scattering of massless scalar waves by Reissner-Nordstrom black holes," *Phys. Rev. D*, vol. 79, p. 064022, 2009.

[32] L. C. Crispino and E. S. Oliveira, "Electromagnetic absorption cross section of Reissner-Nordström black holes," *Phys. Rev. D*, vol. 78, p. 024011, 2008.

[33] L. C. Crispino, A. Higuchi, and E. S. Oliveira, "Electromagnetic absorption cross section of Reissner-Nordstrom black holes revisited," *Phys. Rev. D*, vol. 80, p. 104026, 2009.

[34] L. C. B. Crispino, S. R. Dolan, A. Higuchi, and E. S. de Oliveira, "Inferring black hole charge from backscattered electromagnetic radiation," *Phys. Rev. D*, vol. 90, p. 064027, 2014.

[35] E. S. Oliveira, L. C. Crispino, and A. Higuchi, "Equality between gravitational and electromagnetic absorption cross sections of extreme Reissner-Nordstrom black holes," *Phys. Rev. D*, vol. 84, p. 084048, 2011.

[36] L. C. B. Crispino, S. R. Dolan, A. Higuchi, and E. S. de Oliveira, "Scattering from charged black holes and supergravity," *Phys. Rev. D*, vol. 92, no. 8, p. 084056, 2015, 1507.03993.

[37] E. Jung, S. Kim, and D. Park, "Proof of universality for the absorption of massive scalar by the higher-dimensional Reissner-Nordstrom black holes," *Phys. Lett. B*, vol. 602, pp. 105–111, 2004.

[38] E. Jung and D. Park, "Absorption and emission spectra of an higher-dimensional Reissner-Nordstrom black hole," *Nucl. Phys. B*, vol. 717, pp. 272–303, 2005, hep-th/0502002.

[39] L. C. B. Crispino, A. Higuchi, and G. E. A. Matsas, "Low-frequency absorption cross section of the electromagnetic waves for extreme Reissner-Nordström black holes in higher dimensions," *Phys. Rev. D*, vol. 82, p. 124038, 2010.

[40] R. Brito, V. Cardoso, and P. Pani, *Superradiance: Energy Extraction, Black-Hole Bombs and Implications for Astrophysics and Particle Physics*, vol. 906. Springer, 2015.

[41] R. H. Dicke, "Coherence in Spontaneous Radiation Processes," *Phys. Rev.*, vol. 93, pp. 99–110, 1954.

[42] Y. Zeldovich, "Generation of Waves by a Rotating Body," *Pisma Zh. Eksp. Teor. Fiz.*, vol. 14, p. 270, 1971.

[43] Y. Zeldovich, "Amplification of cylindrical electromagnetic waves reflected by a rotating body," *Zh. Eksp. Teor. Fiz.*, vol. 62, p. 2076, 1972.

[44] C. W. Misner, "Interpretation of gravitational-wave observations," *Phys. Rev. Lett.*, vol. 28, pp. 994–997, 1972.

[45] J. D. Bekenstein, "Extraction of energy and charge from a black hole," *Phys. Rev. D*, vol. 7, pp. 949–953, 1973.

[46] T. Torres, S. Patrick, A. Coutant, M. Richartz, E. W. Tedford, and S. Weinfurtner, "Rotational superradiant scattering in a vortex flow," *Nat. Phys.*, 2017, 1612.06180.

[47] W. H. Press and S. A. Teukolsky, "Floating Orbits, Superradiant Scattering and the Black-hole Bomb," *Nature*, vol. 238, pp. 211–212, 1972.

[48] W. Israel, "Event horizons in static vacuum space-times," *Phys. Rev.*, vol. 164, pp. 1776–1779, 1967.

[49] W. Israel, "Event horizons in static electrovac space-times," *Commun. Math. Phys.*, vol. 8, pp. 245–260, 1968.

[50] D. C. Robinson, "Uniqueness of the Kerr black hole," *Phys. Rev. Lett.*, vol. 34, pp. 905–906, 1975.

[51] R. Ruffini and J. A. Wheeler, "Introducing the black hole," *Phys. Today*, vol. 24, no. 1, p. 30, 1971.

[52] C. Teitelboim, "Nonmeasurability of the lepton number of a black hole," *Lett. Nuovo Cim.*, vol. 3S2, pp. 397–400, 1972.

[53] J. B. Hartle, "Long-range neutrino forces exerted by kerr black holes," *Phys. Rev. D*, vol. 3, pp. 2938–2940, 1971.

[54] J. D. Bekenstein, "Novel 'no scalar hair' theorem for black holes," *Phys. Rev. D*, vol. 51, pp. 6608–6611, 1995.

[55] A. E. Mayo and J. D. Bekenstein, "No hair for spherical black holes: Charged and nonminimally coupled scalar field with selfinteraction," *Phys. Rev. D*, vol. 54, pp. 5059–5069, 1996, gr-qc/9602057.

[56] J. D. Bekenstein, "Black hole hair: 25 - years after," 1996, gr-qc/9605059.

[57] J. D. Bekenstein, "Nonexistence of baryon number for static black holes," *Phys. Rev. D*, vol. 5, pp. 1239–1246, 1972.

[58] S. Hod, "Stationary Scalar Clouds Around Rotating Black Holes," *Phys. Rev. D*, vol. 86, p. 104026, 2012, 1211.3202.

[59] C. A. R. Herdeiro and E. Radu, "Kerr black holes with scalar hair," *Phys. Rev. Lett.*, 2014, 1403.2757.

[60] C. A. R. Herdeiro and E. Radu, "A new spin on black hole hair," *Int. J. Mod. Phys. D*, vol. 23, no. 12, p. 1442014, 2014, 1405.3696.

[61] W. Unruh, "Experimental black hole evaporation," *Phys. Rev. Lett.*, vol. 46, pp. 1351–1353, 1981.

[62] C. L. Benone, E. S. de Oliveira, S. R. Dolan, and L. C. B. Crispino, "Absorption of a massive scalar field by a charged black hole," *Phys. Rev. D*, vol. 89, p. 104053, 2014, 1404.0687.

[63] C. L. Benone, E. S. de Oliveira, S. R. Dolan, and L. C. B. Crispino, "Addendum to 'Absorption of a massive scalar field by a charged black hole'," *Phys. Rev. D*, vol. 95, no. 4, p. 044035, 2017, 1702.06591.

[64] C. L. Benone, E. S. de Oliveira, S. R. Dolan, and L. C. B. Crispino, "Absorption cross section of a massive scalar field by a Reissner-Nordström black hole," To be published.

[65] C. L. Benone and L. C. B. Crispino, "Superradiance in static black hole spacetimes," *Phys. Rev. D*, vol. 93, p. 024028, 2016.

[66] L. C. S. Leite, C. L. Benone, and L. C. B. Crispino, "Scalar absorption by charged rotating black holes," Manuscript submitted for publication.

[67] C. L. Benone, L. C. B. Crispino, C. Herdeiro, and E. Radu, "Kerr-Newman scalar clouds," *Phys. Rev. D*, vol. 90, no. 10, p. 104024, 2014, 1409.1593.

[68] C. L. Benone, "Stationary configurations around charged rotating black holes," *Int. J. Mod. Phys. D*, vol. 25, no. 09, p. 1641012, 2016.

[69] C. L. Benone, L. C. B. Crispino, C. Herdeiro, and E. Radu, "Acoustic clouds: standing sound waves around a black hole analogue," *Phys. Rev. D*, vol. 91, no. 10, p. 104038, 2015, 1412.7278.

[70] C. L. Benone, L. C. B. Crispino, C. A. R. Herdeiro, and E. Radu, "Stationary bound states of massless scalar fields around black holes and black hole analogues," *Int. J. Mod. Phys. D*, vol. 24, no. 09, p. 1542018, 2015.

[71] M. Richartz, C. Herdeiro, C. L. Benone, and L. C. B. Crispino, "Stationary scalar clouds in a static fluid," To be published.

[72] S. Chandrasekhar, *The Mathematical Theory of Black Holes.* New York: Oxford University Press, 1983.

[73] A. de Vries, "The apparent shape of a rotating charged black hole, closed photon orbits and the bifurcation set a 4," *Class. Quantum Grav.*, vol. 17, no. 1, p. 123, 2000.

[74] M. Visser, "Acoustic black holes: Horizons, ergospheres, and Hawking radiation," *Class. Quantum Grav.*, vol. 15, pp. 1767–1791, 1998, gr-qc/9712010.

[75] M. Richartz, A. Prain, S. Liberati, and S. Weinfurtner, "Rotating black holes in a draining bathtub: superradiant scattering of gravity waves," *Phys. Rev. D*, vol. 91, no. 12, p. 124018, 2015, 1411.1662.

[76] J. A. Futterman, F. A. Handler, and R. A. Matzner, *Scattering from black holes.* England: Cambridge University Press, 1988.

[77] Y. Décanini, G. Esposito-Farèse, and A. Folacci, "Universality of high-energy absorption cross sections for black holes," *Phys. Rev. D*, vol. 83, p. 044032, 2011.

[78] Y. Décanini, A. Folacci, and B. Raffaelli, "Fine structure of high-energy absorption cross sections for black holes," *Class. Quantum Grav.*, vol. 28, p. 175021, 2011, 1104.3285.

[79] Y. Décanini, A. Folacci, and B. Raffaelli, "Resonance and absorption spectra of the schwarzschild black hole for massive scalar perturbations: a complex angular momentum analysis," *Phys. Rev. D*, vol. 84, p. 084035, 2011.

[80] S. R. Dolan and A. C. Ottewill, "On an expansion method for black hole quasinormal modes and regge poles," *Class. Quantum Grav.*, vol. 26, p. 225003, 2009.

[81] G. B. Arfken and H. J. Weber, *Mathematical Method for Physicists.* New York: Elsevier Academic Press, 2005.

[82] M. Abramowitz and I. A. Stegun, *Handbook of Mathematical Functions with Formulas, Graphics and Mathematical Tables.* New York: Dover Publications, 9th ed., 1965.

[83] A. Higuchi, "Low frequency scalar absorption cross-sections for stationary black holes," *Class. Quantum Grav.*, vol. 18, p. L139, 2001, hep-th/0108144.

[84] A. Higuchi, "Addendum to 'low-frequency scalar absorption cross sections for stationary black holes'," *Class. Quantum Grav.*, vol. 19, no. 3, p. 599, 2002.

[85] L. Hui, J. P. Ostriker, S. Tremaine, and E. Witten, "Ultralight scalars as cosmological dark matter," *Phys. Rev. D*, vol. 95, no. 4, p. 043541, 2017, 1610.08297.

[86] R. Schoedel, D. Merritt, and A. Eckart, "The nuclear star cluster of the Milky Way: proper motions and mass," *Astron. Astrophys.*, vol. 502, p. 91, 2009, 0902.3892.

[87] R. Bender *et al.*, "Hst stis spectroscopy of the triple nucleus of m31: two nested disks in keplerian rotation around a supermassive black hole," *Astrophys. J.*, vol. 631, p. 280, 2005, astro-ph/0509839.

[88] E. S. Oliveira, S. R. Dolan, and L. C. B. Crispino, "Absorption of planar waves in a draining bathtub," *Phys. Rev. D*, vol. 81, p. 124013, 2010.

[89] N. G. Alexopoulos and N. K. Uzunoglu, "Electromagnetic scattering from active objects: invisible scatterers," *Appl. Opt.*, vol. 17, no. 2, pp. 235–239, 1978.

[90] M. Kerker, "Electromagnetic scattering from active objects," *Appl. Opt.*, vol. 17, no. 21, pp. 3337–3339, 1978.

[91] M. Kerker, "Resonances in electromagnetic scattering by objects with negative absorption," *Appl. Opt.*, vol. 18, no. 8, pp. 1180–1189, 1979.

[92] M. Abramowitz and I. A. Stegun, *Handbook of Mathematical Functions with Formulas, Graphs, and Mathematical Tables.* New York: Dover, 1964.

[93] D. Brill, P. Chrzanowski, C. Martin Pereira, E. Fackerell, and J. Ipser, "Solution of the scalar wave equation in a kerr background by separation of variables," *Phys. Rev. D*, vol. 5, pp. 1913–1915, 1972.

[94] S. Hod, "Stationary resonances of rapidly-rotating Kerr black holes," *Eur. Phys. J. C*, vol. 73, no. 4, p. 2378, 2013, 1311.5298.

[95] S. L. Detweiler, "Klein-Gordon equation and rotating black holes," *Phys. Rev. D*, vol. 22, pp. 2323–2326, 1980.

[96] J. C. Degollado and C. A. Herdeiro, "Stationary scalar configurations around extremal charged black holes," *Gen. Rel. Grav.*, vol. 45, pp. 2483–2492, 2013, 1303.2392.

[97] M. O. P. Sampaio, C. Herdeiro, and M. Wang, "Marginal scalar and Proca clouds around Reissner-Nordström black holes," *Phys. Rev. D*, vol. 90, no. 6, p. 064004, 2014, 1406.3536.

[98] H. Furuhashi and Y. Nambu, "Instability of massive scalar fields in Kerr-Newman space-time," *Prog. Theor. Phys.*, vol. 112, pp. 983–995, 2004, gr-qc/0402037.

[99] D. Nunez, H. Quevedo, and D. Sudarsky, "Black holes have no short hair," *Phys. Rev. Lett.*, vol. 76, pp. 571–574, 1996, gr-qc/9601020.

[100] J. M. Bardeen, W. H. Press, and S. A. Teukolsky, "Rotating black holes: Locally nonrotating frames, energy extraction, and scalar synchrotron radiation," *Astrophys. J.*, vol. 178, p. 347, 1972.

[101] S. Hod, "Rotating black holes can have short bristles," *Phys. Lett. B*, vol. 739, pp. 196–200, 2014, 1411.2609.

[102] S. Hod, "Hairy Black Holes and Null Circular Geodesics," *Phys. Rev. D*, vol. 84, p. 124030, 2011, 1112.3286.

[103] Y. Brihaye, C. Herdeiro, and E. Radu, "Myers-Perry black holes with scalar hair and a mass gap," *Phys. Lett. B*, vol. 739, pp. 1–7, 2014, 1408.5581.

[104] V. Cardoso and P. Pani, "Tidal acceleration of black holes and superradiance," *Class. Quantum Grav.*, vol. 30, p. 045011, 2013, 1205.3184.

[105] S. R. Coleman, "Q Balls," *Nucl. Phys. B*, vol. 262, p. 263, 1985.

[106] E. Radu and M. S. Volkov, "Existence of stationary, non-radiating ring solitons in field theory: knots and vortons," *Phys. Rept.*, vol. 468, pp. 101–151, 2008, 0804.1357.

[107] C. Herdeiro, E. Radu, and H. Runarsson, "Non-linear Q-clouds around Kerr black holes," *Phys. Lett. B*, vol. 739, pp. 302–307, 2014, 1409.2877.

[108] M. Lax and H. Feshbach, "Absorption and scattering for impedance boundary conditions on spheres and circluar cylinders," *J. Acoust. Soc. Am.*, vol. 20, p. 108, 1948.

[109] L. A. Oliveira, V. Cardoso, and L. C. B. Crispino, "Ergoregion instability: The hydrodynamic vortex," *Phys. Rev. D*, vol. 89, no. 12, p. 124008, 2014, 1405.4038.

[110] J. Barranco, A. Bernal, J. C. Degollado, A. Diez-Tejedor, M. Megevand, *et al.*, "Schwarzschild black holes can wear scalar wigs," *Phys. Rev. Lett.*, vol. 109, p. 081102, 2012, 1207.2153.

[111] H. S. Vieira and V. B. Bezerra, "Acoustic black holes: massless scalar field analytic solutions and analogue hawking radiation," *Gen. Rel. Grav.*, vol. 48, no. 7, p. 88, 2016.

[112] V. Cardoso, A. Coutant, M. Richartz, and S. Weinfurtner, "Detecting Rotational Superradiance in Fluid Laboratories," *Phys. Rev. Lett.*, vol. 117, no. 27, p. 271101, 2016, 1607.01378.

[113] S. W. Rienstra and A. Hirschberg, "An Introduction to Acoustics," 2015. `http://www.win.tue.nl/~sjoerdr/papers/boek.pdf`.